Thesis

Correlation induced topological states and magnetic/electron-nematic phase transitions

Kazuhiro Kimura

Department of Physics, Kyoto University

December, 2021

Abstract

The theoretical discovery of topological insulators in 2005 has reaffirmed the importance of band topology in condensed matter physics, which has been extended to superconductors, semimetals and developed into a major field. Furthermore, topological phases have been discovered in strongly correlated systems and have attracted much attention. For example, in the long-known heavy-fermion compounds SmB_6 and YbB_{12}, surface states have been observed, and they have been established as topological insulators in strongly correlated systems. In addition to the above topological Kondo insulators, various types of correlation induced topological states have been studied, such as topological Mott insulators, interaction-reduced classifications, topological spin liquids, and so on. Electron correlation effects on topological states are particularly interesting because they have the potential to induce nontrivial properties. Thus we can say that the interplay between electron correlation and topology is one of the central subjects in modern condensed matter physics. One of the next steps in theoretical research is to investigate a variety of correlation-induced topological phases. Based on the above background, in this thesis, we analyze the correlation-induced topological states and their various phase transitions by numerical calculation.

First, we explore topological states with magnetically ordered phases by taking account of crystalline symmetry, i.e. a mirror symmetry. In particular, we focus on heavy-fermion systems, which have a nontrivial band topology due to the spin-orbit coupling and the strong Coulomb interaction. The emergence of topological properties in the magnetic phases has already been studied. Although in the absence of spatial symmetry, there is no topological phase in the two-dimensional (2D) antiferromagnetic phases at half filling, we demonstrate that a topological phase emerges in the presence of mirror symmetry. This is explicitly shown for a 2D periodic Anderson model. Furthermore, around quarter filling, our analysis shows that a half-metallic state emerges in the ferromagnetic phase, where a spin-selective gap opens, resulting in nontrivial properties characterized by a Chern number. In contrast to the previously proposed models which can apply for spin-conserving system, our scenario can even apply for a wider class of spin-nonconserving systems in the presence of spin-orbit coupling.

Second, we explore the correlation-induced non-Hermitian topological semimetals. In particular, we focus on the non-Hermitian band topology coming from the lifetime effects on quasi-particles in an equilibrium system. The emergence of the non-Hermitian topological semimetals in strongly correlated system has already been studied. Despite intensive studies, it remains unclear what physical properties are affected by the non-Hermitian band structure. In particular, there are few studies elucidating the effects of the non-Hermitian band structure on magnetic/electric responses. Based on the above background, we analyze a diamond-lattice Hubbard model with the spatially modulated Hubbard interaction. Our dynamical mean-field analysis with special emphasis on non-Hermitian properties elucidates that the gapless nodal line changes into a symmetry-protected ex-

ceptional torus (SPET) at the Fermi level enclosing the three-dimensional open Fermi surface, which is unique to non-Hermitian physics with chiral symmetry. Furthermore, we also elucidate the effects of the SPETs on the magnetic response; our results based on the random-phase approximation combined with the dynamical mean-field theory show that SPETs enhance the magnetic susceptibility at the weakly correlated sites, exemplifying effects of non-Hermitian degeneracies on responses to external fields.

Finally, we focus on the electron-nematic phase transition, such as magic-angle twisted bilayer graphene(MA-TBG) and doped-Bi_2Se_3, which are candidate materials of nematic superconductors. The relationship between electron-nematic order and unconventional superconductivity is a pressing question in present condensed matter physics. Motivated by recent studies of three-state Potts nematic states in magic-angle twisted bilayer graphene and doped-Bi_2Se_3, we analyze the impact of critical nematic fluctuations on the low energy properties of phonons. In this study, we propose how to identify the three-state Potts nematic fluctuations by ultrasound attenuation. The Gaussian fluctuation analysis shows that the Landau damping term becomes isotropic due to fluctuations of the C_3-breaking bond-order, and the nemato-elastic coupling is also shown to be isotropic. These two features lead to an isotropic divergence of the transverse sound attenuation coefficient and an isotropic lattice softening, in contrast to the case of the C_4-breaking bond-order which shows the strong anisotropy. Moreover, we use a mean-field approximation and discuss the impurity effects. The transition temperature takes its maximum near the filling of the van-Hove singularity, and the large density of states favors the nematic phase transition. It turns out that the phase transition is of weak first-order in the wide range of filling and, with increasing the impurity scattering, the first order transition line at low temperatures gradually shifts towards the second-order line, rendering the transition a weak first-order in a wider range of parameters. Furthermore, it is confirmed that the enhancement of the ultrasound attenuation coefficient will be clearly observed in experiments in the case of a weak first-order phase transition.

Contents

List of publications

Papers related to the thesis

1. Kazuhiro Kimura, Tsuneya Yoshida and Norio Kawakami
   Topological Properties of Magnetically Ordered Heavy-Fermion Systems in the Presence of Mirror Symmetry
   Journal of the Physical Society of Japan **87**, 084705 (2018).
   ©2018 The Physical Society of Japan

2. Kazuhiro Kimura, Tsuneya Yoshida and Norio Kawakami
   Chiral-symmetry protected exceptional torus in correlated nodal-line semimetals
   Physical Review B **100**, 115124 (2019).
   ©2019 The American Physical Society

3. Kazuhiro Kimura, Manfred Sigrist and Norio Kawakami
   Probing three-state Potts nematic fluctuations by ultrasound attenuation
   Physical Review B **105**, 035130 (2022).
   ©2022 The American Physical Society

Published papers not included in the thesis

1. Kazuhiro Kimura, Tsuneya Yoshida and Norio Kawakami
   Reflection-Symmetry Protected Antiferromagnetic Topological Insulator in Three-Dimensional Heavy-Fermion Systems
   JPS Conf. Proc. **30**, 011012 (2020).
   ©2020 The Physical Society of Japan

2. Robert Peters, Kazuhiro Kimura, Yoshihiro Michishita, Tsuneya Yoshida and Norio Kawakami
   Surface exceptional points in a topological Kondo insulator
   Physical Review B **104**, 235153 (2021).
   ©2021 The American Physical Society

Chapter 1

Introduction to topological materials in strongly correlated electron systems

Since the theoretical discovery of Z_2 topological insulators (TIs)[1–4], topological materials have been the subject of intense theoretical and experimental investigation. Furthermore, the notion of band topology has been extended to strongly correlated systems, where an interplay[5] between topology and Coulomb interaction hosts some exotic phenomena, e.g. topological Kondo insulators[6–8], topological Mott insulators[9–13], and the change of topological classification[14–31], etc. Electron correlation effects on topological states are particularly interesting because they have the potential to drastically change the ground state properties. The interplay between Coulomb interaction and topology is one of the central subjects in condensed matter physics and these two features are important notions for understanding a variety of materials.

In recent years, their interplay has been studied from new perspectives. One direction of researches has focused on material sciences, such as the development of functional materials and the search for new physical properties. Experimentally, in magnetic-impurity doped topological insulators, e.g. (Cr, V)-doped $(Bi,Sb)_2Te_3$,[32, 33] have been found to show the quantum anomalous Hall effect without external magnetic fields, e.g., Chern insulators. Chiral edge modes carry a non-dissipative current, which can be applied to spintronics devices. Furthermore, this observation provides a concrete platform for the exploration of exotic quantum effects such as the topological magnetoelectric effect and the formation of axion insulators. However, several problems remain, e.g., the anomalous quantum Hall effects realized by doping are still limited to the low temperature region of 2K. One way to solve this problem is to search topological materials that have a magnetic order in bulk, rather than a magnetic order formation by doping.

In addition to magnetic topological insulators, with the improvement of experimental techniques for the van der Waals layered materials, experiments with the twisted bilayer graphene have attracted much attention for the so-called first magic angle. Various exotic phases emerge, including the appearance of Mott insulators and unconventional superconducting states, which are a reminiscent feature of cuprate superconductors, quantum Hall ferromagnetic phases, and electron-nematic phases. Conventional graphene-based materials are dominated by p-electrons of carbon atoms, and therefore the Coulomb interaction is not very important. However, in the case of twisted bilayer graphene, the formation of the long-period moiré structure drastically changes the band structure to a quasi-flat band, thus the effect of Coulomb interaction becomes relatively large. In addition, one of the key advantages of this system is the electrical tunability of the charge carrier density in a flat band. This tunability enables us to study the phase diagrams of

unconventional superconductivity and correlated topological states. More experimental and theoretical studies are needed to clarify the origin of intertwined orders.

Another direction in recent researches has focused on new theoretical interests, such as the non-Hermitian topology inspired by the study of open or/and nonequilibrum systems, where the interaction with environments cannot be neglected. A non-Hermitian Hamiltonian gives an effective description in various contexts such as open quantum systems, photonic system[34–36]. Furthermore, as proposed by Kozii and Fu, even in equilibrium systems, such non-Hermitian topological properties [37] can appear due to the lifetime effects originating from a single-particle self-energy [38–42]. Such a new way to describe the quantum many-body systems is expected to provide a key to solve unsolved problems in condensed matter physics, such as the origins for quantum oscillations in topological Kondo insulators SmB_6 and YbB_{12}.

Inspired by the above experimental and theoretical progress, we investigate the physical properties of the correlation-induced topological states and these magnetic or electron-nematic phase transitions in this thesis. We aim to find new topological phenomena, clarify correlation effects, and discuss the stability of these phases in terms of numerical calculations and symmetry. To begin with, we give a brief review of theoretical and experimental backgrounds related to this thesis in the following. In Sec. 1.1, we give an overview of introduction to the interacting topological phases and show a general interest of research. In Sec. 1.2, we show several topological materials. In Sec. 1.3, we give another theoretical perspective of interacting topological phases, referred to as the lifetime induced non-Hermitian topological semimetals. Finally, we mention the organization of this thesis, in Sec. 1.4.

1.1 Introduction to interacting topological phases

Originally, topological materials[3, 4] such as insulators and superconductors are characterized by their metallic surface (edge) states which are protected by local symmetries of the systems. These results are summarized into a topological periodic table, so-called Altrand-Zirnbauer classification table [43–45]. A significant number of TIs have been found so far this decade, including an extension from local symmetry to crystalline symmetry, such as topological crystalline insulators [1, 2, 46–49]. Furthermore, the notion of topology has been generalized to gapless phases [50–56] such as Weyl semimetals, nodal-line semimetals, Weyl superconductor, and so on, where the relation between gapless points/lines and band topology is well understood from the view point of underlying symmetry. These topological phases, whose characteristics are determined by the topological nature of the bulk wave function, are new phases of matter that are different from the ordered phases characterized by symmetry breaking based on Landau theory. One of the essential differences is that the topological properties do not change continuously with external field, and disorder, etc, which is different from the symmetry-broken ordered phase where the order parameter changes continuously. In material science, an important feature of such topological phases is the existence of edge/surface states that is robust against impurities, thus the resulting nondissipative electric/spin current can be applied to the development of new functional materials, such as spintronics. In addition, the emergence of gapless Majorana fermions [57–62] and their non-Abelian statistics in topological superconductors is expected to have applications in topological quantum computation. Therefore, expanding a platform of designing such materials will be a very important issue in condensed matter physics.

The notion of topology has been extended to strongly correlated systems, where an interplay between topology and Coulomb interaction hosts some exotic phenomena. The study of strong Coulomb interaction has a long history since the discovery of high-T_c cuprate superconductors. The difficulty of these many-body problems, such as Mott insulator[63] that becomes insulating due to electron correlation and magnetic fluctuations that become a driving force for unconventional superconductor[64], cannot be resolved by the band theory alone. The electron correlation is one of the most important topics for understanding a variety of materials. With a long history of research, many theoretical concepts and treatments have been established, and interesting phenomena such as heavy-fermion, Kondo effect, Mott transition, and quantum critical phenomena have been studied. In such strongly correlated electron systems, many theoretical and experimental researches have also been carried out from the viewpoint of topology.

To clarify the purpose of studying the topological phases in strongly correlated electron systems, we explain what are of importance and interest. They are summarized in three points below.

- *To elucidate unique topological phases in interacting systems:* The effect of the interaction may cause a drastic change of electronic states, and exotic states with no counterparts in weakly correlated systems may be realized. An old example is the fractional quantum Hall state, which is one of the topological ordered phases, known as a system with long-range quantum entanglement. On the other hand, a topological Mott insulating state has been proposed for symmetry protected topological phase without long-range entanglement. The latter one can be understood by studying the impact of electron correlation on topological insulators.
- *To analyze the stability against strong electron interaction:* In contrast to the above, it is necessary to understand to what extent topological properties can be guaranteed, and from where topological properties are broken, beyond the single particle picture. This understanding will help to create physical platforms of topological phases that have been difficult to realize with weakly correlated systems. For example, in magnetic-impurity doped topological insulators have been found to show the quantum anomalous Hall effect without external magnetic fields.
- *To unravel the mysteries of quantum states of matter:* In strongly correlated electron systems, the introduction of the concept of topology leads to the solution of a long-standing mystery. To understand the origin of a variety of materials, the notion of topology is also important. For example, in heavy-fermion compounds SmB_6 and YbB_{12}, the topologically protected surface states have been pointed out as the origin of a long-known mystery of a low-temperature saturation of resistivity.

To begin with, we introduce theoretical progress in electron correlation effects on topological insulators for the last decade. In a band insulating system, the strong spin-orbit coupling allows a non-trivial topology of the electron bands. In parallel, in Mott insulating system, the strong spin-orbit coupling has attracted interest in the context of many frustrated magnets[65, 66]. Motivated by the question “How these two classes of phenomena are connected from weak to strong electron correlation with keeping on

the strong spin-orbit coupling ?", the interaction induced topological Mott insulator was firstly proposed by D. Pesin and L. Balents in 2010[9]. It may be regarded as a quantum spin-liquid state, where the topological Mott insulating phase is gapped in the bulk, while gapless spinons appear on the surface. Inspired by these theoretical studies, attention to interacting topological phases has increased. A number of numerical calculations were performed to investigate the interplay between strong spin-orbit coupling and electron-electron interactions and how the interaction affects the topological insulating phase[67–73]. In addition, an important result is the formulation of the topological number of interacting systems by V. Gurarie in 2011[74]. It was pointed out that topological properties of a bulk wave-function adiabatically connect[74–78] to a non-interacting system, even if the interactions are somewhat strong, as long as there is no Mott transition or symmetry breaking.

For a better understanding, we will now introduce a concrete example of a topological number in an interacting system with a many-body chiral symmetry discussed by V. Gurarie[74, 79]. For interacting systems, the symmetry defined for the Bloch Hamiltonian must be extended to a many-body Hamiltonian including the electron-electron interaction term. A convenient way to introduce a many-body chiral symmetry is to use the electron Green's function, which is given by $\Gamma^{\dagger}G(k,\omega)\Gamma = -G(k,\omega)$ with a wave number k, a frequency ω, and a many-body chiral operator Γ, $\Gamma^2 = 1$. For example one-dimensional system, the winding number in terms of Green's function can be defined as follows.

$$N = \mathrm{tr}\int_{-\pi}^{\pi}\frac{dk}{4\pi i}\Sigma\mathcal{G}^{-1}(k)\frac{\partial}{\partial k}\mathcal{G}(k), \tag{1.1}$$

where $\mathcal{G}(k)$ is defined as $\mathcal{G}(k) = G(k,\omega)|_{\omega=0}$ and a chiral matrix Σ for a Bloch Hamiltonian. If we set $\mathcal{G}^{-1}(k) = H_k$ with a Bloch Hamiltonian H_k here, we have a well-known formula of the winding number. We note that the Green's function formula is given for other topological numbers in similar manners[74–78]. The most important thing to understand here is how the topological phase transition occurs. From the above equation, we can see that there are two ways to change the winding number N. One is the case where $\mathcal{G}(k)$ has poles, i.e., $\mathcal{G}^{-1}(k) = 0$, corresponding to the gap closing of a single-particle excitation, which appears in an ordinary non-interacting system. The other is the case where $\mathcal{G}(k)$ has zeros, i.e., $\mathcal{G}(k) = 0$, caused by the divergence of the self-energy at $\omega = 0$ and corresponding to the Mott transition, where the single-particle excitation gap is closed by interactions.

The latter supports the possibility of a topological phase unique to Mott insulators, as pointed out by D. Pesin and L. Balents[9]. But, since they used a rather special method, a more generic treatment has been needed. Based on the understanding of topological band theory in terms of Green's function, the notion of topological Mott insulator has been established by density matrix renormalization group analysis in one dimensional systems by T. Yoshida, et. al., in 2014[10, 79]. Where the Mott transition of the topological edge state has been pointed out. The edge Mott states arising here can be understood in terms of the single-site Hubbard model $H_U = Un_{\uparrow}n_{\downarrow}$, with number operators $n_{\uparrow,\downarrow}$ for each spins. In the noninteracting case, the edge states are four-fold degenerate in Fig. 1.1(a), which means that the single-particle excitations are gapless, namely both charge excitation and spin excitation are gapless. On the other hand, in the interacting case, the four-fold degeneracy of the ground state is lifted and reduced to two-fold degeneracy in Fig. 1.1(b). This means the gap opening in the charge excitation, i.e., a Mott insulator, while spin excitations remain gapless, which corresponds to the edge Mott state. In the example of the single-site Hubbard model, a finite interaction results in a Mott insulator,

but this does not necessarily mean that a finite interaction results in an edge/surface Mott transition[10–13] in a general topological insulator. It is also an open problem whether or not the surface Mott states appear in higher dimensions, as originally proposed in frustrated magnets[9].

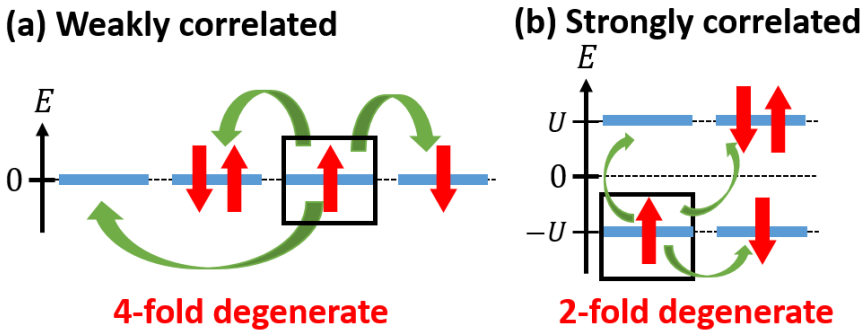

Fig. 1.1: Interaction effects on a topological edge state in a one dimensional system. (a) Gapless single particle excitation in noninteracting or weakly correlated topological edge state. (b) Charge gapped and spin gapless excitations in edge Mott state.

In this section, we have described how topological properties are changed by interactions. As we have shown above, electron correlation effects on the topological band structure are now well understood. While it is important that the interaction leads to the appearance of properties that are not present in weakly correlated systems, it is also important that the stability against the interaction is guaranteed. The latter one is also important for the study of topological Kondo insulators[7, 8] in heavy fermion systems and topological insulators coexisting or competing with long-range ordered phases[68, 69, 72, 73, 80, 81, 81, 82, 82–90]. In addition, what we have discussed here will be the basics for the following chapters. In the next section, we show the topological phases in strongly correlated electron systems from a materials science point of view.

1.2 Topological materials with strong electron correlation

In this section, we exemplify some topological materials in strongly correlated systems.

1.2.1 Heavy-fermion topological systems

Heavy-fermion materials[91–94] are a class of strongly correlated electron systems containing localized f-electrons which are surrounded by conducting d-electrons. In heavy-fermion metals, the effective electron mass is about 1000 times larger than the original one, resulting in magnetism, superconductivity, non-Fermi liquid, and quantum critical phenomena. This variety is understood by the competitive phenomena between the Kondo effect, where the conduction electrons screen the localized magnetic moment, and the RKKY (Rudermann Kittel Kasuya Yoshida) interaction, where the interaction between localized moments mediated by conduction electrons gives rise to magnetic phase transitions. A characteristic feature of heavy-fermion systems is that the energy scale changes to a small Kondo temperature $T_K \sim 10$ K instead of the Fermi temperature $T \sim 10^4$ K

of ordinary metals. This leads to dramatic changes in physical properties depending on pressure and magnetic field at low temperature regions.

As mentioned in the previous section, nontrivial topology enriches quantum states of matter to go beyond the classification into metals and insulators in terms of conventional band theory. In many cases, to realize such a topological phase, strong spin-orbit coupling is required. Heavier elements are preferred over lighter elements such as graphene which was originally proposed as a quantum spin Hall insulator[1, 2]. Heavy-fermion systems are also ideal platforms of exploring the non-trivial topological properties due to the strong spin-orbit coupling. We now give typical examples for the interplay of heavy-fermion and topology.

The topological Kondo insulator is a particularly simple type of topological materials in heavy-fermion systems[6–8]. Originally, the Kondo insulators, first discovered 40 years ago[95], have been known as a narrow gap semiconductor. While these materials have the strong electron-correlation, their low-energy properties can be regarded as adiabatically connected to non-interacting band insulators, where the hybridization between highly renormalized f-electrons and conducting d-electrons forms the excitation gaps of quasi-particles. It has been pointed out that the typical Kondo insulators can also be topologically classified[6]. In particular, SmB_6[96, 97] and YbB_{12}[98] have attracted much attention as a promising candidate for the topological Kondo insulator. The topologically protected surface states have been pointed out as the origin of a long-known mystery of a low-temperature saturation[99] of the electrical resistivity.

While the origin of the saturation has been revealed to be topologically protected surface states, quantum oscillation in the bulk has been reported in many experiments[100–104]. Namely, this means that electrically, it is a highly resistive insulator, but magnetically, it behaves like a metal, making its origin a great mystery. Moreover, the specific heat and thermal conductivity measurements[105, 106] suggest the existence of a charge neutral fermion[106] in the bulk YbB_{12}. Although many interesting theories have been proposed, motivated by these interesting experiments, the origin of the metallic behavior has not yet been understood.

In order to solve such difficult problems, a deeper understanding of the interplay between the electron correlation and topology is needed. For example, theory of lifetime-induced non-Hermitian topological semimetalls may explain such in-gap state. About this theory, we give more details later in Sec. 1.3. In addition to the topological Kondo insulator, recent studies have revealed another kind of topological state called Weyl-Kondo semimetals such as the noncentrosymmetric material $Ce_3Bi_4Pd_3$[107, 108], and the centrosymmetric material YbPtBi[109] under the magnetic field. Some of more interesting points are the study of electron correlation on topological transport properties[110, 111] and the study of Weyl semimetals near the magnetic field-induced quantum critical point[112]. The strong electron-correlation enriches topological states of matter and causes exotic phases with no counterpart of weakly correlated system.

1.2.2 Magnetic topological insulators

We have introduced correlation-induced topological states in the absence of long-range ordered phase. On the other hand, the interplay of magnetism and topology is also an important topic[68, 69, 72, 73, 80–90] from the perspective of materials science, such as the development of functional materials and the search for new physical properties. The magnetic topological insulators[32, 33] have attracted much attention to show the quantum anomalous Hall effect, where a non-dissipative topological current can be applied

to spintronics devices. Moreover, this observation provides a concrete platform for the exploration of exotic quantum effects such as the topological magnetoelectric effect and the formation of axion insulators. Experimentally, it has been realized as a ferromagnetic (FM) topological insulator made by doping magnetic impurities into the topological insulator, such as (Cr, V)-doped $(Bi,Sb)_2Te_3$ and Mn-doped Bi_2Te_3[32, 33]. The important point is to open an exchange gap in the surface state by breaking the time-reversal symmetry, namely realizing a quantum anomalous Hall insulator. Two mechanisms have been considered as a possible origin for ferromagnetism: the carrier-mediated RKKY mechanism and the local valence-electron-mediated Bloembergen-Rowland mechanism[33]. However, several problems remain, e.g., the anomalous quantum Hall effects realized by doping are still limited to the low temperature region of 2K and the inhomogeneity of the magnetism reduces the efficiency of realization and application. One way to solve this problem is to search topological materials that have a magnetic order in bulk, rather than a magnetic order formation by doping. How to design such an intrinsic magnetic topological insulator is a very important issue in topological material science.

Concerning nontrivial properties in bulk FM phases, a spin-selective topological insulator was proposed for heavy-fermion systems[88]. This is a half-metallic FM phase [113–117] around quarter filling, where the minority spin sector acquires a gap while the majority band remains gapless, which is called a spin-selective gap. If the insulating sector has a nontrivial topological number, we have an spin-selective topological insulator, which is a unique topological insulator embedded in a metallic phase. Unfortunately, however, it has been shown that this phase emerges only in spin-conserving systems and is not generally compatible with the presence of spin-orbit coupling, which is necessary for topological properties.

In the ferromagnetic phase, the problem has been how to realize a class A, namely Chern insulator without time-reversal symmetry. On the other hand, magnetic topological insulators based on magnetic symmetry have been proposed, and antiferromagnetic (AF) topological insulators[80] are a typical example. In such AF topological insulators, the primitive-lattice translation symmetry is broken by the collinear antiferromagnetic order, where the unit cell is doubled. The AF order breaks time-reversal (Θ) and primitive-lattice translational ($T_{1/2}$) symmetries but preserves their combined symmetry $S_{\boldsymbol{k}} = \Theta T_{1/2}(\boldsymbol{k})$. Under this symmetry, we can define a Z_2 topological number[118], which is related to the strong index of three-dimensional topological insulators[43–45]. Recently it is found that the van der Waals layered compound $MnBi_2Te_4$[119] could be a possible candidate for AF topological insulators. Note, however, that this Z_2 number is allowed only for three-dimensional systems, as confirmed by the periodic table[43–45, 118, 120, 121].

1.2.3 Electron-nematic phases

In this subsection, we show the electron-nematic phases in twisted bilayer graphene and doped-Bi_2Se_3, which are also topological materials in strongly correlated systems. After we first give an introduction about interests of electron-nematic states, we show these materials.

The stability of Fermi surface to interactions is an important notion[122] to understand the origin of a variety of quantum states of matter in strongly correlated systems. In 1958, based on Landau Fermi liquids theory, I. Pomeranchuk has firstly discussed the stability condition of the isotropic Fermi surface against interactions and the possibility of the spontaneous deformation of the Fermi surface, namely Pomeranchuk instability[123]. The electron-nematic states, specifically referred to as d-wave Pomeranchuk instability

in the case of an isotropic Fermi surface, are a translationally invariant metallic state with a spontaneously generated spatial anisotropy. Originally, the notion of the nematic electron liquid [124] was proposed as a quantum counterpart of classical nematic liquid crystals in a stripe charge ordered state in cuprate with the spontaneous C_4 breaking of the Fermi surface. This is a kind of charge order, and in terms of multipole, it belongs to a class called electric quadrupoles. Generally, electron-nematic states are the state which spontaneously breaks a certain point group symmetry, e.g., C_4- or C_3-rotational symmetry.

One of the most interesting feature of electron-nematic states is that it is intertwined with other ordered phases, including magnetic and superconducting ordered states. Recent discoveries of electron-nematic phases have suggested that the superconducting pairing mechanism may be closely related to nematicity in some correlated electron systems, such as cuprates, iron-based compounds, heavy-fermions, doped-Bi_2Se_3, magic-angle twisted-bilayer graphene (MA-TBG), and so on. Obviously, the relation between electron-nematic order and unconventional superconductivity[64] is a pressing question in present condensed matter physics[125–127].

To highlight the purpose of studying electron-nematic phases, we explain what are of importance and interest. They are summarized in three points below.

- *To elucidate quantum criticality unique to electron-nematicity:* To investigate the low energy properties of quantum phase transitions and quantum criticality is interesting problem in itself, as exemplified by bond orders, orbital orders. The electron-nematic quantum criticality leads to an unusual non-Fermi liquid behavior[125, 128–130], beyond the standard Hertz-Millis-Moriya description[129, 131–133]. Furthermore, because the nematic order parameter couples linearly to acoustic phonon, phonon modes affect the thermodynamic and transport properties [134–136].
- *To reveal the microscopic origins of unconventional superconductors:* Recent studies have elucidated that critical order parameter fluctuations [137–140], namely charge-, orbital-, spin-, and multipole- fluctuations, lead to various unconventional superconductors. As an important issue to investigate the microscopic mechanism of unconventional superconductor, the electron-nematicity has attracted much attention in many exotic superconductors. One of the great interests is why the electron-nematic states emerge so ubiquitously in many unconventional superconductors.
- *To clarify the notion of the order by fluctuation:* Order parameter fluctuation enriches quantum states of matter. The vestigial order[126, 127, 141–144], which is caused by symmetry breaking order parameter fluctuation, is one of the theoretical concepts to understand the intertwined ordered states. It is an important issue to clarify in which materials these ordered phases are realized.

TBG is an interesting material whose topology and interaction can be varied by a new control parameter, the twist angle. While ordinary graphene based materials are composed of carbon, a light element, MATBG has strong electron-electron interaction due to the quasi-flat band structure caused by the moiré interference pattern. Notably, some exotic phenomena[145–158] are reported such as unconventional superconductors near

Mott insulating phases, quantum Hall ferromagnetism and electron-nematic phases, at the first magic angle. The closer relationship[144, 159–163] between the electron correlation and the topological properties is very important to understand physical properties of this material.

In the case of MA-TBG, an electron-nematic state, which breaks the lattice C_{3z} symmetry, has been detected by scanning tunneling microscopy[164–166] and transport measurements [167]. This C_{3z}-broken electron-nematic state, referred to as a three-state Potts nematic state, is of interest for its competition with nematic superconductivity[167] and for the mystery of the Landau level degeneracy[167–169] in different regions of its phase diagram[165, 167]. From a theoretical point of view[162, 169–174], it has been pointed out that unique properties of the moiré phonon, which reflect a non-rigid crystal[175, 176], assist a nematic phase transition[171] and microscopic origin of this nematic state is attributed to the interference of the valley+spin fluctuation[174].

Moreover, in the case of doped-Bi_2Se_3, which is a candidate material of nematic superconductors and topological superconductors [177–185], a three-state Potts nematic state has been reported[186–188] above the superconducting transition temperature. Although this seems to contradict the nematic superconductivity for which an order parameter is accompanied with a breaking of the lattice point group symmetry, it is pointed out that this nematic state is a vestige[126] of the nematic superconductivity[127, 143, 188] caused by the strong superconducting fluctuation. Besides the relationship between nematicity and superconductivity, it is also important to identify the critical behavior of electron-nematic states and to distinguish whether it is intrinsic (i.e. induced spontaneously) or extrinsic (i.e. due to trivial strains or the structural distortion). Despite a lot of research, the identification of such a three-state Potts nematic state and the clarification of whether it is induced spontaneously or from trivial strains are not an easy task.

1.3 New theoretical perspective of non-Hermitian topology

In this section, we give an brief introduction to non-Hermitian physics in equilibrium strongly correlated electron systems.

Recent studies have revealed another kind of interesting topological phase described by a non-Hermitian Hamiltonian [34–36, 189–195, 195–209]. In standard textbooks of quantum mechanics, we learn that the Hamiltonian is represented by a Hermitian operator. The Hermiticity of the Hamiltonian ensures that the eigenvalues of a Hamiltonian are real and bounded below in closed systems. This situation is also true when considering quantum many-body systems, but in open or/and nonequilibrium systems, where the interaction with environments cannot be neglected, non-Hermitian operators give an effective description[34–36].

Non-Hermitian phenomena have been studied and realized in various contexts (e.g. photonic systems, open quantum systems, etc). Moreover, motivated by recent development of topological band theory, the interplay between topology and non-Hermiticity has also attracted much attention in a non-Hermitian extension of topological insulators/semimetals.

Non-Hermitian band theory in strongly correlated systems

A unique feature of non-Hermitian systems is that the energy spectrum becomes complex number. When discussing topological natures of the energy band, the gap structure becomes important. Two types of gap structures[203, 209], i.e. point gap and line gap, are defined in non-Hermitian systems. When the complex spectrum does not cross a reference point (line) in the complex-energy plane, a point (line) gap is open. While the point gap is closed, the line gap is always closed, but conversely, when the point gap is open, the line gap is not always open.

It is well known that the topological structure in gapped systems also plays an important role in gapless topological systems. A topologically protected gapless structure, i.e. point or line, is caused by a change of some topological number. For example Weyl points in three-dimensions are protected by the Chern number in embedded some two-dimensional systems. In non-Hermitian systems, due to the gap structure on the complex energy plane, such a gapless structure or a band degeneracy appears in two distinct situations: when the line gap is open and when it is closed[210]. While the former includes band degeneracies such as Dirac/Wely points in Hermitian systems, the latter shows band degeneracies which have no Hermitian counterpart, e.g. exceptional points[201, 210, 211].

A distinctive property of an exceptional point is swapping of eigenenergies and eigenstates upon its encirclement, and it is characterized by the non-zero winding number on the complex energy plane. It is also a topologically stable band degeneracy and is robust to perturbations. Such emergent exceptional points of non-Hermitian effective Hamiltonian give rise to an open Fermi surface[210, 212–227] such as a "Fermi arc" in the energy spectrum. More precisely, these exceptional points always appear in pairs, and a Fermi arc appears in the bulk band structure to connect the exceptional points. This is one of the unique properties of non-Hermitian systems. Experimentally, Weyl exceptional ring[215] and a bulk Fermi arc accompanied with a pair of exceptional points[214] have been observed in optical wavequide array or photonic crystal slab.

Furthermore, it has been pointed out that the symmetry enriches[210, 224–227] the possible shapes of exceptional points and the Fermi arcs. To date, various non-Hermitian topological semi-metals have been proposed [215–224]. For example, in two dimensions, the exceptional points form symmetry-protected exceptional rings and they induce Fermi planes, which have also been experimentally observed in a two-dimensional photonic crystal slab[194] with PT symmetry. In three dimensions, they form symmetry-protected exceptional surfaces enclosing the region where the band gap becomes pure-imaginary.

Even in equilibrium systems, as pointed out by V. Kozii and L. Fu[37], non-Hermitian band structures are naturally formed by the quasi-particle lifetime originating from the self-energy of electron Green's functions. If we describe the energy spectrum of quasi-particles having the complex self-energy in terms of an effective Hamiltonian defined as $H_{\rm eff}(\boldsymbol{k}) = H_{\boldsymbol{k}} + \Sigma^{\rm R}(\omega + i\delta, \boldsymbol{k})$ with the complex self-energy $\Sigma^{\rm R}(\omega + i\delta, \boldsymbol{k})$, non-Hermitian physics related to exceptional points and the bulk Fermi arc naturally show up in strongly correlated systems, such as the Kondo lattice model, the periodic Anderson model [38–42, 228–236]. One of the most important points is that the bulk Fermi arc structure can be observed in the single-particle spectral function $A(\omega, \boldsymbol{k}) = -\frac{1}{\pi}{\rm Im}{\rm Tr}G^{\rm R}(\omega + i\delta, \boldsymbol{k})$ with the reterded Green's function

$$G^{\rm R}(\omega + i\delta, \boldsymbol{k}) \;\; = \;\; \left[(\omega + i\delta)\mathbb{1} - H_{\rm eff}(\boldsymbol{k})\right]^{-1}. \tag{1.2}$$

The non-Hermitian perspective in equilibrium system has attracted much attention

because of the potential to solve open questions in condensed matter physics, such as the mystery of quantum oscillation in bulk Kondo insulators[236]. In spite of the intensive studies, it remains unclear what physical properties are affected by the non-Hermitian band structure. In particular, there are few studies elucidating effects of the non-Hermitian band structure on magnetic/electric responses.

1.4 Overview of the thesis

In this thesis, we investigate physical properties of the correlation-induced topological states and their various phase transitions. We first overview the contents of this thesis.

In Chapter 2, we explore the topological semimetallic states in 2D antiferromagnetically/ferromagnetically ordered heavy-fermion systems to take into account crystal symmetries and demonstrate how they can emerge by using the Hartree-Fock approximation. We show that antiferromagnetic topological insulating phases are stabilized at half-filling of periodic Anderson model. We also show topological half-metallic ferromagnetic states stabilized around quarter filling. Our scenario can even apply for spin-nonconserving systems in the presence of spin-orbit coupling.

In Chapter 3, we investigate emergent non-Hermitian properties in strongly correlated nodal-line semimetals with chiral symmetry, and discuss their impact on bulk quantities such as the magnetic susceptibility. We elucidate the emergence of the Fermi volume enclosed by a symmetry-protected exceptional torus for a diamond lattice model with spatially modulated Hubbard interaction by employing the dynamical mean-field approximation combined with iterated perturbation theory. Furthermore, in order to investigate the effect of low energy states induced by non-Hermiticity on physical quantities, we calculate a sublattice dependent magnetic susceptibility. Specifically, we find that, due to the emergence of the Fermi volume, the magnetic susceptibility for B-sublattice becomes larger than that for A-sublattice, although the interaction strength is opposite. For this counterintuitive response to the homogeneous magnetic field, the chiral symmetry is essential, leading to the enhancement of local density of state at the Fermi level only for B-sublattice.

In Chapter 4, we investigate the impact of critical nematic fluctuations on acoustic phonon, which in turn enables us to identify the nematic properties by ultrasound attenuation experiments. We propose to detect the intrinsic three-state Potts nematic phase transition by measuring the ultrasound attenuation of the transverse acoustic phonon. Namely ultrasound attenuation coefficient shows an isotropic divergence and the sound velocity renormalization also shows an isotropic angle dependence. In addition, we determine the phase diagram by an extended Hubbard model in a mean-field approximation to investigate the critical properties. The order of phase transition is of weak first-order. Furthermore, it is confirmed that the enhancement of the ultrasound attenuation coefficient can be observed in the case of a weak first-order phase transitions.

Finally, we conclude this thesis and explain our outlook in Chapter 5.

Chapter 2

Topological properties of magnetically ordered heavy-fermion systems in the presence of mirror symmetry

2.1 Introduction to this chapter

In this chapter, we focus on the topological properties in long-range-ordered phases such as ferromagnetic (FM) and antiferromagnetic (AFM) phases. The emergence of topological properties in the magnetic phases has already been studied. Magnetic topological insulators have attracted much attention in terms of the emergence of chiral edge modes and their applications to low-power electronics/spintronics devices. As we have mentioned in Sec. 1.2.2, it has been observed that magnetic-impurity doped topological insulators become ideal Chern insulators. However, there have been still some problems to be solved, such as low transition temperatures and non-uniformity of the sample in the case of magnetically doped insulators. One solution is to search for bulk-magnetic topological insulators. Therefore, epanding the platform of magnetic topological insulators has been required. Here, we focus on heavy-fermion systems, which are expected to have topological properties and various magnetic orders.

For example, an antiferromagnetic topological insulator (AFTI) [80], which is characterized by the combined symmetry of time-reversal and lattice translation, has been proposed for three-dimensional (3D) systems. However, this topological state is allowed only for 3D systems[118, 120, 121]. We here attempt to solve this problem and demonstrate that we can realize AFTIs even in two-dimensional (2D) systems by taking into account a mirror symmetry. Moreover, in a bulk FM phase, a spin-selevtive topological insulator (SSTI), which is a topological insulator in half-metallic states, was proposed for heavy-fermion systems [88]. This half-metallic FM phase [113–117] is stabilized around quarter filling, where one spin sector acquires a gap while the other remains gapless, which is called a spin-selective gap. SSTI is characterized by a nontrivial topology in the insulating sector. However, as pointed out in previous studies, spin conservation is important, and the problem is that it cannot be applied in the presence of general spin-orbit coupling. Here, we will overcome this difficulty and propose a way to realize an SSTI for a spin-nonconserving system in the presence of spin-orbit coupling.

We explore the above-mentioned topological states in 2D magnetically ordered phases by using an effective model of the topological Kondo insulator for heavy-fermion systems, and demonstrate how they can emerge by using the Hartree-Fock (HF) approximation.

Our main idea for realizing such topological states in 2D magnetic phases is to take into account crystal symmetries, in particular, a mirror symmetry. We address two kinds of magnetic phases: a 2D AFM phase at half filling and a half-metallic FM phase around quarter filling. By taking into account the mirror symmetry, we elucidate the remarkable facts that a 2D AFM phase can have a topologically nontrivial structure specified by a mirror Chern number and that a half-metallic FM phase can have a topologically nontrivial structure specified by a Chern number. An important point is that these states can appear for spin-nonconserving systems.

This chapter is organized as follows. In Sec. 2.2, we introduce the topological periodic Anderson model and the method to calculate the Chern number. In Sec. 2.3, we show the numerical results for magnetically ordered topological insulating/half-metallic states. We then discuss the results for an AFTI at half filling in Sec. 2.3.1, and a half-metallic FM topological state near quarter filling in Sec. 2.3.2. In Sec. 2.3.3, we briefly commnet on the electron correlation effect on our topological phases. Sec. 2.4 is devoted to the summary of this chapter. Finally, in Sec. 2.5, we note for some formulas.

2.2 Mean-field theory of topological periodic Anderson model on the square lattice

We explore the topological properties of the heavy-fermion systems by employing a 2D periodic Anderson model with nonlocal d-f hybridization [1][6, 8, 237, 238]. Specifically, we analyze the following topological periodic Anderson model showing band inversion at X points [239–242] due to next-nearest-neighbor (n.n.n.) hopping, which is important for describing bulk SmB_6. In addition to the strong interaction U_f between f-electrons, we also consider the interaction U_d between d-electrons. The Hamiltonian reads

Periodic Anderson model

$$H = \sum_{\boldsymbol{k}} \begin{pmatrix} d_{\boldsymbol{k}}^\dagger & f_{\boldsymbol{k}}^\dagger \end{pmatrix} \begin{pmatrix} \epsilon_{\boldsymbol{k}}^d & V_{\boldsymbol{k}} \\ V_{\boldsymbol{k}}^\dagger & \epsilon_{\boldsymbol{k}}^f \end{pmatrix} \begin{pmatrix} \boldsymbol{d}_{\boldsymbol{k}} \\ \boldsymbol{f}_{\boldsymbol{k}} \end{pmatrix} + \sum_{j;\alpha(=d,f)} U_\alpha n_{j\uparrow}^\alpha n_{j\downarrow}^\alpha, \tag{2.1a}$$

with

$$\epsilon_{\boldsymbol{k}}^d = [-2t_d(\cos k_x + \cos k_y) - 4t_d' \cos k_x \cos k_y]\sigma_0, \tag{2.1b}$$
$$\epsilon_{\boldsymbol{k}}^f = [\epsilon_f - 2t_f(\cos k_x + \cos k_y) - 4t_f' \cos k_x \cos k_y]\sigma_0, \tag{2.1c}$$
$$V_{\boldsymbol{k}} = -2[\sigma_x \sin k_x (V_1 + V_2 \cos k_y) + \sigma_y \sin k_y (V_1 + V_2 \cos k_x)], \tag{2.1d}$$

where $\epsilon_{\boldsymbol{k}}^d(\epsilon_{\boldsymbol{k}}^f)$ is the dispersion of d-(f-) electrons, $V_{\boldsymbol{k}}$ is a Fourier component of the nonlocal d-f hybridization, and $\boldsymbol{k}$ is a wave number.

The annihilation operators are defined as $\boldsymbol{d}_{\boldsymbol{k}} = \begin{pmatrix} d_{\boldsymbol{k}\uparrow} & d_{\boldsymbol{k}\downarrow} \end{pmatrix}^T$ and $\boldsymbol{f}_{\boldsymbol{k}} = \begin{pmatrix} f_{\boldsymbol{k}\uparrow} & f_{\boldsymbol{k}\downarrow} \end{pmatrix}^T$. The basis function for this model is $(d_\uparrow, d_\downarrow, f_\uparrow, f_\downarrow)^T$, where $\sigma_i (i = 0, x, y, z)$ are the Pauli matrices for spins. Here, t_d, t_f, t_d', and t_f' are hopping parameters, V_1 and V_2 denote the d-f hybridization, and ϵ_f is the difference between the d- and f-electron energies. We consider the above model on a 2D square lattice in the x-y plane, which is a 2D version of

[1] Spatial inversion symmetry prohibits a local hybridization between orbitals of different parity.

the topological crystalline insulator with non-trivial mirror chern number[237, 238]. The system has inversion symmetry, so that the hybridization has odd parity, $V_{\boldsymbol{k}} = -V_{-\boldsymbol{k}}$.

In order to study the ground state of the model in Eq. (2.1), we employ the following HF approximation for the Coulomb term:

$$n^{\alpha}_{i\uparrow} n^{\alpha}_{i\downarrow} \sim n^{\alpha}_{i\uparrow} \langle n^{\alpha}_{i\downarrow} \rangle + \langle n^{\alpha}_{i\uparrow} \rangle n^{\alpha}_{i\downarrow} - \langle n^{\alpha}_{i\uparrow} \rangle \langle n^{\alpha}_{i\downarrow} \rangle, \tag{2.2}$$

where $n^{\alpha}_{i\sigma} (\alpha = d, f)$ is the number operator. Here, $\langle \cdots \rangle$ denotes the expectation value at zero temperature.

We introduce the mirror operation M_z, which inverts the z-axis,

$$M_z = i\,\tau_z \otimes \sigma_z, \tag{2.3}$$

where $\tau_i (i = 0, x, y, z)$ are the Pauli matrices for two-orbitals, d- and f-electrons. In order to consider the magnetically ordered topological insulating states with a mirror symmetry, we introduce the corresponding topological number. First, recall that the Chern number in multiband systems is given as

Chern number

$$C = \frac{1}{2\pi} \sum_i \int_S [\nabla_{\boldsymbol{k}} \times \mathcal{A}_i]_z dk_x dk_y, \tag{2.4}$$

where $\mathcal{A}_i(\boldsymbol{k}) = -i\langle u_i(\boldsymbol{k}) | \nabla_{\boldsymbol{k}} | u_i(\boldsymbol{k}) \rangle$ is the $U(1)$ Berry connection, where $|u_i(\boldsymbol{k})\rangle$ is a Bloch state with occupied band index i, which is an eigenstate of $\mathcal{H}(\boldsymbol{k})$.

In the mirror-symmetric system, all the eigenstates are characterized by their mirror parities and divided into two subspaces as

$$\mathcal{H}(\boldsymbol{k}) = \begin{pmatrix} \mathcal{H}_{M_z=+i}(\boldsymbol{k}) & 0 \\ 0 & \mathcal{H}_{M_z=-i}(\boldsymbol{k}) \end{pmatrix}. \tag{2.5}$$

The net Chern number C and the mirror Chern number C_m are defined by the Chern numbers $C_{\pm i}$ obtained in each mirror subspace, namely,

$$C = C_{M_z=+i} + C_{M_z=-i}, \tag{2.6a}$$
$$C_m = (C_{M_z=+i} - C_{M_z=-i})/2. \tag{2.6b}$$

2.3 Numerical results of magnetically ordered topological states

We here discuss the obtained results for the magnetic phases at half filling and around quarter filling separately. The values of the parameters we employ in the following are $t_d = 1$ (energy unit), $t'_d = -0.5, t_f = -t_d/5, t'_f = -t'_d/5, U_d = 2$. Unless otherwise noted we set $(V_1, V_2) = (0.1, -0.4)$. The choice of these parameters will be explained below. The magnetic properties of the system are studied by the HF method and the Chern number is calculated by the Fukui-Hatsugai method[243], which is efficient for numerical calculations.

2.3.1 Antiferromagnetic topological insulator/semimetal

For a heavy-fermion system at half filling, there are some AFM phases and a Kondo insulating phase in the ordinary Doniac phase diagram. In contrast to a previous study [80], we here demonstrate that the AFTI can emerge in 2D mirror-symmetric systems. The model we employ here is a topological mirror Kondo insulator introduced in Refs [237, 238, 244], which is a mirror-symmetric extension of the topological Kondo insulator. This model was previously used to address a nonmagnetic Kondo insulating phase. The net Chern number is zero, $C = 0$, because of the time-reversal symmetry, but there is still a possibility of having a non-zero mirror Chern number $C_m \neq 0$. We elucidate below that the system can change from a paramagnetic phase to an AFM phase without breaking its mirror symmetry, thus leading to an AFTI. The AFM phase, where the magnetization is along the z-axis in our case, breaks a space translation symmetry $T_{1/2}$, and thus the period of the unit cell is doubled. Time-reversal symmetry is also broken by the magnetization, but we show that the net Chern number is zero by using the combined symmetry $S = \Theta T_{1/2}$ of the time-reversal Θ and primitive-lattice translation $T_{1/2}$.

We assume that the nesting vector is $\boldsymbol{Q} = (\pi, \pi)$ for the AFM phase, which is justified for $(t'_d, t'_f, V_2) = (0, 0, 0)$, see below. The mean-field Hamiltonian is given by

$$\mathcal{H}^{mf}_{\boldsymbol{k}} = \begin{pmatrix} \epsilon^d_{\boldsymbol{k}} + h^d_{int} & V_{\boldsymbol{k}} \\ V^\dagger_{\boldsymbol{k}} & \epsilon^f_{\boldsymbol{k}} + h^f_{int} \end{pmatrix}, \tag{2.7a}$$

with

$$\epsilon^d_{\boldsymbol{k}} = [-2t_d(\cos k_x + \cos k_y)\eta_x - 4t'_d \cos k_x \cos k_y \eta_0]\sigma_0, \tag{2.7b}$$

$$\epsilon^f_{\boldsymbol{k}} = [\epsilon_f \eta_0 - 2t_f(\cos k_x + \cos k_y)\eta_x - 4t'_f \cos k_x \cos k_y \eta_0]\sigma_0, \tag{2.7c}$$

$$V_{\boldsymbol{k}} = -2[\sin k_x \cdot \sigma_x(V_1\eta_x + V_2\eta_0 \cos k_y) + \sin k_y \cdot \sigma_y(V_1\eta_x + V_2\eta_0 \cos k_x)], \tag{2.7d}$$

$$h^\alpha_{int} = U_\alpha \begin{pmatrix} \langle n^{A\alpha}_{0\downarrow}\rangle & 0 & 0 & 0 \\ 0 & \langle n^{B\alpha}_{0\downarrow}\rangle & 0 & 0 \\ 0 & 0 & \langle n^{A\alpha}_{0\uparrow}\rangle & \\ 0 & 0 & 0 & \langle n^{B\alpha}_{0\uparrow}\rangle \end{pmatrix}, \tag{2.7e}$$

where $\alpha = d, f$, and $\eta_i (i = 0, x, y, z)$ are the Pauli matrices for sublattice indices. The basis function is $(d^A_\uparrow, d^B_\uparrow, d^A_\downarrow, d^B_\downarrow, f^A_\uparrow, f^B_\uparrow, f^A_\downarrow, f^B_\downarrow)^T$. The mirror operation in the sublattice is

$$M_z = i\,\tau_z \otimes \sigma_z \otimes \eta_0. \tag{2.8}$$

Symplified model calculation: Case of $(t'_d, t'_f, V_2) = (0, 0, 0)$

In order to see the essence of the results more clearly, we start with a simplified model having only nearest-neighbor (n.n.) hopping and hybridization, i.e., $(t'_d, t'_f, V_2) = (0, 0, 0)$. We first determine the easy axis of the magnetization by using second-order perturbation theory in the strong correlation limit. As a result, we conclude that the z-direction is the easy axis. The detail of the derivation is given in Sec. 2.5.2. It turns out that the magnetic moments of f- and d-electrons align antiparallel at each site in the z-direction, as shown in Fig. 2.1(a).

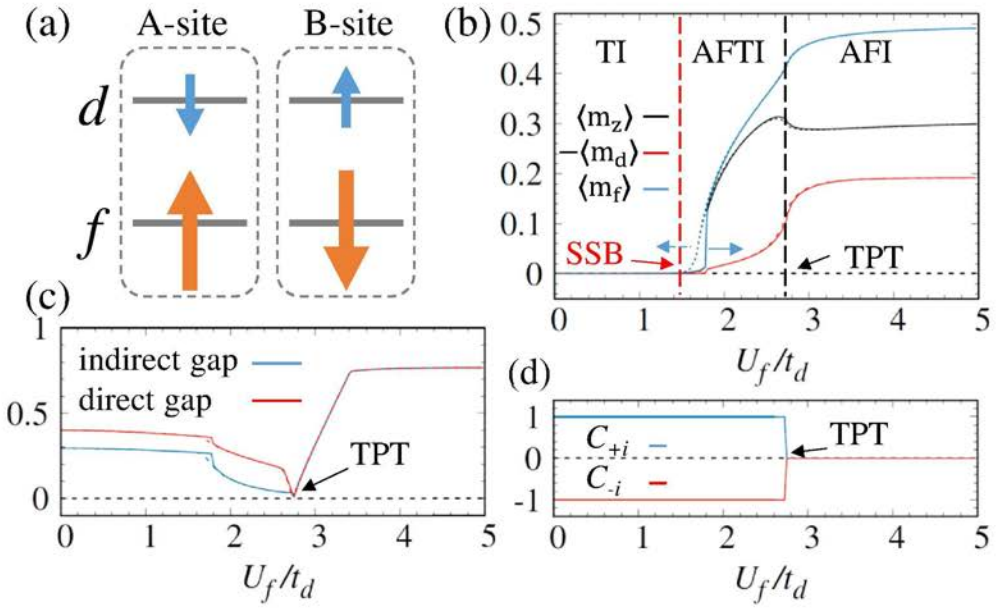

Fig. 2.1: Magnetic and topological properties for a simplified model with only n.n. hopping and interaction, $(t'_d, t'_f, V_2) = (0,0,0)$ and $(U_d, V_1) = (2.0, 0.1)$, obtained with the HF approximation: (a) spin configuration of the AFM phase, (b) staggered magnetic moments, (c) indirect gap and direct gap, (d) Chern number for each sector. In (b), the red dashed line denotes a spontaneous symmetry breaking (SSB) transition, the black dashed line denotes a topological phase transition (TPT), and there is a small hysteresis loop because of the first-order transition. In (c), the indirect gap is the band gap between the conduction and valence bands $\min(E_{\boldsymbol{k}}^{\text{conduction}} - E_{\boldsymbol{k}'}^{\text{valence}})$ ($\boldsymbol{k}$ is not necessarily equal to $\boldsymbol{k}'$) while the direct gap is the band gap at wave number $\boldsymbol{k}$ $\min(E_{\boldsymbol{k}}^{\text{conduction}} - E_{\boldsymbol{k}}^{\text{valence}})$, where indirect gap $\leq$ direct gap. We have a TI for $U_f < 1.42$, an AFTI for $1.42 < U_f < 2.72$, and an AF trivial insulator (AFI) for $2.72 < U_f$. Except when $U_f = 2.72$, the system is an insulator because of the finite indirect gap. Reprinted figure with premission from [245] Copyright 2018 by the Journal of the Physical Society of Japan.

The mean-field results for $(U_d, V_1) = (2, 0.1)$ are summarized in Figs. 2.1 (b)- 2.1 (d). Note that the results are not sensitive to the value of V_1. We obtain an AFTI phase as shown in Fig. 2.1(b). At $U_f = 2.72$, there is a first-order magnetic phase transition, and the spin configuration for $U_f > 2.72$ in Fig. 2.1(a), where d- and f-electrons align in the opposite directions, is in accordance with the second-order perturbation analysis. We show the direct and indirect gaps in Fig. 2.1(c). The former is important for determining the topological structure, and we confirm that there is indeed a finite direct gap in the AFM phase. Note that the phase transition in Fig. 2.1(c) is a Lifshitz transition, where gap closing seems to occur at a single point. However, this is an accidental phenomenon due to our choice of parameters. It is seen that the AFTI phase extends between $U_f = 1.42$ and $U_f = 2.72$, where the mirror Chern number takes a value of $C_m = 1$ in Fig. 2.1(d) with the finite magnetization in Fig. 2.1(b). In the strong interaction region, there is a topological phase transition to a trivial phase at $U_f = 2.72$, where both the direct and indirect gaps are closed. As seen from Fig. 2.1(d), the transition is accompanied by a change in the mirror Chern number from $C_m = 1$ to $C_m = 0$ while the net Chern number is zero. This topological phase transition is triggered by the competition between the two

types of gap. Namely, in the weak interaction region, the topologically nontrivial gap due to the nonlocal hybridization V_1 is dominant, while in the strong interaction region, the topologically trivial gap with the AFM order is dominant. The competition between the two different states gives rise to a topological phase transition accompanied by gap closing. We show details of competing behaviour in the next subsection.

Competition between two types of energy gap: Case of $(t'_d, t'_f, V_2) = (0, 0, 0)$

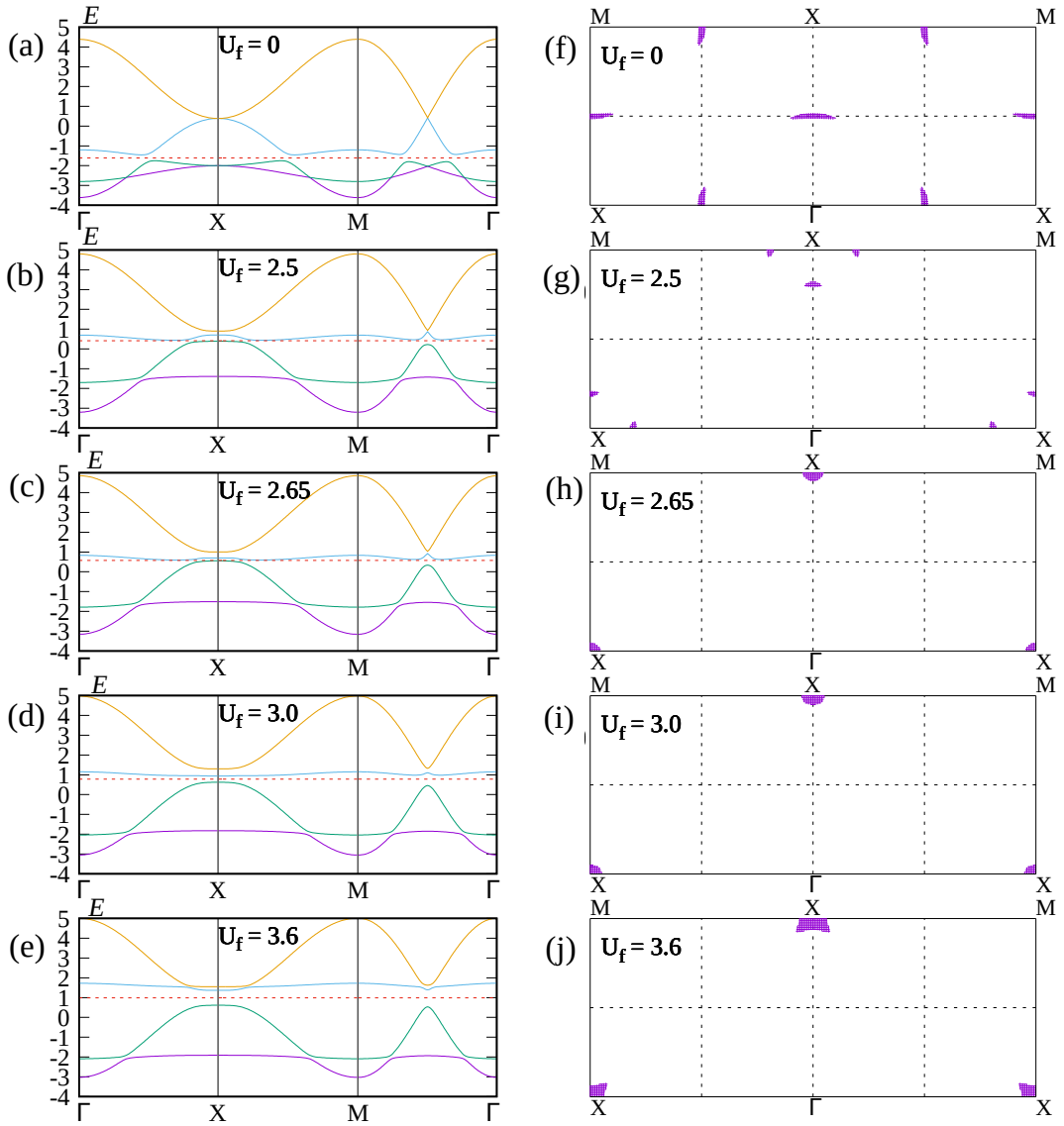

Fig. 2.2: U_f dependences of gap structure for a simplified model with only n.n. hopping and interaction, $(t'_d, t'_f, V_2) = (0, 0, 0)$ and $(U_d, V_1) = (2.0, 0.1)$, obtained with the HF approximation. Energy spectra: (a) $U_f = 0$, (b) $U_f = 2.5$, (c) $U_f = 2.65$, (d) $U_f = 3.0$, (e) $U_f = 3.6$. The red dashed line denotes the position of the chemical potential. Corresponding wave number that brings about the lowest direct gap: (f) $U_f = 0$, (g) $U_f = 2.5$, (h) $U_f = 2.65$, (i) $U_f = 3.0$, (j) $U_f = 3.6$. Reprinted figure with premission from [245] Copyright 2018 by the Journal of the Physical Society of Japan.

Here, we investigate the competition between two types of gap, topologically trivial and nontrivial gaps, in a simplified model with only n.n. hopping and interaction,

$(t'_d, t'_f, V_2) = (0,0,0)$ and $(U_d, V_1) = (2.0, 0.1)$. There are two origins of this competition, one is the shift of the f-band $U_f \langle n_{0\sigma}^{AorB\alpha} \rangle$ and the other is the change in the nonlocal hybridization $V_{\boldsymbol{k}}$.

We first note that the Hamiltonian [Eq. (2.7)] can be block-diagonalized for two mirror sectors in the presence of mirror symmetry. We focus on one of the mirror sectors because both have the same band structure. The sector $M_z = +i$ is constructed from $(d_\uparrow^A, d_\uparrow^B, f_\downarrow^A, f_\downarrow^B)$ while the sector $M_z = -i$ is constructed from $(d_\downarrow^A, d_\downarrow^B, f_\uparrow^A, f_\uparrow^B)$. At $U_f = 0$, a band inversion occurs between the second and third bands from the bottom in Fig. 2.2(a). Here, for simplicity, four bands are labeled as follows; the first and fourth bands from the bottom originate from d-electrons, whereas the second and third bands originate from f-electrons. The insulating phases are classified according to the band structure; (i) a band inversion occurs between the second and third bands, and the chemical potential lies between these d- and f-bands, (ii) a band inversion does not occur and the chemical potential lies between the d- and f-bands, and (iii) the chemical potential lies between different d-bands. The first type (i) has the nontrivial topological structure shown in Figs. 2.2(a)- 2.2(c), whereas the second type (ii) in Fig. 2.2(d) and the third type (iii) in Fig. 2.2(e) do not have nontrivial topological structures.

Next, we discuss the shift of the f-band, which is the Hartree shift due to the interaction U_f. To this end, it is sufficient to consider the Hartree shift in sublattices A and B only for one of the mirror sectors. The linear dependence of the direct gap on U_f after the TPT in Fig. 2.1(c) can be understood by this Hartree shift, as described below. Before the TPT, the chemical potential is between the inverted d- and f-bands but after the TPT, the chemical potential is between the non-inverted d- and f-bands or between the d-bands. In the region where the chemical potential lies between the inverted d- and f-bands, the direct gap proportional to the Hartree shift for one of the f-bands causes the linear dependence on U_f as seen in Fig. 2.1(c). On the other hand, when the chemical potential lies between different d-bands, the direct gap is not affected by the Hartree shift for the f-band, leading to an almost unchanged gap size. Since the direct gap caused by the Hartree shift does not have a topologically nontrivial structure, the system is topologically trivial.

The above explanation becomes much clearer if we take into account the effect of the nonlocal hybridization $V_{\boldsymbol{k}}$, which is an odd function of $\boldsymbol{k}$. An important point is that $V_{\boldsymbol{k}}$ vanishes at the X points ($V_{\boldsymbol{k}=\mathrm{X}} = 0$), which allows us to understand the characteristic behavior, in particular, in the region before the TPT in Fig. 2.1(c). By calculating the wave number dependence of the gap size, we determine the wave number that gives the smallest direct gap in Figs. 2.2(f)-2.2(j). At $U_f = 0$, this wave number is located in the middle between the Γ and X points. With increasing U_f, the band structure around the Fermi level is changed by the Hartree shift as in Figs. 2.2(b), and 2.2(c) and the above-mentioned wave number approaches the X point in Fig. 2.2, making the gap size smaller. This is because around the X point the hybridization $V_{\boldsymbol{k}}$ becomes small, and therefore the direct gap rapidly decreases around the TPT in Fig. 2.1(c). Just after the TPT, the above wave number is still located around the X point in Figs. 2.2(i) and 2.2(j). Thus, the direct gap is caused only by the Hartree shift, giving rise to a linear dependence on U_f, as already mentioned above.

2D effective model for SmB_6: Case of $(t'_d, t'_f, V_2) = (-0.5, 0.1, -0.4)$

We now investigate the model with a specific choice of the parameters, $(t'_d, t'_f, V_2) = (-0.5, 0.1, -0.4)$. Importantly, these parameters can describe band inversions for the

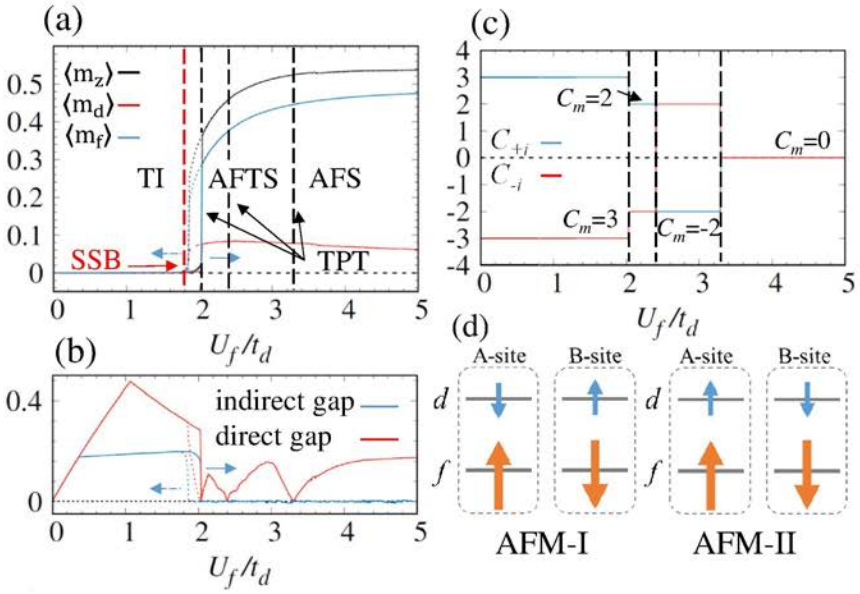

Fig. 2.3: Magnetic and topological properties for the effective model of SmB_6, $(t'_d, t'_f, V_2) = (-0.5, 0.1, -0.4)$ and $(U_d, V_1) = (2.0, 0.1)$ at half filling: (a) staggered magnetic moments, (b) indirect gap and direct gap, (c) Chern number for each sector, (d) spin configurations of the two AFM phases. In (a), there is a small hysteresis loop because of the first-order transition. In (b), the region where the indirect gap is closed is semimetallic, and the points where the direct gap is closed denote the topological phase transitions. In (c), there are two Chern numbers for two mirror sectors, and the change in the Chern numbers signals the topological phase transition. We have an AF topological semimetal (AFSM) for $1.8 < U_f < 3.25$ and an AF trivial semimetal (AFS) for $U_f < 3.25$. Reprinted figure with premission from [245] Copyright 2018 by the Journal of the Physical Society of Japan.

X points in the 3D Brillouin zone (see Appendix 2.5.1), leading to a strong topological insulator phase, as observed for SmB_6 via angle-resolved photoemission spectroscopy measurements [96, 97]. The results obtained for topological and magnetic properties at half filling are shown in Fig. 2.3(a). A prominent feature in this model is that the system becomes metallic where the indirect gap is closed in the AFM phase even at half filling, as seen in Fig. 2.3(b). Note, however, that the topological properties still remain intact in this region because the direct gap is not closed. Namely, the Chern number is still well defined [Fig. 2.3(c)] in the region where the direct gap is open. Thus, the topological properties remain even in a "metal", and such a metal adiabatically connected to a topological insulator is called a topological semimetal. Note that this definition of a semimetal is standard in condensed matter but slightly different from that for Dirac/Weyl semimetals, which are zero-gap semiconductors by definition. Finally, there are several topological phase transitions between different Chern numbers, as seen in Fig. 2.3(c). This spin configuration is of the AFM-II type in Fig. 2.3(d).

Summarizing all these results, we arrive at the phase diagram shown in Fig. 2.4(a). The horizontal axis denotes the strength of the interaction U_f and the vertical axis the strength of hybridization V_1. There are two AFM phases in Fig. 2.4(a). The above analysis for the dashed blue line in Fig. 2.4(a) ($V_1 = 0.1, V_2 = -0.4$) also applies to the region $|V_1| < |V_2|$ where the spin configuration is of the AFM-II type. In the AFM phase for these parameters, a semimetallic AFM topological phase is realized, which we refer

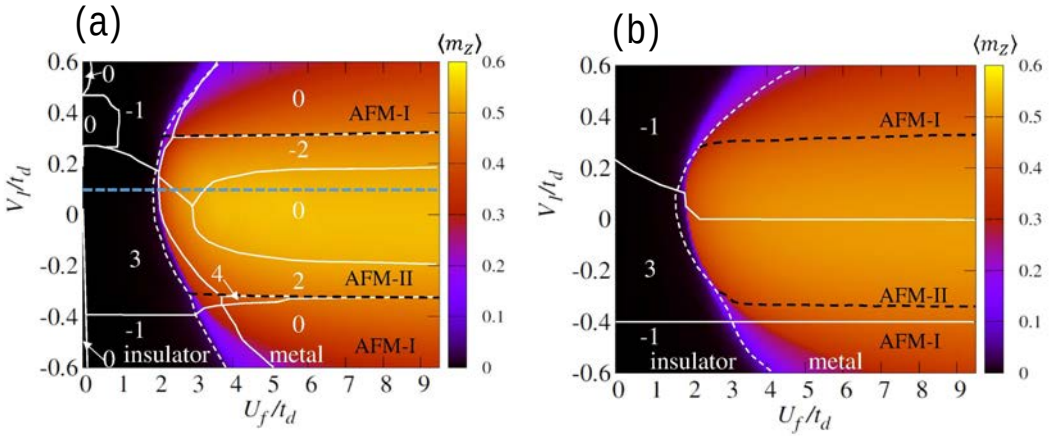

Fig. 2.4: Phase diagram of mirror-symmetric AFTI at half filling as a function of the interaction U_f and hybridization V_1: (a) $U_d = 2$, (b) $U_d = 0$. The white (dashed) line denotes the topological (insulator-metal) phase transition line and the black dashed line separates two AFM phases, i.e., AFM-I and AFM-II. We set $V_2 = -0.4$. In the metallic region, the indirect gap is closed; thus, there is a Fermi surface. However, the direct gap at the same wave number $\boldsymbol{k}$ is not closed; thus, the Chern number is still well defined. The white numbers are mirror Chern numbers. The mirror Chern numbers are 4, 3, 2, 0, -1, and -2 in two figures. The color plot shows the strength of the magnetization. Reprinted figure with premission from [245] Copyright 2018 by the Journal of the Physical Society of Japan.

to as an AFM topological semimetal. The mirror Chern number has various values in the phase diagram, which is due to the presence of n.n.n. hopping and hybridization, and is enriched by U_d. The changes in the mirror Chern number are driven by the shift of the f-band. In general, a complex band structure brings about various topological numbers (mirror Chern numbers), for example, see Refs. [30] and [244].

For reference, we show the phase diagram for $U_d = 0$. The obtained phase diagram is shown in Fig. 2.4(b). In contrast to the case with finite U_d shown in Fig. 2.4(a), the phase diagram is much simpler and we also find nontrivial topological states in a wider region. Comparing the two phase diagrams, the both band structures have the non-trivial topology in paramagnetic phases, but in the ordered phase, the situation is different. When we change U_d, various topological phase transition occur even within the antiferromagnetic phase. Thus we conclude that finite U_d is detrimental to topological properties in AFM phases. The reason why these deferences occur that a finite value of U_d contributes to opening the gap between the d-bands, which leads to the topologically trivial band structure in the AFM phase, as shown in the simplified model (see Figs. 2.2).

Here some comments on the difference between the current results and the previous ones are in order. So far, topological properties with the AFM order have been studied in Refs. [73, 84–87], focusing on the systems with spin $U(1)$ symmetry. The Hamiltonian with spin $U(1)$ symmetry can be block-diagonalized for two spin sectors. In such a case, the topology of the AFM phase is characterized by the spin Chern number. In the presence of spin-orbit coupling, however, such $U(1)$ symmetry may disappear generally. Here, we stress that the AFTI in our analysis is more generic in the sense that our scenario does not require spin $U(1)$ symmetry. AFM systems respecting mirror symmetry with strong spin-orbit coupling are candidates for the AFTI proposed in this chapter.

2.3.2 Ferromagnetic topological half-metal

We now move on to an intriguing topological half-metallic state. Around quarter filling in the Kondo lattice system, it has been known that a half-metallic FM phase dubbed a spin-selective Kondo insulator [113–117] appears, where a spin-selective gap opens, namely, one spin sector is metallic while the other is insulating. This has been demonstrated for spin-conserving systems and has been extended later to a topological version referred to as a spin-selective topological insulator (SSTI) [88], where the insulating sector has topologically nontrivial properties. A crucial problem in the previous proposals is that all the results on the SSTI rely on spin $U(1)$ symmetry, which will disappear in the presence of spin-orbit coupling in general. Thus, one might naively think that the SSTI cannot appear in reality. To overcome this difficulty, we here demonstrate that by using a mirror symmetry, such a topological half-metallic state can indeed exist in the 2D FM phase.

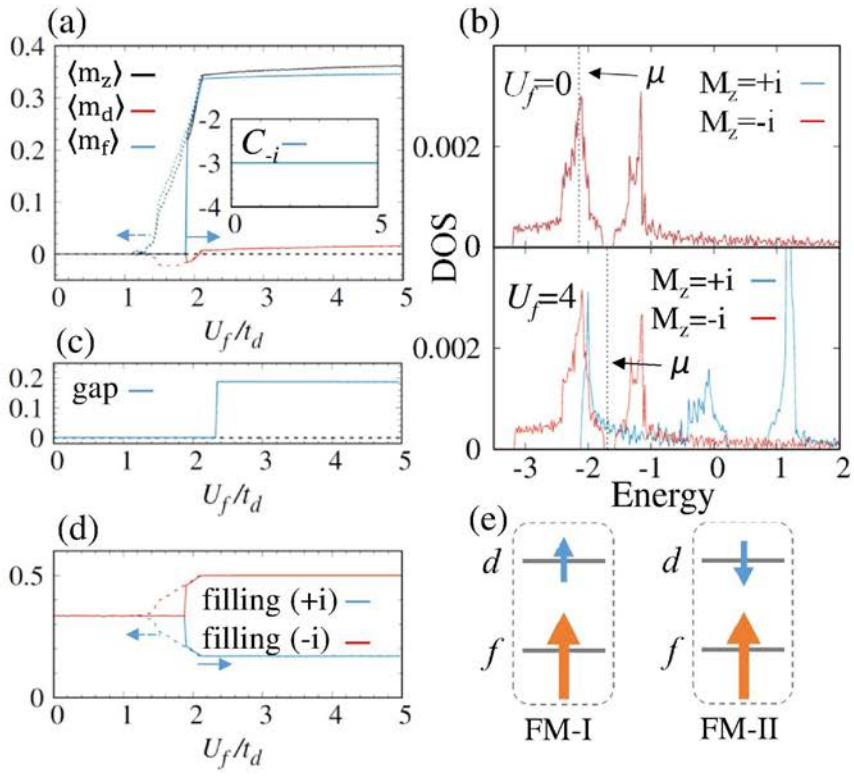

Fig. 2.5: Magnetic and topological properties around quarter filling for $(U_d, U_f) = (0, 4)$ and filling of 0.335: (a) magnetization of f- (d-) electrons, where the Chern number for the gapped sector is plotted in the inset. (b) DOS at $U_f = 0$ and $U_f = 4$, (c) gap of insulating sector, (d) electron filling for each mirror sector, (e) spin configurations. In (a), the red (blue) line represents d- (f-) electron magnetization and the black line the total magnetization. For all U_f, the system has the same Chern number $C_{-i} = -3$ in the mirror sector $M_z = -i$. In (b), we show the DOS for the sector of $M_z = +i$ ($M_z = -i$) by the blue (red) line, where the chemical potential μ is indicated by the dashed black line. In (c), the blue line is the gap of the mirror sector $M_z = -i$. In the region of $U_f > 2.3$, the sector $M_z = -i$ is an insulator. We have a metallic state at $U_f = 0$, while at $U_f = 4$, we have the SSTI, where the sector $M_z = +i$ ($M_z = -i$) is a metal (an insulator). Reprinted figure with premission from [245] Copyright 2018 by the Journal of the Physical Society of Japan.

In Figs. 2.5 and 2.6(a), we show the results obtained around quarter filling. At a filling

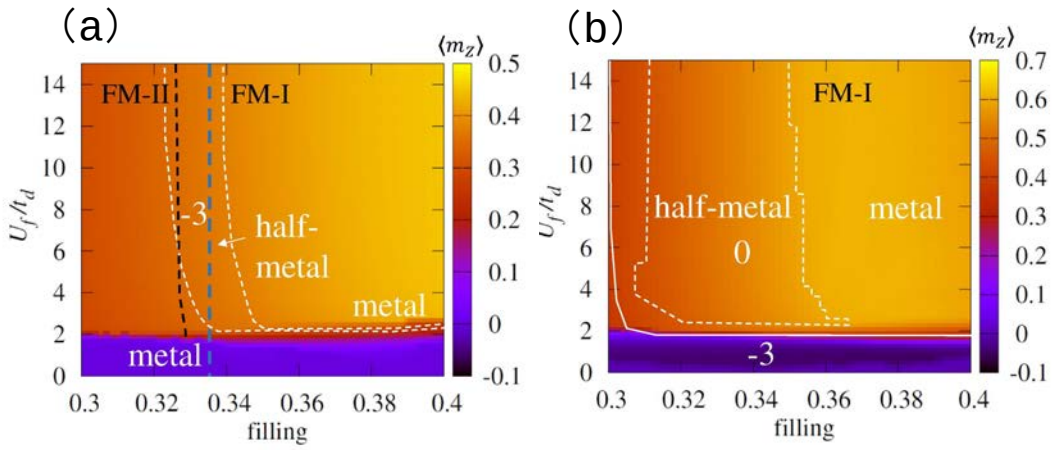

Fig. 2.6: Phase diagram of mirror-selective topological insulator around quarter filling: (a) $U_d = 0$, (b) $U_d = 2$. The white (dashed) line denotes the topological (insulator-metal) phase transition line and the black dashed line separates two FM phases, i.e., FM-I and FM-II. In the half-metallic region, the sector $M_z = -i$ has a finite gap and the sector $M_z = +i$ is metallic. The white numbers are mirror Chern numbers of the sector $M_z = -i$ in the whole region. The blue dashed line represents the filling of 0.335. The color plot shows the strength of the magnetization. Reprinted figure with premission from [245] Copyright 2018 by the Journal of the Physical Society of Japan.

of 0.335 and $U_d = 0$, a FM phase emerges, as seen in Fig. 2.5(a), where the magnetization has a hysteresis loop. From the density of states (DOS) shown in Fig. 2.5(b), we find that the system is metallic at $U_f = 0$, whereas the system is half-metallic at $U_f = 4$ with the $M_z = +i$ sector being metallic while the $M_z = -i$ sector is insulating, as seen in Fig. 2.5(c). This mirror-selective gap gives rise to the nontrivial topological number $C_{-i} = -3$ in Fig. 2.5(a), resulting in a mirror-selective topological insulator where the filling of the insulating sector is always half, as seen in Fig. 2.5(d). This spin configuration in Fig. 2.5(e) is of the FM-I type.

All these results are put together in the phase diagram of Fig. 2.6(a), shown as functions of the strength of the interaction U_f and the filling in the system. There are two FM phases having different types of spin configuration in Fig. 2.5(e) and the system has competition between two magnetic orders. We also study the case including the finite interaction U_d, as shown in Fig. 2.6(b). At $U_d = 2$, there is no topological phase, in contrast to the above-mentioned case of $U_d = 0$, which shows a nontrivial topological phase in some parameter region. In both cases, the direct gap is open even in the metallic phase and the band structure has a non-trivial topology, but in the ordered phase, the situation is different. Whereas the half-metallic FM phase is stabilized by the finite U_d, the finite U_d deforms the band structure into a topologically trivial in this mean-field calculation. The topological properties have a strong dependence on the band structure and spin configuration under the ferromagnetic ordered states. Summarizing, we find the mirror-selective topological insulator in a half-metallic FM phase, which can emerge for spin nonconserving systems, in contrast to the previous proposals.

2.3.3 Electron correlation effect: beyond mean-field description

So far, we have discussed the nontrivial topological states in the AFM phase and the half-metallic FM phase in the HF approximation. One may ask what will happen if electron correlations are taken into account beyond the HF treatment. Here, we argue that the

topological properties obtained from the mean-field Hamiltonian can persist even if we consider electron correlations by, for example, dynamical mean-field theory, provided the Mott transition is absent according to Refs. [74, 77, 246–248]. Recall that the Chern number of each mirror sector is given in terms of the Green's function as

$$C_\sigma = \int \frac{d\omega d^2k}{24\pi^2} \mathrm{Tr}[\epsilon^{\mu\nu\rho} G_\sigma \partial_\mu G_\sigma^{-1} G_\sigma \partial_\nu G_\sigma^{-1} G_\sigma \partial_\rho G_\sigma^{-1}], \tag{2.9}$$

where $\epsilon_{\mu\nu\rho}$ is a totally antisymmetric Levi-Civita tensor, and $(\partial_0, \partial_1, \partial_2) = (\partial_\omega, \partial_{k_x}, \partial_{k_y})$, $k = (\omega, \boldsymbol{k})$. Summation is assumed over repeated indices $\mu, \nu, \rho = 0, 1, 2$. σ specifies the mirror parity and G_σ is the full single-particle Green's function, which is related to the free Green's function $G_{\sigma 0}$ via $G_\sigma^{-1}(i\omega, \boldsymbol{k}) = G_{\sigma 0}^{-1}(i\omega, \boldsymbol{k}) - \Sigma_\sigma(i\omega, \boldsymbol{k})$, where $\Sigma_\sigma(i\omega, \boldsymbol{k})$ is the self-energy. In the present treatment, G_σ is a 4×4 (2×2) matrix in the AFM (half-metallic FM) case. According to Refs.[77, 248], the Chern number is determined by the topological Hamiltonian $h_\sigma^{\mathrm{eff}}(\boldsymbol{k}) = -G_\sigma^{-1}(0, \boldsymbol{k}) = -G_{\sigma 0}^{-1}(0, \boldsymbol{k}) + \Sigma_\sigma(0, \boldsymbol{k})$. This is because the Chern number does not change under the smooth deformation as

$$G_\sigma(i\omega, \boldsymbol{k}, \lambda) = (1 - \lambda) G_\sigma(i\omega, \boldsymbol{k}) + \lambda [i\omega + G_\sigma^{-1}(0, \boldsymbol{k})]^{-1}, \tag{2.10}$$

where $\lambda \in [0, 1]$, provided $\det G_\sigma \neq 0$ and $\det G_\sigma^{-1} \neq 0$ are satisfied. The cases of $\det G_\sigma = 0$ and $\det G_\sigma^{-1} = 0$ respectively correspond to the gap closing or the emergence of Mott insulators with $\mathrm{Im}[\Sigma(0, \boldsymbol{k})] \to -\infty$. Therefore, provided the Mott transition does not occur, the electron correlation effect on the AFM (half-metallic FM) phase can be treated with the renormalized band insulator, and thus the HF results may not be changed qualitatively, although the phase diagram should be modified quantitatively.

2.4 Summary

In this chapter, we have explored two topological states in the AFM/FM phases by taking account of the mirror symmetry in heavy-fermion systems. Concretely, in reference to topological crystalline insulators, we have proposed 2D topological crystalline insulating states in magnetically ordered phases for interacting systems. In particular, we have shown that in the AFM phase at half filling there is a topological state characterized by a mirror Chern number. In the case of a SmB_6 film, an AFM topological semimetallic phase is expected. We have also shown that in the half-metallic FM phase around quarter filling, the spin-selective topological insulating state characterized by a Chern number is realized.

In contrast to the previous studies, which assumed spin $U(1)$ symmetry to obtain such topological properties in the magnetic phases, our proposal is that these phases can be realized even in the absence of spin $U(1)$ symmetry by taking into account crystalline symmetry in magnetic phases. Generally, spin $U(1)$ symmetry is not preserved in the presence of spin-orbit coupling; thus, the present scenario without respecting spin $U(1)$ symmetry will provide a feasible platform to realize magnetic topological insulators for 2D systems.

All numerical calculations have been done in the HF approximation. We also have discussed the correlation effects qualitatively and shown that the topological properties of these states may not change in the presence of correlation effects. Nevertheless, more elaborate calculations should be carried out to confirm this conclusion. In addition, a 3D version of the mirror-selective topological insulator has been discussed [249]. It might

be interesting to study how our mirror-selective topological insulator extends to three dimensions by increasing the thickness of the layers. Moreover, resent experiments have shown a metallic AFM phase with pressurized SmB_6[250–254]. From the first-principle calculation[255], it has been pointed out that this metallic AFM phase would serve as a better candidate for a AFTI with Z_2 number and A-type AF configuration is proposed for its ground state. Motivated by these studies, we have also discussed the possibility of the realization of the mirror symmetric AFTI phase[256].

2.5 Appendix for this chapter: Derivation of some models

2.5.1 Three-dimensional effective model of SmB_6

The 3D effective model Hamiltonian [237, 238, 244] reads

$$H_{\boldsymbol{k}} = \sum_{\boldsymbol{k}} \begin{pmatrix} \boldsymbol{d}_{\boldsymbol{k}}^\dagger & \boldsymbol{f}_{\boldsymbol{k}}^\dagger \end{pmatrix} \begin{pmatrix} \epsilon_{\boldsymbol{k}}^d & V_{\boldsymbol{k}} \\ V_{\boldsymbol{k}}^\dagger & \epsilon_{\boldsymbol{k}}^f \end{pmatrix} \begin{pmatrix} \boldsymbol{d}_{\boldsymbol{k}} \\ \boldsymbol{f}_{\boldsymbol{k}} \end{pmatrix} \tag{2.11a}$$

with

$$\begin{aligned} \epsilon_{\boldsymbol{k}}^d &= [-2t_d(\cos k_x + \cos k_y + \cos k_z) \\ &\quad -4t_d'(\cos k_x \cos k_y + \cos k_y \cos k_z + \cos k_z \cos k_x)]\sigma_0, \qquad (2.11b) \\ \epsilon_{\boldsymbol{k}}^f &= [\epsilon_f - 2t_f(\cos k_x + \cos k_y + \cos k_z) \\ &\quad -4t_f'(\cos k_x \cos k_y + \cos k_y \cos k_z + \cos k_z \cos k_x)]\sigma_0, \qquad (2.11c) \\ V_{\boldsymbol{k}} &= -2[\sigma_x \sin k_x(V_1 + V_2(\cos k_y + \cos k_z)) \\ &\quad +\sigma_y \sin k_y(V_1 + V_2(\cos k_z + \cos k_x)) + \sigma_z \sin k_z(V_1 + V_2(\cos k_x + \cos k_y))], \\ &\qquad (2.11d) \end{aligned}$$

where $\epsilon_{\boldsymbol{k}}^d(\epsilon_{\boldsymbol{k}}^f)$ is the dispersion of d-(f-) electrons, $V_{\boldsymbol{k}}$ is the Fourier component of the nonlocal d-f hybridization, and $\boldsymbol{k}$ is the wave number. The annihilation operators are defined as $\boldsymbol{d}_{\boldsymbol{k}} = \begin{pmatrix} d_{\boldsymbol{k}\uparrow} & d_{\boldsymbol{k}\downarrow} \end{pmatrix}^T$, $\boldsymbol{f}_{\boldsymbol{k}} = \begin{pmatrix} f_{\boldsymbol{k}\uparrow} & f_{\boldsymbol{k}\downarrow} \end{pmatrix}^T$. The basis function for this model is $(d_\uparrow, d_\downarrow, f_\uparrow, f_\downarrow)^T$, where $\sigma_i (i = 0, x, y, z)$ are the Pauli matrices for spins. The concrete values of the parameters we employ are $t_d = 1$ (energy unit), $t_d' = -0.5, t_f = -t_d/5, t_f' = -t_d'/5$. Note that this model has three band inversions at X points [239–242] as shown in Fig. 4.4. Our 2D effective model is introduced to properly take into account this inversion property.

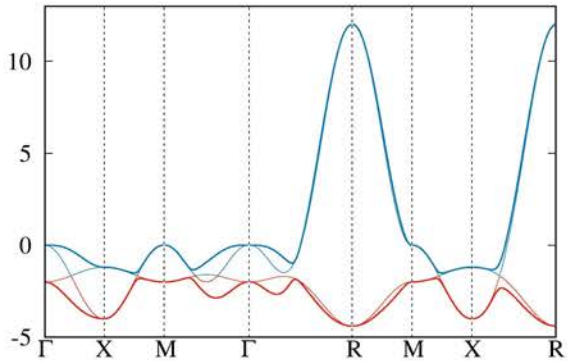

Fig. 2.7: Energy spectrum of the model for 3D SmB_6. The thick lines are the band structures of d- and f-electrons, $(V_1, V_2) = (0.1, -0.4)$. The thin lines show the bare energies of d- and f-bands for the same parameters but with vanishing hybridization $(V_1, V_2) = (0, 0)$. The band inversion at the X point is realized. Reprinted figure with premission from [245] Copyright 2018 by the Journal of the Physical Society of Japan.

2.5.2 Effective spin model: Strong correlation limit

Here, we determine the magnetization axis by using second-order perturbation theory to clarify whether the magnetization is mirror-symmetric or not. For simplicity, we use the model with $V_2 = 0$, $t'_d = 0$, $t'_f = 0$ at half filling. Starting from the strong correlation limit $U_f \gg 1$, we use the normalized hybridization V_1/U_f as a perturbation parameter. We use the following relations between the spins S_i^α ($\alpha = d, f$ and $i = x, y, z$) of d-/f-electrons and the fermionic operators $d_{i\sigma}$ and $f_{j\sigma}$ with spin indices $\sigma = \uparrow, \downarrow$ and site indices i, j:

$$S^d_{xi} \cdot S^f_{xj} = \frac{1}{2} \sum_{\sigma=\uparrow,\downarrow} \left(d^\dagger_{i\sigma} d_{i\bar{\sigma}} f^\dagger_{j\sigma} f_{j\bar{\sigma}} + d^\dagger_{i\sigma} d_{i\bar{\sigma}} f^\dagger_{j\bar{\sigma}} f_{j\sigma} \right), \tag{2.12a}$$

$$S^d_{yi} \cdot S^f_{yj} = \frac{1}{2} \sum_{\sigma=\uparrow,\downarrow} \left(-d^\dagger_{i\sigma} d_{i\bar{\sigma}} f^\dagger_{j\sigma} f_{j\bar{\sigma}} + d^\dagger_{i\sigma} d_{i\bar{\sigma}} f^\dagger_{j\bar{\sigma}} f_{j\sigma} \right), \tag{2.12b}$$

$$S^d_{zi} \cdot S^f_{zj} = \frac{1}{2} \sum_{\sigma=\uparrow,\downarrow} \left(d^\dagger_{i\sigma} d_{i\sigma} f^\dagger_{j\sigma} f_{j\sigma} - d^\dagger_{i\sigma} d_{i\sigma} f^\dagger_{j\bar{\sigma}} f_{j\bar{\sigma}} \right), \tag{2.12c}$$

$$n^d_i \cdot n^f_j = \sum_{\sigma=\uparrow,\downarrow} \left(d^\dagger_{i\sigma} d_{i\sigma} f^\dagger_{j\sigma} f_{j\sigma} + d^\dagger_{i\sigma} d_{i\sigma} f^\dagger_{j\bar{\sigma}} f_{j\bar{\sigma}} \right). \tag{2.12d}$$

The hybridization term then results in the following exchange interaction via the second-order perturbation:

$$\begin{aligned} H' = & \sum_{i\in x} J^{ix}_{df} S^d_{xi} \cdot S^f_{xi-1} + J^{iy}_{df} S^d_{yi} \cdot S^f_{yi-1} + J^{iz}_{df} S^d_{zi} \cdot S^f_{zi-1} \\ & + \sum_{i\in x} J^{ix}_{df} S^d_{xi-1} \cdot S^f_{xi} + J^{iy}_{df} S^d_{yi-1} \cdot S^f_{yi} + J^{iz}_{df} S^d_{zi-1} \cdot S^f_{zi} \\ & + \sum_{j\in y} J^{jx}_{df} S^d_{xj} \cdot S^f_{xj-1} + J^{jy}_{df} S^d_{yj} \cdot S^f_{yj-1} + J^{jz}_{df} S^d_{zj} \cdot S^f_{zj-1} \\ & + \sum_{j\in y} J^{jx}_{df} S^d_{xj-1} \cdot S^f_{xj} + J^{jy}_{df} S^d_{yj-1} \cdot S^f_{yj} + J^{jz}_{df} S^d_{zj-1} \cdot S^f_{zj}, \end{aligned} \tag{2.13}$$

where $J_{df}^{i,\alpha}$ ($i = x, y$ and $\alpha = x, y, z$) are the coupling constants between d- and f-electrons. For the spin configuration along the x-axis, the coupling constants satisfy $J_{df}^{ix} = J_{df} > 0, J_{df}^{iy} = -J_{df} < 0$, and $J_{df}^{iz} = -J_{df} < 0$, while for the y-axis, they satisfy $J_{df}^{jx} = -J_{df} < 0, J_{df}^{jy} = J_{df} > 0, J_{df}^{jz} = -J_{df} < 0$ (see Table. A·1), and $J_{df} = 2V_1^2(\frac{1}{\epsilon_f} + \frac{1}{U_f - \epsilon_f}) > 0$, where ϵ_f is the chemical potential of f-electrons. From only this constraint, we cannot yet determine the spin configuration at the ground state. When $t_{dd} = t_{ff} = 0$, the spins can be polarized along the x- or y-direction without energy loss.

We then consider another perturbation expansion in t_f/U_f for $U_f \gg 1$. It induces the AFM interaction $J_{ff}\boldsymbol{S}_i^f \cdot \boldsymbol{S}_j^f (J_{ff} < 0)$, giving rise to frustration in these cases. As a result, the easy axis of the magnetization is the z-axis, preserving the mirror symmetry, and the ground state of this model prefers the configuration having the staggered AFM order in Fig. 2.8, where all other magnetic configurations are frustrated. Those for d-electrons and f-electrons align in the opposite directions at the same site.

Table 2.1: Exchange couplings obtained for the spin-half 2D periodic Anderson model with non-local d-f hybridization using second-order perturbation theory from the strong correlation limit. J_{df}^x, J_{df}^y, and J_{df}^z are coupling constants for the effective spin model, where superscripts x, y, and z specify the quantization axis for the spin. There are two spin configurations along the x- and y-axes. $+$ $(-)$ means an antiferromagnetic (AF) [ferromagnetic (F)] coupling.

	J_{df}^x	J_{df}^y	J_{df}^z
x-axis	$+$(AF)	$-$(F)	$-$(F)
y-axis	$-$(F)	$+$(AF)	$-$(AF)

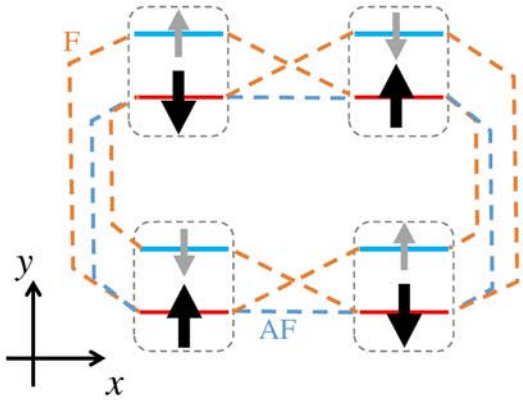

Fig. 2.8: Spin configuration in real space, where all the spins align along the z-axis. The blue (red) lines denote the d- (f-) level and the bold black/gray arrows denote spins. The dashed blue (orange) lines indicate the AF (F) coupling, where we consider the perturbation in V_1/U_f and t_f/U_f. There is no frustration and a configuration having a staggered AFM phase is realized, where f- and d-electrons align antiparallel at each site. Reprinted figure with premission from [245] Copyright 2018 by the Journal of the Physical Society of Japan.

We further consider the perturbation expansion in t_d/U_d for $U_d \gg 1$ because d-electrons have reasonably strong correlation. It turns out that this term induces the AFM interaction $J_{dd}\boldsymbol{S}_i^d \cdot \boldsymbol{S}_j^d (J_{dd} < 0)$ with no frustration in this order if the easy axis of magnetization is the z-axis. In this situation, the coupling constants are modified as $J_{df} = 2V_1^2(\frac{1}{U_d+\epsilon_f} + \frac{1}{U_f-\epsilon_f}) > 0$ but the sign is unchanged. We thus conclude that the easy axis of the magnetization is the z-axis and a staggered AFM phase, where f- and d-electrons align antiparallel at each site, is realized.

Chapter 3

Chiral-symmetry protected exceptional torus in correlated nodal-line semi-metals

3.1 Introduction to this chapter

In this chapter, we investigate emergent non-Hermitian properties in strongly correlated nodal-line semimetals(NLSMs) with chiral symmetry. As we have mentioned in Sec. 1.3, non-Hermitian topological semimetals in strongly correlated electron systems have attracted attention as a new type of correlation-induced topological states. Furthermore, the notion of non-Hermiticity has a potential to solve the problem of quantum oscillations in Kondo insulators, and further analysis is required. There have been many analyses of the emergence of effective non-Hermitian band structures in conventional equilibrium systems, especially in heavy-fermion systems. However, these analyses have been limited to the calculation of the spectral function. Thus, in spite of the intensive studies, it remains unclear what physical properties are affected by the non-Hermitian band structure. In particular, there are few studies elucidating effects of the non-Hermitian band structure on magnetic and/or electric responses.

Motivated by these situations, we investigate emergent non-Hermitian properties with chiral symmetry protected NLSMs, and discuss their impact on bulk quantities such as the magnetic susceptibility. The chiral-symmetric NLSMs provide a feasible platform to study non-Hermiticity and symmetry-protected topological degeneracy. Specifically, employing the dynamical mean-field theory[257–261] combined with the iterated perturbation theory[259–261] (DMFT+IPT), we elucidate the emergence of symmetry-protected exceptional torus (SPETs) for a Hubbard model of the diamond lattice. These SPETs induce a sharp peak of the local density of states at the Fermi energy only for one of the sublattices having weak correlation, which results in the local magnetic susceptibility of strong sublattice dependence. To our best knowledge, this is the first result exemplifying how the non-Hermitian degeneracies affect magnetic responses. We stress that the chiral symmetry is essential for the above behaviors. Recently, the emergence of SPETs with PT (product of parity and time-reversal) symmetry has been reported by analyzing a noninteracting non-Hermitian Hamiltonian[224]. In contrast to such a case, SPETs with chiral symmetry are fixed to the Fermi level, which induces the Fermi volumes (i.e., low energy excitations enclosed by SPETs) in the Brillouin zone [1].

[1] SPETs with CP (product of parity and particle-hole) symmetry are fixed to the Fermi level. However,

This chapter is organized as follows. In Sec. 3.2, we describe our setup and give a brief explanation of our approach. From Sec. 3.2.1 to Sec. 3.2.3, we derive DMFT formulation on the diamond lattice Hubbard model. In Sec. 3.3, we show the phenomenology of the chiral-symmetry protected non-Hermitian degeneracies. In Sec. 3.4, we show the DMFT results for the interaction driven exceptional torus. We study the emergence of exceptional torus at the Fermi level and its impact on bulk properties thorough the magnetic susceptibility. Sec. 3.5 is devoted to the summary of this chapter. Finally, in Sec. 3.6, we note for some formulas.

3.2 Dynamical mean-field theory on the diamond lattice Hubbard model

3.2.1 Hubbard model on the diamond lattice

We study the two-band Hubbard model with spatially modulated on-site Hubbard interactions on the diamond lattice (see Fig.3.1);

$$\hat{H} = \sum_{\langle i\alpha, j\alpha'\rangle\sigma} t_{ij}\hat{c}^{\dagger}_{i\alpha\sigma}\hat{c}_{j\alpha'\sigma} + \sum_{i\alpha} U_{\alpha}(\hat{n}_{i\alpha\uparrow} - \frac{1}{2})(\hat{n}_{i\alpha\downarrow} - \frac{1}{2}), \tag{3.1}$$

where $\hat{c}^{\dagger}_{i\alpha\sigma}(\hat{c}^{\dagger}_{i\alpha\sigma})$ creates (annihilates) a fermion at the i-th site of sublattice $\alpha(= A, B)$ with spin σ and $\hat{n}_{i\alpha\sigma} = \hat{c}^{\dagger}_{i\alpha\sigma}\hat{c}_{i\alpha\sigma}$. $t \in \mathbb{R}$ is a hopping parameter and $U_{\alpha} \in \mathbb{R}$ is an on-site interaction. The first term of the above Hamiltonian describes hopping of fermions between neighboring sites in the diamond-lattice whose primitive vectors are $\boldsymbol{a}_i$, $(i = 1,2,3)$: $\boldsymbol{a}_1 = \frac{a}{2}(0,1,1)$, $\boldsymbol{a}_2 = \frac{a}{2}(1,0,1)$, $\boldsymbol{a}_3 = \frac{a}{2}(1,1,0)$. The noninteracting term denotes the NLSM, which is protected by the chiral (sublattice) symmetry. Details are given in later this section and it is summarized in Fig. 3.2. We note that the many-body Hamiltonian Eq. (3.1) preserves the many-body chiral symmetry at half filling which is defined by Eqs. (3.12) and (3.13). We expect that our toy model can be realized for cold atoms because in such systems the spatially modulated interactions are fabricated by the optical Feshbach resonance [262, 263]. As pointed out in Ref. [224], PT symmetry may induce SPETs for the NLSMs with gain and loss, which indicates the presence of SPETs for corresponding correlated systems. We stress, however, that the crucial difference from the PT symmetric case is that for our system with many-body chiral symmetry, the low energy excitations induced by the SPETs appear strictly at the Fermi level, which enhances the magnetic susceptibility.

Topological characterization of nodal-line semimetal

Now we introduce the tight-binding model $h(\boldsymbol{k})$ of Eq. (3.1), as follows

$$h(\boldsymbol{k}) = \begin{pmatrix} 0 & D_{\boldsymbol{k}} \\ D^{*}_{\boldsymbol{k}} & 0 \end{pmatrix}, \; D_{\boldsymbol{k}} = t_0 + \sum_{j=1,2,3} t_j e^{i\boldsymbol{k}\cdot\boldsymbol{a}_j}. \tag{3.2}$$

Here, the Pauli matrices τ's act on the sublattice space and t_i with $i = 0,1,2,3$ denotes the nearest neighbor hopping indicated by silver (gold) bonds in Fig.3.1. The nodal-line

the system with CP symmetry is realized for superconductors.

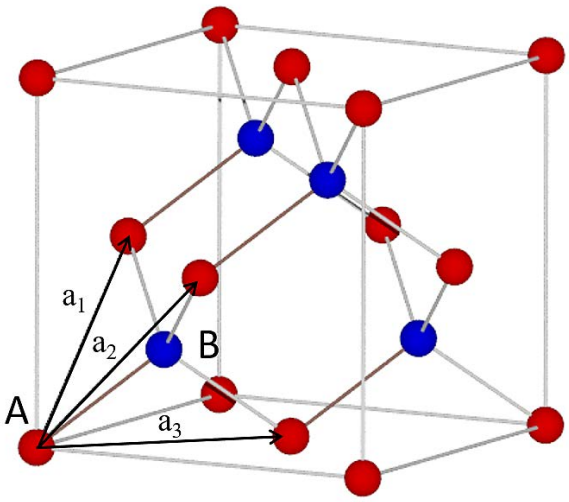

Fig. 3.1: Sketch of the diamond lattice. Blue (red) spheres denote the A- (B-) sublattice. $\boldsymbol{a}_i$ $(i = 1,2,3)$ denote primitive lattice vectors. Reprinted figure with premission from [264] Copyright 2019 by the American Physical Society.

structure of the noninteracting Hamiltonian can be understood by stacking of the one-dimensional topological insulators with chiral symmetry. The noninteracting Hamiltonian $h(\boldsymbol{k})$ has the chiral symmetry: $\{h(\boldsymbol{k}), \tau_3\} = 0$, where τ_3 is the chiral matrix which acts on the sublattice degrees of freedom in two sublattice system. To see the topological properties of the Dirac line node, we calculate the winding number along the blue line in Fig. 3.2(a). The definition of the winding number is:

$$\nu_{k_x,k_y} = \frac{1}{2\pi i}\int_{-2\pi}^{2\pi} dk_z \partial_{k_z} \ln D_{\boldsymbol{k}} = \frac{1}{2\pi}[\arg D_{\boldsymbol{k}}|_{k_z=2\pi} - \arg D_{\boldsymbol{k}}|_{k_z=-2\pi}]. \quad (3.3)$$

We note that the period in the k_z direction is 4π. The structure of the argument of $D_{\boldsymbol{k}}$ on $k_y = \pi$ plane is shown in Fig. 3.2(b) and the winding number is shown in Fig. 3.2(c). The change of winding number signals the bulk gapless structure and the Dirac line node structure appears in the three-dimensional BZ.

3.2.2 DMFT+IPT method for many-body chiral symmetric system

In the following, we demonstrate the correlation-induced SPETs by spatially modulated interactions in three dimensional systems. We employ the DMFT+IPT method to analyze correlation effects and clarify how SPETs affect low-energy properties. In order to treat inhomogenity with the DMFT framework, we employ the sublattice method[261]. In the DMFT framework, the lattice model is mapped to an effective impurity model described by

$$Z^{\alpha}_{\rm eff} = \int \mathcal{D}\bar{c}_{0\alpha\sigma}\mathcal{D}c_{0\alpha\sigma} e^{-S^{\alpha}_{\rm eff}}, \quad (3.4)$$

$$S^{\alpha}_{\rm eff} = -\int_0^{\beta} d\tau \int_0^{\beta} d\tau' \sum_{\sigma} \bar{c}_{0\alpha\sigma}(\tau)\mathcal{G}^{-1}_{\alpha\sigma}(\tau-\tau')c_{0\alpha\sigma}(\tau') + U_{\alpha}\int_0^{\beta} d\tau (n_{0\alpha\uparrow}(\tau) - \frac{1}{2})(n_{0\alpha\downarrow}(\tau) - \frac{1}{2}), \quad (3.5)$$

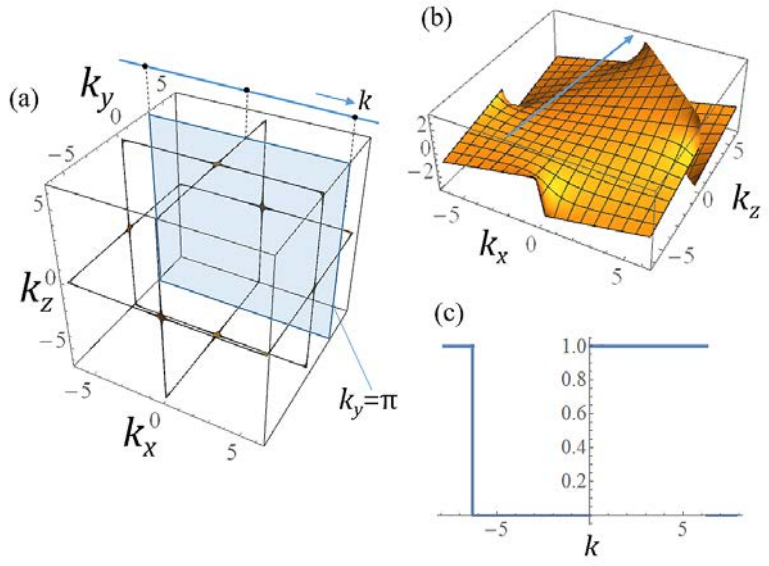

Fig. 3.2: The topological properties of noninteracting Hamiltonian are shown here. (a): The Fermi surface (the black line) at the noninteracting case in the three-dimensional BZ. (b): The argument of the off-diagonal element $D_{\boldsymbol{k}}$ on $k_y = \pi$ plane and the blue arrow means the path of integral. (c): The winding number $\nu_{k_x,k_y=\pi}$ on the blue arrow of (a). In panel (b), we plotted the Arg $D_{\boldsymbol{k}}$, where Arg means the principal value of the argument within the interval $(-\pi, \pi]$. Reprinted figure with premission from [264] Copyright 2019 by the American Physical Society.

where $\mathcal{G}_{\alpha\sigma}(\tau)$ is the noninteracting Green's function of the effective impurity model for the sublattice α, imaginary time τ, inverse temperature β and $\bar{c}_{0\alpha\sigma}$ is a Grassmannian variable corresponding to the creation operator. $\mathcal{G}_{\alpha\sigma}(\tau)$ is obtained by solving the following self-consistent equation:

$$\mathcal{G}^{-1}_{\alpha\sigma}(\omega) = \left[\frac{1}{N}\sum_{\boldsymbol{k}}\frac{1}{(\omega+i\delta+\mu)\mathbb{1}-h(\boldsymbol{k})-\Sigma^R_\sigma(\omega)}\right]^{-1}_{\alpha\alpha} - \Sigma^R_{\alpha\sigma}(\omega), \quad (3.6)$$

where the Fourier representation of noninteracting Hamiltonian $h(\boldsymbol{k})$ is given by a 2×2 matrix which is constructed from two sublattices and $\Sigma^R_\sigma(\omega) := \mathrm{diag}(\Sigma^R_{A\sigma}(\omega), \Sigma^R_{B\sigma}(\omega))$ denotes the self-energy of the retarded Green's function describing electrons on sublattice α.

In order to solve the self-consistent equation in Eq. (3.6), we employ the IPT method which is particularly efficient for a particle-hole symmetric system[261]. The second-order self-energy is calculated as $\Sigma^{(2)}_{\alpha\sigma}(\tau) = -U^2_\alpha \mathcal{G}_{\alpha\sigma}(\tau)\mathcal{G}_{\alpha-\sigma}(-\tau)\mathcal{G}_{\alpha-\sigma}(-\tau)$. Here, we consider the spin symmetric case $\mathcal{G}_{\alpha\downarrow} = \mathcal{G}_{\alpha\uparrow}$. Thus, the retarded self-energy is written as

$$\Sigma^{R(2)}_\alpha(\omega) = U^2\int_{-\infty}^{\infty}dx\int_{-\infty}^{\infty}dy\int_{-\infty}^{\infty}dz\rho^0_\alpha(x)\rho^0_\alpha(y)\rho^0_\alpha(z) \times\frac{f(-x)f(-y)f(z)+f(x)f(y)f(-z)}{\omega-x-y+z+i\delta}, \quad (3.7)$$

where $\rho^0_\alpha(\omega) = -\frac{1}{\pi}\mathrm{Im}\left[\mathrm{tr}\mathcal{G}_{\alpha\sigma}(\omega+i\delta)\right]$ is the density of state (DOS) and $\delta = 0+$. By using the IPT solver we can provide real-frequency self-energies and Green's function without a numerical analytic-continuation.

3.2.3 Random phase approximation for the magneic susceptibility

From obtained Green's function with DMFT+IPT, we compute the magnetic susceptibility as follows. Based on the random-phase approximation (RPA), we obtain the site-resolved spin susceptibility $\chi^s_A := (\chi^{\mathrm{RPA}}_{AA} + \chi^{\mathrm{RPA}}_{AB})/2$, $\chi^s_B := (\chi^{\mathrm{RPA}}_{BB} + \chi^{\mathrm{RPA}}_{BA})/2$ (the factor $1/2$ means the square of spin $1/2$ times spin degrees of freedom 2) with $\boldsymbol{\chi}^{\mathrm{RPA}}(\boldsymbol{q}, i\epsilon_m) := (\mathbf{1} - \boldsymbol{\chi}^0\boldsymbol{U})^{-1}\boldsymbol{\chi}^0$, where 2×2 matrices $\boldsymbol{\chi}^{\mathrm{RPA}}$ ($\boldsymbol{\chi}^0$) are the RPA susceptibility (susceptibility with bubble approximation). $\boldsymbol{U}$ denotes the interaction matrix, $\boldsymbol{U} := \mathrm{diag}(U_A, U_B)$. Matrix elements $\chi^0_{\alpha\beta}$ are defined as

$$\chi^0_{\alpha\beta}(\boldsymbol{q}, i\epsilon_m) = -\frac{T}{N}\sum_{\boldsymbol{k},n} G_{\alpha\beta}(\boldsymbol{q}+\boldsymbol{k}, i\omega_n + i\epsilon_m) G_{\beta\alpha}(\boldsymbol{k}, i\omega_n), \tag{3.8}$$

where $\epsilon_m = 2m\pi T$, $m \in \mathbb{Z}$ and $G_{\alpha\beta}(\boldsymbol{k}, i\omega_n)$ is lattice Green's function obtained from DMFT. Here, we have used the relation $G_\alpha(\boldsymbol{k}, i\omega_n) = \int_{-\infty}^{\infty} dx \frac{A_\alpha(\boldsymbol{k},x)}{i\omega_n - x}$. The magnetic susceptibility is given by the $\boldsymbol{q} = 0$ and $\epsilon_m = 0$ component of $\chi^s_\alpha(\boldsymbol{q}, i\epsilon_m)$, $\alpha = A, B$.

3.3 Overview of the symmetry protection of exceptional torus for chiral symmetry

In this section, we give a short review of chiral symmetry-protected non-Hermitian degeneracies. Let us analyze a generic system with chiral symmetry which has two bands. The non-Hermitian effective Hamiltonian, describing the single-particle excitations, is defined as $H_{\mathrm{eff}}(\omega, \boldsymbol{k}) := h(\boldsymbol{k}) + \Sigma^R(\omega + i\delta, \boldsymbol{k})$, where the Hermitian matrix $h(\boldsymbol{k})$ denotes the one-body part of the Hamiltonian, and $\Sigma^R(\omega + i\delta, \boldsymbol{k})$ denotes the self-energy with an infinitesimal positive constant δ. For a non-Hermitian 2×2 Hamiltonian, we can write an effective Hamiltonian of the form:

Effective non-Hermitian Hamiltonian

$$H_{\mathrm{eff}} = [b_0(\boldsymbol{k}) + id_0(\boldsymbol{k})]\tau_0 + [\boldsymbol{b}(\boldsymbol{k}) + i\boldsymbol{d}(\boldsymbol{k})]\cdot\boldsymbol{\tau}, \tag{3.9}$$

with two real d-vectors $\boldsymbol{b}(\boldsymbol{k}) := (b_1(\boldsymbol{k}), b_2(\boldsymbol{k}), b_3(\boldsymbol{k}))$ and $\boldsymbol{d}(\boldsymbol{k}) := (d_1(\boldsymbol{k}), d_2(\boldsymbol{k}), d_3(\boldsymbol{k}))$ and real numbers $b_0(\boldsymbol{k}), d_0(\boldsymbol{k})$, where τ's are Pauli matrices.

We immediately find the eigenenergies of the form

$$E_\pm(\boldsymbol{k}) = b_0(\boldsymbol{k}) + id_0(\boldsymbol{k}) \pm \sqrt{\boldsymbol{b}^2(\boldsymbol{k}) - \boldsymbol{d}^2(\boldsymbol{k}) + 2i\boldsymbol{b}(\boldsymbol{k})\cdot\boldsymbol{d}(\boldsymbol{k})}. \tag{3.10}$$

In order for the effective Hamiltonian to possess band touching points, two real d-vectors need to satisfy

Band touching conditions

$$\boldsymbol{b}^2(\boldsymbol{k}) = \boldsymbol{d}^2(\boldsymbol{k}),\ \boldsymbol{b}(\boldsymbol{k})\cdot\boldsymbol{d}(\boldsymbol{k}) = 0. \tag{3.11}$$

If the solution has non-zero vectors, then these equations describe exceptional points where the theory becomes defective, i.e., the Hamiltonian cannot be diagonalized and lacks a complete basis of eigenvectors.

To highlight the symmetry protection in our case, we first introduce the definition of the many-body chiral symmetry in Sec. 3.3.1. Second, we show the many-body chiral symmetry in terms of the Green's function in Sec. 3.3.2. Finally, we discuss the symmetry protection of the many-body chiral symmetry in the strongly correlated system in Sec. 3.3.3.

3.3.1 Definition of the many-body chiral symmetry

The definition of many-body chiral symmetry [74, 79] for the many-body Hamiltonian $\hat{H}$ is:

$$\hat{U}_\Gamma^\dagger \hat{H}^* \hat{U}_\Gamma = \hat{H}, \tag{3.12}$$

where $\hat{H}$ is many-body Hamiltonian and $\hat{U}_\Gamma$ is the chiral operator which is a unitary operator $\hat{U}_\Gamma^2 = 1$. $\hat{U}_\Gamma$ transforms a creation and annihilation operator $\hat{c}_{in}^\dagger$ and $\hat{c}_{in}$ (where i labels the sites of a lattice and n labels the internal degrees of freedom such as sublattice and spin, etc), as follows: $\hat{U}_\Gamma^\dagger \hat{c}_{in}^\dagger \hat{U}_\Gamma = \sum_m U_{\Gamma,nm} \hat{c}_{im}$ and $\hat{U}_\Gamma^\dagger \hat{c}_{in} \hat{U}_\Gamma = \sum_m \hat{c}_{im}^\dagger U_{\Gamma,mn}^\dagger$, where the unitary matrix $U_\Gamma^{(\dagger)}$ is the chiral matrix of the noninteracting Hamiltonian h_{ij} satisfying $U_\Gamma^\dagger h_{ij} U_\Gamma = -h_{ij}$ with $U_\Gamma^2 = \mathbb{1}$. Here $\mathbb{1}$ denotes the identity matrix. The explicit form of the chiral operator $\hat{U}_\Gamma$ is defined for systems composed of two sublattices, as follows:

$$\hat{U}_\Gamma = \prod_{js} (\hat{c}_{js\uparrow}^\dagger + \mathrm{sgn}(s)\hat{c}_{js\uparrow})(\hat{c}_{js\downarrow}^\dagger + \mathrm{sgn}(s)\hat{c}_{js\downarrow}), \tag{3.13}$$

where $\mathrm{sgn}(s)$ takes 1 and -1 for $s = A$ and $s = B$, respectively. From the above chiral transformation, it is straightforward to see that:

$$\hat{U}_\Gamma^\dagger \hat{c}_{is\sigma}^\dagger \hat{U}_\Gamma = \mathrm{sgn}(s)\hat{c}_{is\sigma},\ \hat{U}_\Gamma^\dagger \hat{c}_{is\sigma} \hat{U}_\Gamma = \mathrm{sgn}(s)\hat{c}_{is\sigma}^\dagger. \tag{3.14}$$

We note that the chiral matrix $U_\Gamma = \tau_3$, where the Pauli matrix τ_3 acts on the sublattice space.

3.3.2 Green's function formula of the many-body chiral symmetry

In terms of Green's function, we obtain the following relation:

Many-body chiral symmetry in terms of Green ' s function

$$G(\omega + i\delta) = -U_\Gamma^\dagger G^\dagger(-\omega + i\delta) U_\Gamma, \tag{3.15}$$

where U_Γ is the chiral matrix and $G(\omega + i\delta)$ is the single-particle Green's function.

To obtain above Eq. (3.15), we introduce the reterded and advanced Green's functions ($G^R(t)$, $G^A(t)$):

$$G_{ab}^R(t) = -i\theta(t)[\langle \hat{c}_a(t)\hat{c}_b^\dagger(0)\rangle + \langle \hat{c}_b^\dagger(0)\hat{c}_a(t)\rangle], \tag{3.16}$$
$$G_{ab}^A(t) = i\theta(-t)[\langle \hat{c}_a(t)\hat{c}_b^\dagger(0)\rangle + \langle \hat{c}_b^\dagger(0)\hat{c}_a(t)\rangle], \tag{3.17}$$

where a and b denote the set of indices, lattice site i and internal degrees of freedom n; $\hat{c}_a := \hat{c}_{in}$ and $\theta(t)$ is a step function. Now we assume that $t > 0$. Then we obtain the following relation:

$$\begin{aligned}
\langle \hat{c}_a(t)\hat{c}_b^\dagger(0)\rangle &= \mathrm{Tr}[e^{-\beta\hat{H}}e^{i\hat{H}t}\hat{c}_a(0)e^{-i\hat{H}t}\hat{c}_b^\dagger(0)] \\
&= \mathrm{Tr}[e^{-\beta\hat{H}}\hat{U}_\Gamma^\dagger e^{i\hat{H}^*t}\hat{U}_\Gamma\hat{c}_a(0)\hat{U}_\Gamma^\dagger e^{-i\hat{H}^*t}\hat{U}_\Gamma\hat{c}_b^\dagger(0)\hat{U}_\Gamma^\dagger\hat{U}_\Gamma], \\
&= U^\dagger_{\Gamma,aa'}U_{\Gamma,b'b}\mathrm{Tr}[e^{-\beta\hat{H}^*}e^{i\hat{H}^*t}\hat{c}^\dagger_{a'}(0)e^{-i\hat{H}^*t}\hat{c}_{b'}(0)], \\
&= U^\dagger_{\Gamma,aa'}U_{\Gamma,b'b}\mathrm{Tr}[\hat{c}^\dagger_{b'}(0)e^{-i\hat{H}t}\hat{c}_{a'}(0)e^{i\hat{H}t}e^{-\beta\hat{H}}], \\
&= U^\dagger_{\Gamma,aa'}U_{\Gamma,b'b}\langle\hat{c}^\dagger_{b'}(0)\hat{c}_{a'}(-t)\rangle. \qquad (3.18)
\end{aligned}$$

Here, we have used the following relations:

$$\begin{aligned}
e^{i\hat{H}t} &= \hat{U}_\Gamma^\dagger e^{i\hat{H}^*t}\hat{U}_\Gamma,\ e^{-\beta\hat{H}} = \hat{U}_\Gamma^\dagger e^{-\beta\hat{H}^*}\hat{U}_\Gamma, \qquad (3.19)\\
\hat{U}_\Gamma\hat{c}_a\hat{U}_\Gamma^\dagger &= U^\dagger_{\Gamma,aa'}\hat{c}^\dagger_{a'},\ \hat{U}_\Gamma\hat{c}_b^\dagger\hat{U}_\Gamma^\dagger = U^\dagger_{\Gamma,b'b}\hat{c}_{b'}, \qquad (3.20)\\
\langle M^*|\hat{A}|N^*\rangle &= \langle N|\hat{A}^T|M\rangle, \qquad (3.21)
\end{aligned}$$

where $|M\rangle$ and $|N\rangle$ denote general eigenstates of the many-body Hamiltonian. In a similar way, we have

$$\langle\hat{c}_b^\dagger(0)\hat{c}_a(t)\rangle = U^\dagger_{\Gamma,aa'}U_{\Gamma,b'b}\langle\hat{c}_{a'}(-t)\hat{c}^\dagger_{b'}(0)\rangle. \qquad (3.22)$$

As a result, we obtain $G^R(t) = -U_\Gamma^\dagger G^A(-t)U_\Gamma$ and the Fourier representation is:

$$G(\omega + i\delta) = -U_\Gamma^\dagger G(-\omega - i\delta)U_\Gamma, \qquad (3.23)$$

where $G(\omega + i\delta)$ is Green's function.

To go from Eq. (3.23) to Eq. (3.27), we have used the following relation:

$$G^\dagger_{ab}(\omega + i\delta) = G_{ab}(\omega - i\delta). \qquad (3.24)$$

This relation is understood by the Lehmann representation of the Green's function, as follows:

$$G_{ab}(z) = \sum_{NM} e^{\beta(\Omega - E_N)}\frac{e^{\beta(E_N-E_M)}+1}{z + E_N - E_M}\langle N|\hat{c}_a|M\rangle\langle M|\hat{c}_b^\dagger|N\rangle, \qquad (3.25)$$

where $z \in \mathbb{C}$, $e^{\beta\Omega} = \sum_N e^{-\beta E_N}$, and $E_N(\in \mathbb{R})$ is the energy for the many-body Hamiltonian. So the Hermitian conjugate of the Green's function is obtained:

$$\begin{aligned}
G^\dagger_{ab}(z) &= \sum_{NM} e^{\beta(\Omega - E_N)}\frac{e^{\beta(E_N-E_M)}+1}{(z + E_N - E_M)^*}\langle N|\hat{c}_b|M\rangle^*\langle M|\hat{c}_a^\dagger|N\rangle^*, \\
&= \sum_{NM} e^{\beta(\Omega - E_N)}\frac{e^{\beta(E_N-E_M)}+1}{z^* + E_N - E_M}\langle N|\hat{c}_a|M\rangle\langle M|\hat{c}_b^\dagger|N\rangle, \\
&= G_{ab}(z), \qquad (3.26)
\end{aligned}$$

where we have used Eq. (3.18) to go from the first line to the second line. We thus obtain Eq. (3.24).

Combining Eq. (3.24) and Eq. (3.23), we arrive at the many-body chiral symmetry in terms of Green's function:

$$G(\omega + i\delta) = -U_\Gamma^\dagger G^\dagger(\omega - i\delta)U_\Gamma, \qquad (3.27)$$

as shown in Eq. (3.15).

3.3.3 Effective non-Hermitian Hamiltonian representation of the many-body chiral symmetry

The effective Hamiltonian $H_{\text{eff}}(\omega, \boldsymbol{k})$ is defined by the single-particle Green's function: $G^{-1}(\omega + i\delta) = \omega \mathbb{1} - h_{\boldsymbol{k}} - \Sigma(\omega + i\delta, \boldsymbol{k}) = \omega \mathbb{1} - H_{\text{eff}}(\omega, \boldsymbol{k})$. In terms of $H_{\text{eff}}(\omega, \boldsymbol{k})$, we can rewrite the constraint of the many-body chiral symmetry of the form:

Many-body chiral symmetry in terms of effective non-Hermitian Hamiltonian

$$H_{\text{eff}}(\omega, \boldsymbol{k}) = -U_\Gamma^\dagger H_{\text{eff}}^\dagger(-\omega, \boldsymbol{k}) U_\Gamma. \tag{3.28}$$

In particular, at $\omega = 0$, this constraint is reduced to

$$H_{\text{eff}}(0, \boldsymbol{k}) = -U_\Gamma^\dagger H_{\text{eff}}^\dagger(0, \boldsymbol{k}) U_\Gamma, \tag{3.29}$$

which we refer to as extended chiral symmetry. In our model, the chiral matrix is written as $U_\Gamma := \tau_3$. From this constraint, each term of the effective Hamiltonian is divided into symmetric or anti-symmetric sectors as,

$$U_\Gamma^\dagger [b_i \tau_i]^\dagger U_\Gamma = \begin{cases} +b_i \tau_i, & (i = 0, 3) \\ -b_i \tau_i, & (i = 1, 2) \end{cases}, \tag{3.30}$$

$$U_\Gamma^\dagger [i d_i \tau_i]^\dagger U_\Gamma = \begin{cases} -i d_i \tau_i, & (i = 0, 3) \\ i d_i \tau_i, & (i = 1, 2) \end{cases}, \tag{3.31}$$

where four parameters $b_i (i = 1, 2)$ and $d_i (i = 0, 3)$ respect the chiral symmetry. We note $b_0 = b_3 = d_1 = d_2 = 0$.

Finally, considering the many-body chiral symmetry, the effective Hamiltonian $H_{\text{eff}}(0, \boldsymbol{k})$ is expanded by Pauli matrices τ's as follows.

Emergence of the exceptional ring/torus

$$H_{\text{eff}}(0, \boldsymbol{k}) = b_1(\boldsymbol{k})\tau_1 + b_2(\boldsymbol{k})\tau_2 + i\{d_0(\boldsymbol{k})\tau_0 + d_3(\boldsymbol{k})\tau_3\}. \tag{3.32}$$

Thus, the second condition (band touching condition) of Eq. (3.11) is satisfied automatically by the chiral symmetry. The manifold consisting of defective points is determined by the single constraint $\boldsymbol{b}^2(\boldsymbol{k}) = \boldsymbol{d}^2(\boldsymbol{k})$. The number of conditions for band degeneracy is reduced to one. As a result, a $(d-1)$-dimensional exceptional manifold emerges in the d-dimensional system when $d \geq 0$ [226]. Thus, we can obtain an exceptional ring and torus in two- and three- dimensional systems with chiral symmetry.

Note that the Fermi surface emerges in the region surrounded by exceptional manifold, called Femi volumes[225], which are open regions of vanishing real part of the energy gap and have the same dimension as the system itself.

3.4 DMFT results for the interaction driven exceptional torus

Having finished general arguments on chiral symmetric SPETs in the previous section, we now present the DMFT results in this section. We first show that SPETs with chiral

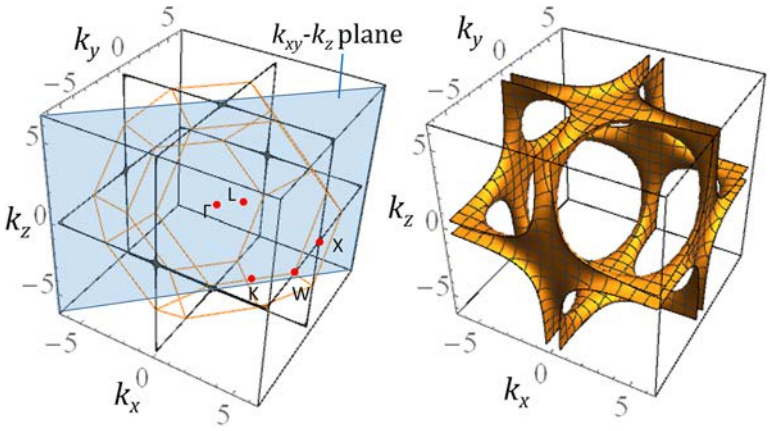

Fig. 3.3: Left panel: the Fermi surface (the black line) at the noninteracting case in the three-dimensional BZ. Right panel: the SPET (the orange surface) for $(U_A/t, U_B/t) = (8, 0)$ and $T/t = 0.8$. In the left figure, the orange line (blue plane) represents the three-dimensional BZ ($k_{xy} - k_z$ plane). Reprinted figure with premission from [264] Copyright 2019 by the American Physical Society.

symmetry emerges from DMFT+IPT calculation. Secondly, based on the RPA approximation, we numerically elucidate that low energy excitations accompanying the SPETs enhance the magnetic susceptibility.

The effective Hamiltonian $H_{\text{eff}}(0, \boldsymbol{k})$, which has the many-body chiral symmetry (Eq. 3.28), is expanded in terms of the Pauli matrices τ's as follows:

$$H_{\text{eff}}(0, \boldsymbol{k}) = id_0(\boldsymbol{k})\tau_0 + [\boldsymbol{b}(\boldsymbol{k}) + i\boldsymbol{d}(\boldsymbol{k})] \cdot \boldsymbol{\tau}, \tag{3.33}$$

$$\boldsymbol{b}(\boldsymbol{k}) = (b_1(\boldsymbol{k}), b_2(\boldsymbol{k}), 0), \tag{3.34}$$

$$\boldsymbol{d}(\boldsymbol{k}) = (0, 0, d_3(\boldsymbol{k})), \tag{3.35}$$

as we have shown in Eq. (3.32). The above vectors $\boldsymbol{b}$ and $\boldsymbol{d}$ are given by

$$b_1(\boldsymbol{k}) + ib_2(\boldsymbol{k}) = t_0 + \sum_{j=1,2,3} t_j e^{i\boldsymbol{k}\cdot\boldsymbol{a}_j}, \tag{3.36}$$

$$d_0(\boldsymbol{k})\tau_0 + d_3(\boldsymbol{k})\tau_3 = \text{Im}\Sigma^R(0 + i\delta, \boldsymbol{k}). \tag{3.37}$$

Intuitively, the origin of the non-Hermiticity is coming from the difference of the lifetime of the quasi-particles. Here, the Pauli matrices τ's act on the sublattice space and t_i with $i = 0, 1, 2, 3$ denotes the nearest neighbor hopping indicated by silver (gold) bonds in Fig.3.1. In this case, by using the above effective Hamiltonian, the Green's function is written as

$$G(\omega, \boldsymbol{k})^{-1} = (\omega + i\delta)\tau_0 - H_{\text{eff}}(\omega, \boldsymbol{k}). \tag{3.38}$$

3.4.1 Emergence of the interaction-driven SPET: Energy spectrum and spectral function

We investigate the diamond lattice with isotropic hopping $t_i = t, i = 0, 1, 2, 3$ for $U_B = 0$. First, we show the noninteracting Fermi surface. In the left panel of Fig.3.3, we can confirm that the diamond lattice shows nodal-line semi-metals. Introducing on the

interaction, the nodal line changes to the SPET (see right panel of Fig. 3.3). The SPET are given by the defective points of the effective non-Hermitian Hamiltonian. The real and imaginary parts of energy dispersion are shown in Fig. 3.4. On the cutting plane ($k_{xy} - k_z$), we confirm that the band touching region of the real part appears in Fig. 3.4(a) and it is enclosed by the defective points, i.e. the real part [Fig. 3.4(b)] and the imaginary part [Fig. 3.4(b)] of the energy dispersion has simultaneously the gapless structure on its points. We note that the change of the energy dispersion with/without interaction are shown in Fig. 3.4(c) and Fig. 3.4(d). At first glance, it looks like a modest change, but at point X, for example, we can see how the cross section of the gapless line originally becomes the cross section of the gapless volume. Thus we conclude that, inside of the SPET, the gap becomes pure imaginary and the low energy excitations appear as a Fermi volume inside of the SPET.

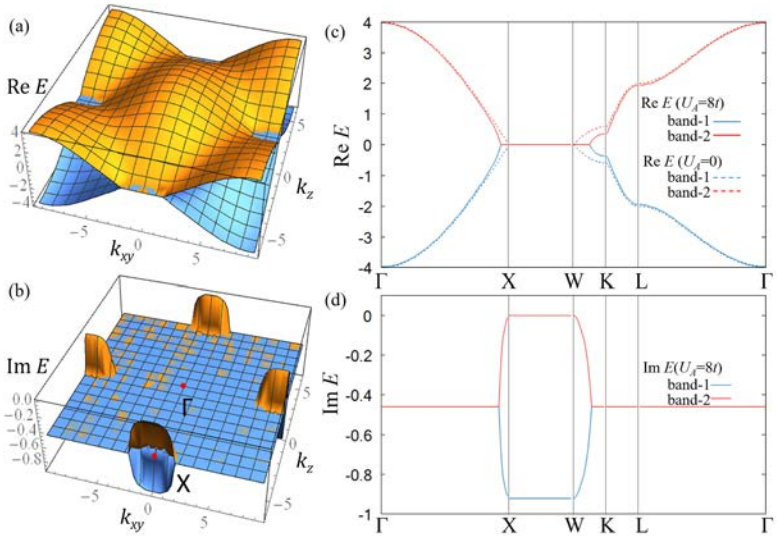

Fig. 3.4: The energy dispersion of non-Hermitian Hamiltonian $H_{\text{eff}}(0, \boldsymbol{k}) = h(\boldsymbol{k}) + \Sigma(0)$ with $(U_A/t, U_B/t, T/t) = (8, 0, 0.8)$. (a) and (b) [(c) and (d)] are the real and imaginary part of $H_{\text{eff}}(0, \boldsymbol{k})$ on the $k_{xy} - k_z$ plane [high symmetric line]. In panel (c), solid (dotted) lines denote the dispersion with $U_A = 8t$ ($U_A = 0$). Reprinted figure with premission from [264] Copyright 2019 by the American Physical Society.

The emergence of Fermi volume which is surrounded by SPET can be seen via the momentum-resolved spectral function $A(\boldsymbol{k}, \omega) = -\frac{1}{\pi}\text{Im}\left[\text{tr}G^R(\boldsymbol{k}, \omega)\right]$ [Fig. 3.5(a)]. Away from the Fermi level, these low energy excitations are smoothly connected with the renormalized bands see [Fig. 3.5(b)]. Here is a brief comment on Fig. 3.5(b). Although Fig. 3.5(b) seems to suggest that the region of high spectral weight between the X and W points has finite width in energy, we have confirmed that this width hardly depends on the interaction strength. This means that it is not originating from the interaction-driven SPET. The emergent Fermi volume, which is formed mainly by the contribution of the noninteracting B-sublattice, gives rise to a peak structure in the LDOS for the B-sublattice at zero energy as seen in Fig. 3.5(c). Note that these characteristic features come from largely different lifetimes for the two sublattices. The peak structure of LDOS is not limited to the diamond lattice but generally applies for two-sublattice chiral symmetric system. We discuss the relationship between the origin of the peak structure and the many-body chiral symmetric system in Sec. 3.4.2. The appearance of SPET and the peak

structure of LDOS originate from the sublattice-dependent Hubbard interaction.

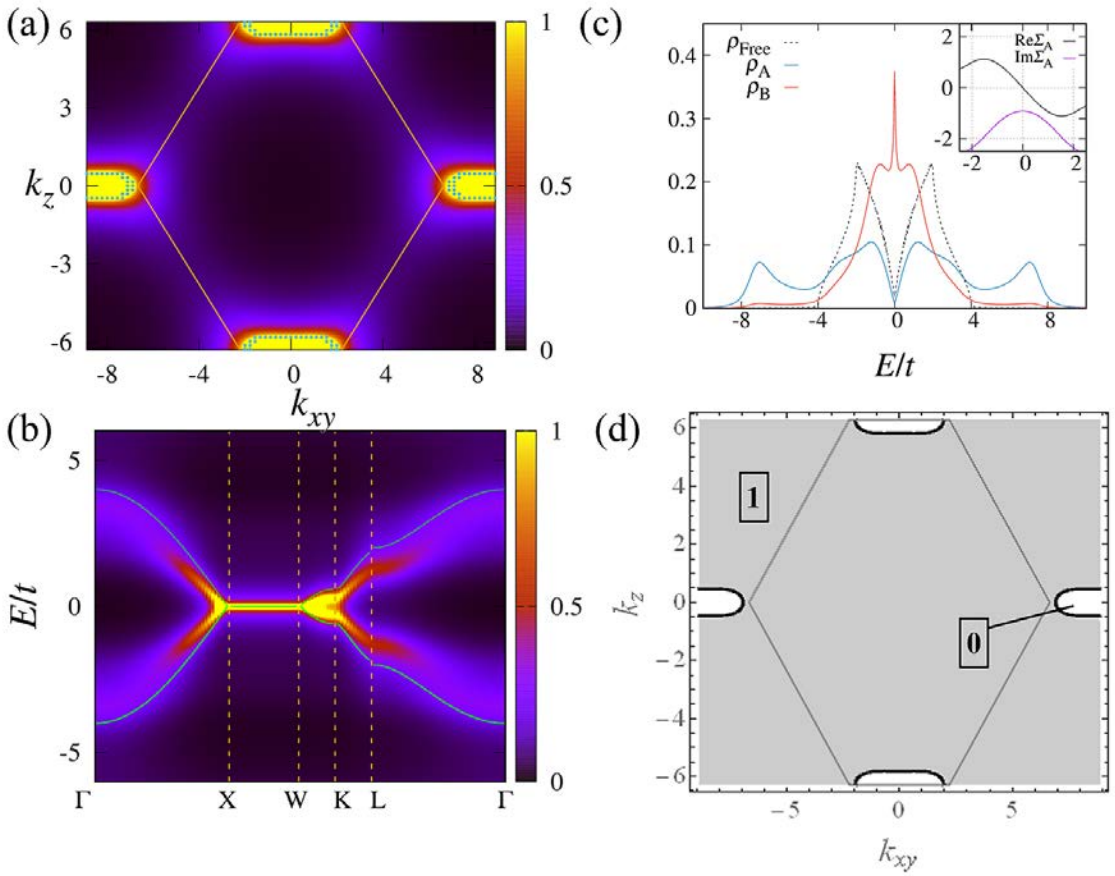

Fig. 3.5: (a) [(b)]: Momentum-resolved spectral weight $A(\boldsymbol{k},\omega=0)$ at k_{xy}-k_z plane [$A(\boldsymbol{k},\omega)$ at high symmetric points] of NLSM with $(U_A/t, U_B/t) = (8,0)$ at temperature $T/t = 0.8$. In panel (a), orange lines illustrate the BZ, the effective Hamiltonian becomes defective at the blue dots and the color plot indicates the strength of spectral weight. In panel (b), the blue line denotes the energy spectrum of free diamond lattice. (c): Density of states for each sublattice for $(U_A/t, U_B/t) = (8,0)$ at temperature $T/t = 0.8$. (d): Color map of the zero-th Chern number for $\mathrm{Im}\Sigma^R_A(\omega=0) = -0.92$ at k_{xy}-k_z plane. Here, the zero-th Chern number at each point is indicated by a number enclosed with a box and SPETs are represented with black line. Reprinted figure with premission from [264] Copyright 2019 by the American Physical Society.

Next, we check topological properties of the system. We show that a zero-th Chern number can be introduced for the occupation number of the following Hermitian Hamiltonian [210, 226]

$$\tilde{H}(\boldsymbol{k}) = -iH'(\boldsymbol{k})\Gamma, \tag{3.39}$$
$$H'(\boldsymbol{k}) = H_{\mathrm{eff}}(0,\boldsymbol{k}) - [\mathrm{tr}H_{\mathrm{eff}}(0,\boldsymbol{k})/N]\,\mathbb{1}, \tag{3.40}$$

with $N = \dim H_{\mathrm{eff}}(0,\boldsymbol{k})$. Exceptional points are consistent with the change of the Chern number in Fig.3.5(d). The radius of SPETs is related to the difference in the imaginary part of self-energy $r = [\mathrm{Im}\Sigma^R_B(\omega) - \mathrm{Im}\Sigma^R_A(\omega)]/2$ at $\omega = 0$ between A- and B- sublattices (see inset of Fig.3.5(c)). We show the size of SPET as functions of A-site interaction U_A/t and temperature T/t in Fig.4.3. We confirm that the radius of SPET is enhanced

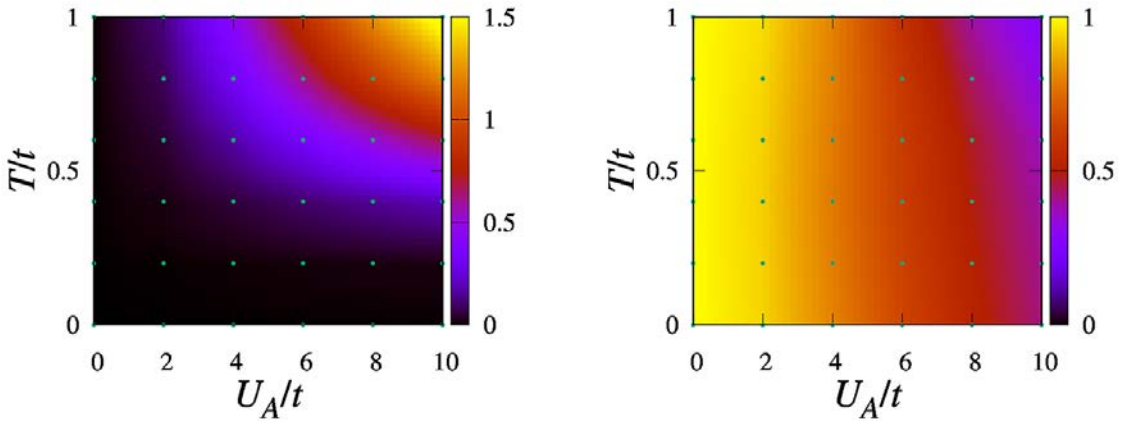

Fig. 3.6: Left panel: Color plot of the imaginary part of the self-energy $-\mathrm{Im}\Sigma_A^R(\omega=0)$ as functions of temperature T/t and interaction U_A/t. Right panel: Color plot of the renormalization factor $z_\alpha = [1-\partial \mathrm{Re}\Sigma_\alpha^R(\omega)/\partial\omega]^{-1}$ as functions of temperature T/t and interaction U_A/t. These data are obtained for the isotropic diamond lattice at $U_B/t=0$. We note that the imaginary part of the self-energy determines the radius of SPETs; the radius is $r=-\mathrm{Im}\Sigma_A^R(\omega=0)/2$. Reprinted figure with premission from [264] Copyright 2019 by the American Physical Society.

with increasing A-site interaction or temperature. However the renormalization factor of the A-site Green's function hardly depends on temperature in Fig.4.3.

SPET of anisotropic diamond lattice for $U_B = 0$

We proceed to investigate the anisotropic diamond lattice with $t_0/t_i \neq 1, i=1,2,3, t_i = t$. With increasing the parameter of hopping with $1 < t_0/t_i < 3$, the topological phase transition occurs and we obtain various shapes of SPETs in Appendix 3.6.1. We show the Fermi surface of nodal line semimetals with $t_0/t_i = 2$ in Fig.3.7 in the noninteracting case. Considering spatially modulated on-site Coulomb interactions, we obtain SPETs and momentum-resolved spectral weight in Fig.3.7 with $(U_A/t, U_B/t) = (12,0)$ at temperature $T/t=1$.

We stress that in contrast to the PT symmetric case[224], the band touching region inside of the SPETs emerges at $\omega=0$ (in this case it is called the Fermi volume) because of the chiral symmetry. This is understood by the prohibition of real coefficients of Pauli matrix τ_0 in an effective Hamiltonian although the PT symmetric system does not prohibit it. As discussed momentarily below, the Fermi volume inside of SPETs affects low-energy physical properties of the system.

3.4.2 LDOS structure in SPET

As shown in the previous subsection, the emergent Fermi volume, forming by noninteracting B-sublattice, gives rise to a peak structure in the LDOS. Beyond the above limited analysis with $U_B=0$, it is generally expected that the emergence of SPET and the Fermi volume are not limited to the U_B=0 case. Now we demonstrate what happens when the U_B is finite. We also use the isotropic diamond lattice for $U_B = U_A/2$. According to the DMFT calculation, the LDOS structure and difference in the imaginary part of self-energy

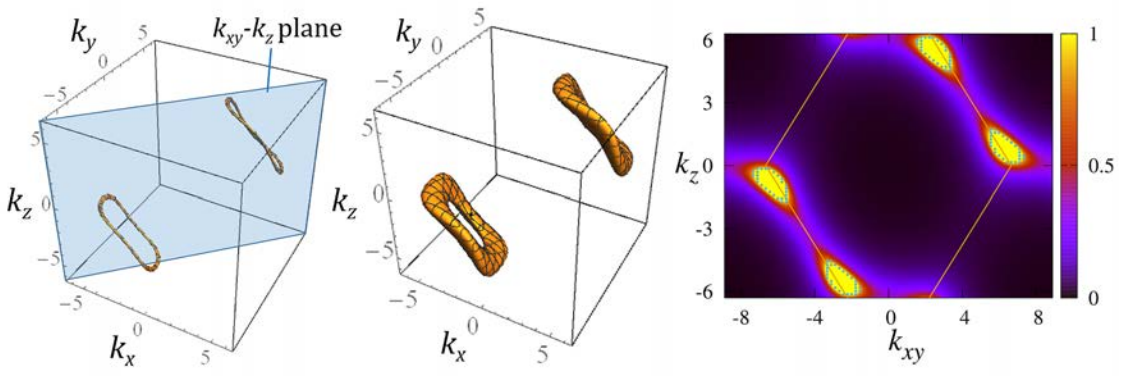

Fig. 3.7: The left (middle) panel: Noninteracting Fermi surface of NLSM (ET with $(U_A/t, U_B/t) = (12,0)$ at temperature $T/t = 1$) in the case of anisotropic diamond lattice $t_0/t_i = 2, (i = 1,2,3)$. The right panel: Momentum-resolved spectral weight $A(\boldsymbol{k}, \omega = 0)$ on k_z-k_{xy} plane with $(U_A/t, U_B/t) = (12,0)$ at temperature $T/t = 1$. The orange lines illustrate the BZ at k_{xy}-k_z plane and the effective Hamiltonian becomes defective at the blue dots in the right panel. Reprinted figure with premission from [264] Copyright 2019 by the American Physical Society.

$\mathrm{Im}\Sigma^R_B(\omega = 0) - \mathrm{Im}\Sigma^R_A(\omega = 0)$ are shown in Figs. 3.8(a) and 3.8(b). Compared to Fig. 3.5(c), the divergent peak structure does not appear, but the situation where the LDOS is higher in the weakly interacting B-sublattice than the strongly interacting A-sublattice. Moreover a similar dependence of interaction and temperature is observed in difference in the imaginary part of self-energy, which induces a non-Hermitian band structure.

In the following subsection, we discuss the origin of LDOS structure.

LDOS structure

$$\rho_A(\omega = 0) \quad < \quad \rho_B(\omega = 0), \tag{3.41}$$

where $\rho_\alpha = \sum_{\boldsymbol{k}\in BZ} A_\alpha(\boldsymbol{k}, \omega = 0)$, $\alpha = A, B$. Although the on-site Hubbard interactions U_A is larger than U_B, $\rho_B(\omega = 0)$ becomes larger than $\rho_A(\omega = 0)$ at finite temperature

To obtain the above Eq. (3.41), we discuss the sublattice dependent LDOS structure. Here, we consider the two-sublattice system with many-body chiral symmetry[226] and spin U(1) symmetry. The full Green's function is written in a 2×2 matrix which is constructed from two sublattices, as follows,

$$\begin{aligned} G(\boldsymbol{k}, \omega) &= [\omega \mathbb{1} - h(\boldsymbol{k}) - \Sigma^R(\boldsymbol{k}, \omega)]^{-1}, \\ &= \begin{pmatrix} \omega - \Sigma^R_A & -D_{\boldsymbol{k}} \\ -D^*_{\boldsymbol{k}} & \omega - \Sigma^R_B \end{pmatrix}^{-1}, \end{aligned} \tag{3.42}$$

where $h(\boldsymbol{k})$ and $\Sigma^R(\boldsymbol{k}, \omega)$ are Hamiltonian and self-energy,

$$h(\boldsymbol{k}) = \begin{pmatrix} 0 & D_{\boldsymbol{k}} \\ D^*_{\boldsymbol{k}} & 0 \end{pmatrix}, \Sigma^R(\boldsymbol{k}, \omega) = \begin{pmatrix} \Sigma^R_A & 0 \\ 0 & \Sigma^R_B \end{pmatrix}. \tag{3.43}$$

$D_{\boldsymbol{k}}$ is the Fourier component of tight-binding model as shown in Eq. (3.36) for example, and Σ^R_α are self-energy of each sublattice, $\alpha = A, B$. We obtain full Green's functions of

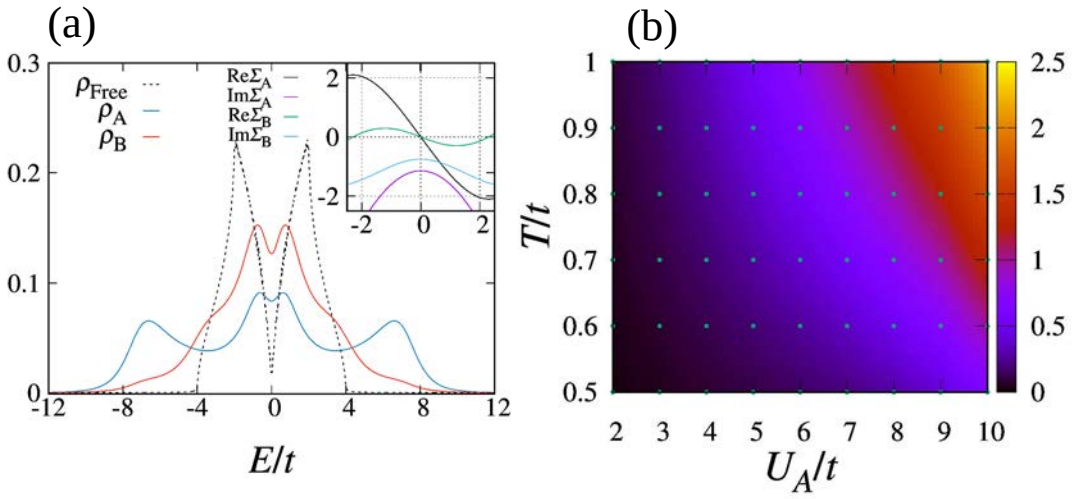

Fig. 3.8: Density of states and difference in the imaginary part of self-energy with $U_B = U_A/2$. (a) Density of states for each sublattice for $(U_A/t, U_B/t) = (9, 4.5)$ at temperature $T/t = 0.5$. The inset shows the self-energy $\Sigma_A^R(\omega)$ and $\Sigma_B^R(\omega)$ as a function of ω. (b) Color plot of the difference in the imaginary part of the self-energy $\mathrm{Im}\Sigma_B^R(\omega = 0) - \mathrm{Im}\Sigma_A^R(\omega = 0)$ as functions of temperature T/t and interaction U_A/t for the isotropic diamond lattice at $U_B = U_A/2$.The imaginary part of the self-energy determines the radius of SPETs. We note that the imaginary part of the self-energy determines the radius of SPETs; the radius is $r = [\mathrm{Im}\Sigma_B^R(\omega = 0) - \mathrm{Im}\Sigma_A^R(\omega = 0)]/2$. Reprinted figure with premission from [264] Copyright 2019 by the American Physical Society.

each subalttice,

$$G_{AA}(\boldsymbol{k}, \omega) = \frac{\omega - \Sigma_B^R}{(\omega - \Sigma_A^R)(\omega - \Sigma_B^R) - |D_{\boldsymbol{k}}|^2}, \tag{3.44}$$

$$G_{BB}(\boldsymbol{k}, \omega) = \frac{\omega - \Sigma_A^R}{(\omega - \Sigma_A^R)(\omega - \Sigma_B^R) - |D_{\boldsymbol{k}}|^2}. \tag{3.45}$$

To discuss the structure of LDOS, we consider the $\omega = 0$ component of spectral function for each sublattice,

$$\begin{aligned} A_A(\boldsymbol{k}, \omega = 0) &= -\frac{1}{\pi}\mathrm{Im}G_{AA}(\boldsymbol{k}, \omega = 0), \\ &= \frac{1}{\pi}\frac{-\mathrm{Im}\Sigma_B^R(0)}{\mathrm{Im}\Sigma_A^R(0)\mathrm{Im}\Sigma_B^R(0) + |D_{\boldsymbol{k}}|^2}, \end{aligned} \tag{3.46}$$

$$\begin{aligned} A_B(\boldsymbol{k}, \omega = 0) &= -\frac{1}{\pi}\mathrm{Im}G_{BB}(\boldsymbol{k}, \omega = 0), \\ &= \frac{1}{\pi}\frac{-\mathrm{Im}\Sigma_A^R(0)}{\mathrm{Im}\Sigma_A^R(0)\mathrm{Im}\Sigma_B^R(0) + |D_{\boldsymbol{k}}|^2}, \end{aligned} \tag{3.47}$$

where $A_\alpha(\boldsymbol{k}, \omega)$ is the spectral function of α sublattice, $\alpha = A, B$. Now we consider the imbalance of self-energy at the Fermi level such as

$$-\mathrm{Im}\Sigma_A^R(\omega = 0) > -\mathrm{Im}\Sigma_B^R(\omega = 0), \tag{3.48}$$

$$|\mathrm{Im}\Sigma_A^R(\omega = 0)| > |\mathrm{Im}\Sigma_B^R(\omega = 0)|, \tag{3.49}$$

where, due to the positivity of the spectral function, $\mathrm{Im}\Sigma_\alpha(\omega = 0)$ is always negative, $\alpha = A, B$. The relation between spectral functions of two sublattices is obtained as,

$$A_A(\boldsymbol{k}, \omega = 0) \quad < \quad A_B(\boldsymbol{k}, \omega = 0). \tag{3.50}$$

The above inequality is valid for all wave vectors in BZ. Finally, the LDOS is obtained from the summation of spectral function for all wave vectors and we show the relationship between LDOS of each sublattice, as follows,

$$\rho_A(\omega = 0) \quad < \quad \rho_B(\omega = 0), \tag{3.51}$$

where $\rho_\alpha = \sum_{\boldsymbol{k}\in BZ} A_\alpha(\boldsymbol{k}, \omega = 0)$, $\alpha = A, B$. The inequality means the imbalance of LDOS for each sublattice [see Figs. 3.5(c) and 3.8(a)]. In our case, the origin of self-energy is only on-site Coulomb interaction and the relation for the imbalance of self-energy Eq.(3.49) is the same as the imbalance of on-site Hubbard interactions $U_A > U_B$ at finite temperature. We show examples of the imbalance of self-energy in the inset of Figs. 3.5(c) and 3.8(a). As a result, in the many-body chiral symmetric system with spin U(1) symmetry, considering the spatially modulated on-site Hubbard interactions, the peak structure or the imbalance of LDOS structure always appears at on the Fermi level at finite temperatures.

3.4.3 Effects of SPETs on the magnetic susceptibility

We show that the SPETs induce a nontrivial response to the magnetic field; the low energy excitations enclosed by the SPETs make the magnetic susceptibility of the B-sublattice larger than that of the A-sublattice, although the interaction strength is opposite ($U_A > U_B$). The mechanisms are as follows. As seen in Fig.3.5(c), at $\omega = 0$, the LDOS for B-sublattice becomes larger than that for A-sublattice because of SPETs as shown in Eq. (3.41). This fact indicates that the response to the Zeeman splitting for B-sublattice becomes larger than that for A-sublattice. Therefore, the magnetic moment of B-sublattice can becomes larger than that of A-sublattice.

The numerical data supporting the above scenario are shown in Fig. 3.9(a) and (b). The former (the latter) data are obtained at $U_B = U_A/2$ ($U_B = 0$). In Fig. 3.9(a), we can see that the magnetic susceptibility for B-sublattice becomes larger than that for A-sublattice, corresponding to the emergence of the low energy excitations enclosed by the SPETs (for the LDOS at $U_B = U_A/2$ and for the self-energy as shown in Figs. 3.8(a) and 3.8(b). We can also observe similar behaviors at $U_B = 0$ although the region of $\chi^s_B > \chi^s_A$ is narrow in this extreme limit. We stress that essential ingredients are the difference in the lifetime of the self-energy and the chiral symmetry. Therefore, the above enhancement is generic and considered to be observed for any two-sublattice model where the self-energy satisfies $|\mathrm{Im}\Sigma^R_A(\omega = 0)| > |\mathrm{Im}\Sigma^R_B(\omega = 0)|$.

3.5 Summary

In this chapter, we have studied chiral-symmetric correlated NLSMs in three dimensions with special emphasis on non-Hermitian properties. Concretely, we have elucidated the emergence of SPETs for a diamond lattice model with spatially modulated Hubbard interaction. Essential difference from the case for NLSMs with PT symmetry studied so far is that the present SPETs with chiral symmetry and the associated low energy excitations

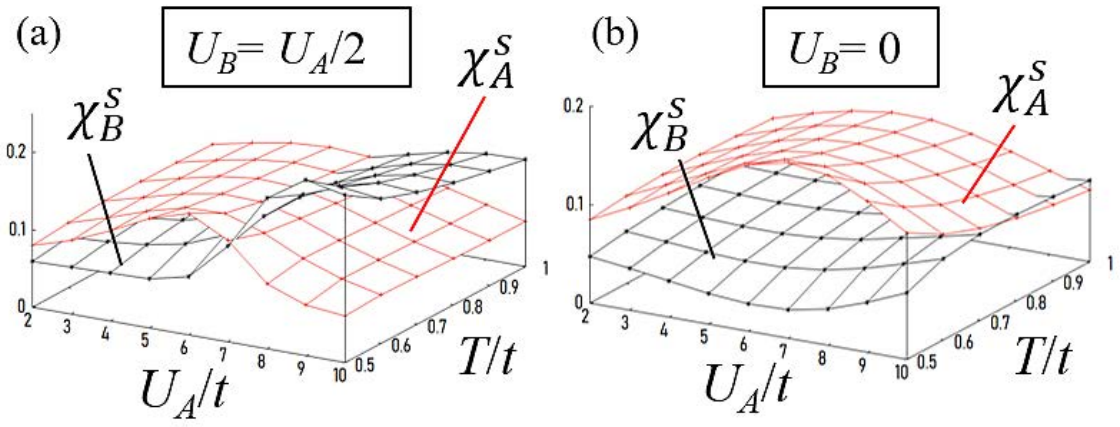

Fig. 3.9: The magnetic susceptibility for each sublattice $\chi^s_\alpha(\boldsymbol{q} = 0, i\epsilon_m = 0)$, $\alpha = A, B$ as functions of temperature T/t and interaction U_A/t. Panel (a) [(b)] are obtained at $U_B = U_A/2$ (at $U_B = 0$) with RPA. Reprinted figure with premission from [264] Copyright 2019 by the American Physical Society.

(i.e., Fermi volumes) are fixed to the Fermi level. Furthermore, we have elucidated that these low energy excitations result in counterintuitive behaviors which are the first results exemplifying the effects of SPETs on magnetic responses. Specifically, by employing by DMFT and RPA, we have found that due to the Fermi volumes, magnetic susceptibility for B-sublattice becomes larger than that for A-sublattice, although the interaction strength is opposite ($U_A > U_B$). For this counterintuitive response to the homogeneous magnetic field, the chiral symmetry is essential which leads to the enhancement of LDOS at the Fermi level only for B-sublattice.

One may wonder whether SPETs persist when we go beyond the DMFT-IPT[259–261]. We consider that they persist because of the following reasons. (i) It is well-known that the IPT method gives qualitatively correct results for systems with particle-hole symmetry. Indeed, the DMFT combined with the numerical renormalization group method elucidates the emergence of symmetry-protected exceptional rings for two-dimensional systems with chiral symmetry[226] which can be regarded as a cross section of SPETs in three dimensions. (ii) The chiral symmetry ensures that the spatial fluctuations do not destroy the SPETs. The symmetry constraint in Eq. (3.28) for $\omega = 0$ ensures that the effective Hamiltonian can be written in the form of Eq. (3.32), indicating that the SPETs persist even in the presence of spatial fluctuations. The details study on this point is left for future work.

We finish this chapter with comments on future studies. Important open questions are (i) finding experimental setups or candidate materials showing SPETs and (ii) elucidating how to observe the unique magnetic response elucidated in this chapter. Concerning the toy model analyzed in this chapter, we expect that it can be realized for cold atoms by employing optical Feshbach resonance[262, 263]. In such systems, the unique magnetic response might be observed by noise correlations or Bragg scattering of light which have been employed to observe the spin correlation functions[265, 266]. In addition, elucidating effects of non-Hermitian band structures on magnetic responses for other cases of symmetry remains an important future work.

3.6 Appendix for this chapter: Numerical data

3.6.1 SPET of the anisotropic diamond lattice

We show the results of anisotropic diamond lattices in Fig. 3.10. The shape of SPETs is determined from the band touching point of Eqs. (3.10) and (3.37). The topological phase transition occurs between $t_0/t_i = 1.49$ and $t_0/t_i = 1.5$, between $t_0/t_i = 2.5$ and $t_0/t_i = 3.0$.

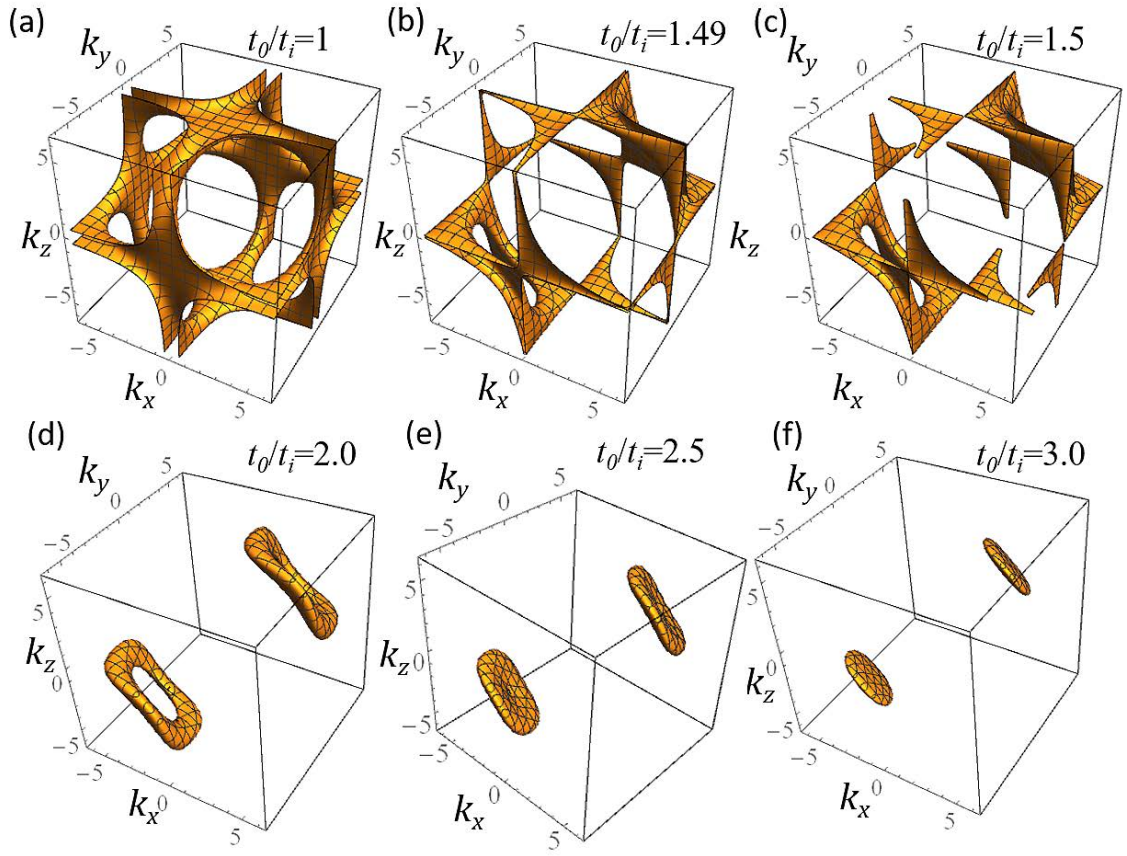

Fig. 3.10: SPETs for anisotropic diamond lattices with $t_0/t_i \neq 1, i = 1,2,3, t_i = 1$ and $\mathrm{Im}\Sigma_A^R(\omega = 0) = -1$ in three-dimensional BZ. Reprinted figure with premission from [264] Copyright 2019 by the American Physical Society.

Chapter 4

Probing three-state Potts nematic fluctuations by ultrasound attenuation

4.1 Introduction to this chapter

Electron-nematic states, which break a certain point group symmetry of the electronic system, have attracted much attention because of the appearance in many unconventional superconductors ubiquitously. To reveal the relationship between electron-nematic state and unconventional superconductivity has been a central subject in present condensed matter physics. For example, in iron-based superconductors, it has been shown that the lattice C_4-breaking electron nematic state originates from an orbital order and its orbital fluctuation leads to unconventional superconductivity. In many materials, such as cuprates, iron-based compounds, heavy-fermions, doped-Bi_2Se_3, and magic-angle twisted-bilayer graphene (MA-TBG), various electron-nematic states have been reported. As we have mentioned in Sec. 1.2.3, one of the most interesting features of electron-nematic states is that these are intertwined with other ordered phases and topological phases.

Since the experimental discovery of unconventional superconducting states near Mott insulating phases, MA-TBG has attracted much attention for the interplay[145–158] between band topology and strong Coulomb interaction caused by the moiré interference pattern. In this material a lattice C_3-breaking electron-nematic state[164–167], which is referred to as a three-state Potts nematic states, has also been reported, and it is of interest for its competition with nematic superconductivity[167] and for the mystery of the Landau level degeneracy[167–169]. But, no clear evidence of intrinsic phase transition has been found, and the phase diagram is still unclear. The three-state Potts nematic state has also been reported in doped-Bi_2Se_3[186–188] above the superconducting transition temperature, which is also a candidate material of nematic superconductors[177–185]. Theoretically, an exotic scenario has been proposed as the electron-nematic state caused by the strong superconducting fluctuation, referred to as a vestigial nematic state[126, 127, 143, 188], but there is no strong evidence to support it. Besides revealing the microscopic origin of nematicity and the relation with superconductivity, one of the important problems is to identify the critical behavior of electron-nematic states and to distinguish whether it is intrinsic (i.e. induced spontaneously) or extrinsic (i.e. due to trivial strains, the structural distortion or an effect of the substrate).

In this chapter, we investigate the impact of critical nematic fluctuations on phonons, which in turn enables us to identify the nematic properties by ultrasound attenuation experiments. Despite a lot of research, the identification of such a three-state Potts nematic state and the clarification of whether it is induced spontaneously or from trivial strains

are not an easy task. We analyze the influence of the nemato-elastic coupling on the low energy properties of phonons by a phenomenological argument using a Ginzburg-Landau-Wilson (GL) action[267] and a model calculation based on the Hubbard model. It is shown that nematic fluctuations induce an isotropic divergence of the transverse sound attenuation coefficient, which is defined as the inverse of the phonon mean free path.

This chapter is organized as follows. In Sec. 4.2, we present a phenomenological argument to see how the critical nematic fluctuation affects the properties of phonon. First, in Sec. 4.2.1, we discuss the Landau damping for the C_3 -breaking bond-order fluctuation. Second, in Sec. 4.2.2, we analyze the influence of the nemato-elastic coupling on the acoustic phonons. In Sec. 4.3, we present a model calculation of nematicity and discuss a mean-field phase diagram. First, from Sec. 4.3.1 to Sec. 4.3.3, we derive the mean-field theory of the three-state Potts neamtic phase transtion. Second, in Sec. 4.3.4, we show the phase diagrams and, in Sec. 4.3.5, we show the sound attenuation coefficients. In Sec. 4.4, we give a brief discussion on the application of our results. Sec. 4.5 is devoted to the summary of this chapter. Finally, in Sec. 4.6, we note for some formulas.

4.2 Phenomenological approach to the impact of critical nematic fluctuations on phonons

In this section, we present a phenomenological theory to show how the ultrasound attenuation detects the critical nematic fluctuations. In the following subsection, to consider how to capture the signature of the intrinsic nematic phase transition, we focus on the impact of critical nematic fluctuations on low-energy properties of acoustic phonons.

First, we deal with the nematic phase transition phenomenologically. In hexagonal lattices, such as MA-TBG and doped-Bi_2Se_3, the nematic order is described by a two-component order parameter $\mathbf{\Phi} = (\Phi_1, \Phi_2)$, which belongs to a two-dimensional representation of the point group D_3[174], D_6[171] and D_{3d}[143], in the three-state Potts-model class. The GL action for the nematic fluctuation[171] on the two-dimensional system is given as follows:

GL action for the three-state Potts nematic phase transition

$$S_{\rm nem}[\mathbf{\Phi}] = \int d^2\boldsymbol{r}d\tau\left[\frac{1}{2}r\Phi_+\Phi_- + \frac{1}{6}u_3(\Phi_+^3+\Phi_-^3) + \frac{1}{4}u_4(\Phi_+\Phi_-)^2\right] \quad (4.1)$$

where $\Phi_\pm = \Phi_1(x) \pm i\Phi_2(x)$, $x = (\boldsymbol{r}, \tau)$ and GL coefficients r, u_3, u_4.

$\mathbf{\Phi}$ is naturally parametrized as $\mathbf{\Phi} = \Phi(\cos 2\theta, \sin 2\theta)$, where the angle θ can be identified with the orientation of the nemetic director $\hat{n} = (\cos\theta, \sin\theta)$ with angle 2θ reflecting the invariance of π rotation. The cubic term reflects the hexagonal anisotropy and is expressed as

$$\frac{1}{6}u_3(\Phi_+^3+\Phi_-^3) = \frac{1}{6}u_3\Phi^3\cos 6\theta, \quad (4.2)$$

which is minimized at $\theta = 2n\pi/6 = \{0, \pi/3, 2\pi/3\}$ for $u_3 < 0$ and $\theta = (2n+1)\pi/6 = \{\pi/6, \pi/2, 5\pi/6\}$ for $u_3 > 0$. These solutions represent threefold degenerate nematic directors.

When we consider the Gaussian fluctuation region, the corresponding action for nematic fluctuation is given by

$$S_{\text{Gauss}}[\mathbf{\Phi}] = \sum_{q} \mathbf{\Phi}_q \left[\hat{\chi}_d^{-1}(\boldsymbol{q}, i\epsilon_m)\right] \mathbf{\Phi}_q^*, \tag{4.3}$$

with $q = (\boldsymbol{q}, i\epsilon_m)$, the boson Matsubara frequency ϵ_m, and $\Phi_{iq}^* = \Phi_{i-q}$, because of $\Phi_i(x) \in \mathbb{R}$. Here,

$$\hat{\chi}_d^{-1}(\boldsymbol{q}, i\epsilon_m) = (r + \xi_0^2 \boldsymbol{q}^2)\mathbb{1} + \hat{D}\left(\frac{|\epsilon_m|}{\Gamma_d(\boldsymbol{q})}\right), \tag{4.4}$$

is the matrix of the d-wave density correlation function, where $r \propto T_{c0} - T$ measures the distance from the mean-field transition temperature T_{c0}, with the mean-field correlation length ξ_0 and the damping rate $\Gamma_d(\boldsymbol{q})$. The Landau damping term[1] $\hat{D}\left(\frac{|\epsilon_m|}{\Gamma_d(\boldsymbol{q})}\right)$ depends on the type of order parameter and the microscopic details of the system.

In the following subsection, we derive the functional form of $\hat{D}\left(\frac{|\epsilon_m|}{\Gamma_d(\boldsymbol{q})}\right)$ coming from the C_3-breaking bond-order (see Eq. (4.5)), which is an example of the three-state Potts nematic order. Remarkably, we find that the C_3-breaking case has an isotropic angular dependence of the Landau damping, in sharp contrast to the strong angle dependence of the Landau damping in the case of the C_4-breaking bond-order[135, 268] which is an example of the Ising nematic order.

4.2.1 Phenomenology of a C_3-breaking bond-order fluctuation

According to the standard Hertz-Millis-Moriya description[129, 131–133], the dynamics of a ferroic order parameter which couples to an itinerant electron system is overdamped at low frequency. This is based on the simplest treatment of the critical order parameter fluctuation. On the other hand, the dynamics of electron-nematicity is more complicated[125, 128, 129]. For example, in isotropic Fermi liquids, the order parameter fluctuation of the d-wave Pomeranchuk instability is decomposed into a ballistic ($z = 2$) transverse mode and an overdamped ($z = 3$) longitudinal mode, where z is a dynamical critical exponent[2]. This nature leads to various intriguing properties unique to the nematic quantum critical point such as an unusual non-Fermi liquid behavior[130, 269, 270] and the multiscale quantum criticality[271]. Moreover, in lattice systems with C_4-breaking bond-order fluctuation, the appearance of a ballistic mode and its effect on the critical properties have been discussed[135, 268].

In this subsection, we derive the functional form of the Landau damping $\hat{D}\left(\frac{|\epsilon_m|}{\Gamma_d(\boldsymbol{q})}\right)$, as follows:

[1] The Landau damping term appears as a self-energy correction due to the coupling between the nematic fluctuations to the itinerant electron system. The critical dynamics is generated by the excitation of particle-hole pairs in the Fermi sea and the dynamical critical exponent is determined by this frequency dependent term. We note that Landau damping requires electrons to scatter along the Fermi surface.

[2] A ballistic mode (an overdamped mode) shows $D \propto \frac{|\epsilon_m|^2}{|q|^2}$ ($D \propto \frac{|\epsilon_m|}{|q|^3}$) with a dynamical exponent $z = 2$ ($z = 3$). The former is called as a ballistic mode without damping, while the latter involves overdamping due to the particle-hole pair creation.

Gaussian fluctuation theory

$$S_{\rm Gauss}[\Phi] \;=\; \sum_q \Phi_q \Big[r + \xi_0^2 \boldsymbol{q}^2 - D_q \Big] \Phi_q^*,\; D_q = -\frac{\rho_0}{2} \frac{|\omega_m|}{v_{\rm F}|\boldsymbol{q}|}, \tag{4.5}$$

with $q = (\boldsymbol{q}, i\epsilon_m)$, the boson Matsubara frequency ϵ_m, the density of states at the Fermi level ρ_0 and the Fermi velocity $v_{\rm F}$, where $r \propto T_{c0} - T$ measures the distance from the mean-field transition temperature T_{c0}, with the mean-field correlation length ξ_0.

The coupling term between the nematic fluctuation and the electrons

Let us begin by asking what happens for the dynamics of the nematic fluctuation for the C_3-breaking bond-order case which is one of the microscopic origins of electron-nematicity. For simplicity, we assume a circular Fermi surface around the Γ point and the single band system in a C_3 symmetric lattice. The interaction between the nematic fluctuation (Φ_{1q}, Φ_{2q}) and the electrons $(c_k^\dagger, c_k)$ resulting from the Hubbard-Stratonovich transformation is given by

$$\mathcal{H}_{\rm coup} \;\propto\; \sum_{q,k} \Big[d_{1k} \Phi_{1q} + d_{2k} \Phi_{2q} \Big] c_{k+q/2}^\dagger c_{k-q/2}, \tag{4.6}$$

where form factors of a two-dimensional representation are $d_{1k} \sim (\hat{k}_x^2 - \hat{k}_y^2) = \cos 2\theta_k$ and $d_{2k} \sim 2(\hat{k}_x \hat{k}_y) = \sin 2\theta_k$ with the wave vector of electron $\boldsymbol{k} = |\boldsymbol{k}|(\hat{k}_x, \hat{k}_y) = |\boldsymbol{k}|(\cos\theta_k, \sin\theta_k)$. It reflects a two-dimensional representation of a C_3 symmetric lattice, meaning that two waves, $d_{x^2-y^2}$-wave and d_{xy}-wave, cannot be treated separately. Furthermore, the order parameter is parametrized as $\boldsymbol{\Phi} = \Phi(\cos 2\theta, \sin 2\theta)$ with the nematic director $\hat{n} = (\cos\theta, \sin\theta)$ and its angle θ. The coupling term is expressed in terms of the relative angle between the wave vector and the nematic director $(\theta_k - \theta)$ as follows,

$$\mathcal{H}_{\rm coup} \;\propto\; \sum_{q,k} \Phi_q \cos 2(\theta_k - \theta) c_{k+q/2}^\dagger c_{k-q/2}, \tag{4.7}$$

where we have used $\Phi_{1q} = \Phi_q \cos 2\theta$, $\Phi_{2q} = \Phi_q \sin 2\theta$ and the coupling term vanishes at $\theta_k - \theta = \pm\pi/4$.

Nematic polarization for a circular Fermi surface

The low-energy contribution of a nematic polarization matrix $\chi_q^{ij} = \frac{T}{N} \sum_k d_{ik} d_{jk} G_k G_{k+q}$ with $i, j = 1, 2$ and an electron Green's function $G_k^{-1} = i\omega_n - \epsilon_k - \mu$, the energy dispersion $\epsilon_k = \boldsymbol{k}^2/2m$ and the electron mass m, determines the dynamical properties of the nematic polarization

$$\begin{aligned} D_{\boldsymbol{q}, i\epsilon_m}^{ij} \;&=\; \chi_{\boldsymbol{q}, i\epsilon_m}^{ij} - \chi_{\boldsymbol{q},0}^{ij} \sim -i\epsilon_m \rho_0 \int_{k_{\rm FS}} \frac{d_{ik} d_{jk}}{i\epsilon_m - v_{\rm F} \boldsymbol{k} \cdot \boldsymbol{q}}, \\ &=\; -\frac{i\epsilon_m}{v_{\rm F}|\boldsymbol{q}|} \rho_0 \int_0^{2\pi} \frac{d\theta_k}{2\pi} \frac{d_{ik} d_{jk}}{i\epsilon_m / v_{\rm F}|\boldsymbol{q}| - \cos(\theta_k - \theta_q)}, \end{aligned} \tag{4.8}$$

with ρ_0 is the density of states at the Fermi level, the Fermi velocity $v_{\rm F}$ and the boson Matsubara frequency ϵ_m. Now we set $\psi = (\theta_k - \theta_q)$ and rewrite each component of $d_{ik}d_{jk}$ as,

$$\begin{aligned}
d_{1k}d_{1k} &= \cos^2 2\theta_k = \cos^2(2\psi + 2\theta_q) \\
&\sim \cos^2 2\theta_q \cos^2 2\psi + \sin^2 2\theta_q \sin^2 2\psi, \qquad (4.9)\\
d_{2k}d_{2k} &= \sin^2 2\theta_k = \sin^2(2\psi + 2\theta_q) \\
&\sim \cos^2 2\theta_q \sin^2 2\psi + \sin^2 2\theta_q \cos^2 2\psi, \qquad (4.10)\\
d_{1k}d_{2k} &= \frac{1}{2}\sin 4\theta_k = \frac{1}{2}\sin(4\psi + 4\theta_q) \\
&\sim \frac{1}{2}\cos 4\theta_q \sin 4\psi + \frac{1}{2}\sin 4\theta_q \cos 4\psi = \frac{1}{2}\sin 4\theta_q (2\cos^2 2\psi - 1) \qquad (4.11)
\end{aligned}$$

where we have ignored terms proportional to $\sin 2\psi \cos 2\psi$, because they vanish after ψ integral. Combined with the above equations, the dynamical part of nematic polarization $\hat{D}_q = \hat{\chi}_q - \hat{\chi}_{q,0}$ is calculated as,

$$D_q^{ij} = -ia\rho_0 \int_0^{2\pi} \frac{d\psi}{2\pi} \frac{d_{ik}d_{jk}}{ia - \cos\psi}, \qquad (4.12)$$

with $a = \frac{\epsilon_m}{v_{\rm F}|\boldsymbol{q}|}$, the shorthand notation $q = (\boldsymbol{q}, i\epsilon_m)$ and

$$\begin{aligned}
D_q^{11} &= ia\rho_0 \Big\{ \cos^2 2\theta_{\boldsymbol{q}} \Big[i{\rm Sgn}(a) - 2ia \Big] + \sin^2 2\theta_{\boldsymbol{q}} \Big[2ia \Big] \Big\}, \qquad (4.13)\\
D_q^{22} &= ia\rho_0 \Big\{ \cos^2 2\theta_{\boldsymbol{q}} \Big[2ia \Big] + \sin^2 2\theta_{\boldsymbol{q}} \Big[i{\rm Sgn}(a) - 2ia \Big] \Big\}, \qquad (4.14)\\
D_q^{12} &= ia\rho_0 \Big\{ \sin 4\theta_{\boldsymbol{q}} \Big[i{\rm Sgn}(a) - 2ia \Big] - \frac{1}{2}\sin 4\theta_{\boldsymbol{q}} \Big[i{\rm Sgn}(a) \Big] \Big\}, \qquad (4.15)
\end{aligned}$$

with $D_q^{12} = D_q^{21}$. We have used the following equations in the above calculations,

$$\begin{aligned}
I_C(a) &= -\int_0^{2\pi} \frac{d\psi}{2\pi} \frac{\cos^2 2\psi}{ia - \cos\psi}, \\
&= i(1 + 2a^2) \Big[\frac{(1 + 2a^2)}{\sqrt{1 + a^2}} {\rm Sgn}(a) - 2a \Big] |_{a\to 0} \to i{\rm Sgn}(a) - 2ia, \qquad (4.16)\\
I_S(a) &= -\int_0^{2\pi} \frac{d\psi}{2\pi} \frac{\sin^2 2\psi}{ia - \cos\psi}, \\
&= 2ai \Big[1 + 2a^2 - 2|a|\sqrt{1 + a^2} \Big] |_{a\to 0} \to 2ia. \qquad (4.17)
\end{aligned}$$

Here, $a \to 0$ means the static limit ($|\epsilon_m| \gg v_{\rm F}|\boldsymbol{q}|$) and we evaluate the leading order component of a in the above integral. After using the above integration to Eq. (4.12), the dynamical part of the nematic polarization matrix in the static region ($|\epsilon_m| \gg v_{\rm F}|\boldsymbol{q}|$) is,

$$\hat{D}_q = -\frac{a\rho_0}{2} \begin{pmatrix} 1 & 0 \\ 0 & 1 \end{pmatrix} - \rho_0 \Big[\frac{a}{2} - 2a^2 \Big] \begin{pmatrix} \cos 4\theta_{\boldsymbol{q}} & \sin 4\theta_{\boldsymbol{q}} \\ \sin 4\theta_{\boldsymbol{q}} & -\cos 4\theta_{\boldsymbol{q}} \end{pmatrix}. \qquad (4.18)$$

At first glance, this would seemingly break the C_3-symmetry, but later calculations show that the C_3-rotation symmetry is preserved when the angle of the nematic directors is taken into account.

Next, we express the above function in terms of the angle of nematic director θ and consider the dynamical part of Eq. (4.3),

$$\begin{aligned}\boldsymbol{\Phi}_q^T \hat{D}_q \boldsymbol{\Phi}_q^* &= \Phi_q \begin{pmatrix} \cos 2\theta & \sin 2\theta \end{pmatrix} \hat{D}_q \begin{pmatrix} \cos 2\theta \\ \sin 2\theta \end{pmatrix} \Phi_q^*, \\ &= -\Phi_q \rho_0 \Big[\frac{|\epsilon_m|}{v_{\mathrm{F}}|\boldsymbol{q}|} \cos^2(2\theta_{\boldsymbol{q}} - 2\theta) - 2 \frac{|\epsilon_m|^2}{(v_{\mathrm{F}}|\boldsymbol{q}|)^2} \cos(4\theta_{\boldsymbol{q}} - 4\theta) \Big] \Phi_q^*, \end{aligned} \tag{4.19}$$

where $\boldsymbol{\Phi}_q = \Phi_q(\cos 2\theta, \sin 2\theta)$ and Φ_q is the norm of $\boldsymbol{\Phi}_q$. Thus the Gaussian action including the above discussion is rewritten as

$$S_{\mathrm{Gauss}}[\boldsymbol{\Phi}] = \sum_q \boldsymbol{\Phi}_q^T \Big[(r + \xi_0^2 \boldsymbol{q}^2) \mathbb{1} + \hat{D}_q \Big] \boldsymbol{\Phi}_q^*, \tag{4.20}$$

$$\boldsymbol{\Phi}_q^T \hat{D}_q \boldsymbol{\Phi}_q^* = -\Phi(q) \rho_0 \Big[\frac{|\epsilon_m|}{v_{\mathrm{F}}|\boldsymbol{q}|} \cos^2(2\theta_{\boldsymbol{q}} - 2\theta) - 2 \frac{|\epsilon_m|^2}{(v_{\mathrm{F}}|\boldsymbol{q}|)^2} \cos(4\theta_{\boldsymbol{q}} - 4\theta) \Big] \Phi^*(q). \tag{4.21}$$

where $r \propto T_{c0} - T$ measures the distance from the mean-field transition temperature T_{c0}, where the mean-field correlation length is ξ_0.

Result: Isotropic angular dependence of the Landau damping

The orientations of the nematic directors are restricted to three directions by the cubic term in Eq. (4.1) as follows, $\theta = \{0, 2\pi/3, 4\pi/3\}$ for $u_3 < 0$ and $\theta = \{-\pi/6, \pi/2, 7\pi/6\}$ for $u_3 > 0$. Precisely speaking, the damping term preserves this $\mathbb{Z}_3$ symmetry in disordered state, thus we need to treat three angles equivalently in the above Eq. (4.21).

$$\begin{aligned} & \cos^2(2\theta_{\boldsymbol{q}} - 2\theta) \\ \to\ & \frac{1}{3} \Big[\cos^2(2\theta_{\boldsymbol{q}}) + \cos^2(2\theta_{\boldsymbol{q}} - \frac{2\pi}{3}) + \cos^2(2\theta_{\boldsymbol{q}} - \frac{4\pi}{3}) \Big], \qquad (4.22) \\ =\ & \frac{1}{3} \Big[\cos^2(2\theta_{\boldsymbol{q}}) + \frac{1}{2} \cos^2(2\theta_{\boldsymbol{q}}) + \frac{3}{2} \sin^2(2\theta_{\boldsymbol{q}}) \Big] = \frac{1}{2}. \qquad (4.23) \end{aligned}$$

Eventually, within this treatment, there is no anisotropy of Landau damping in the three-state Potts nematic case, and thus we arrive at the following action with the single component scalar field Φ

$$S_{\mathrm{Gauss}}[\Phi] = \sum_q \Phi(q) \Big[\chi_d^{-1}(q) \Big] \Phi^*(q), \tag{4.24}$$

$$\chi_d^{-1}(q) = r + \xi_0^2 \boldsymbol{q}^2 + \frac{|\epsilon_m|}{\Gamma_d(\boldsymbol{q})}, \tag{4.25}$$

with $\boldsymbol{\Phi} = \Phi(\cos 2\theta, \sin 2\theta)$ and the damping rate $\Gamma_d^{-1}(\boldsymbol{q}) = \frac{\rho_0}{2v_{\mathrm{F}}} |\boldsymbol{q}|^{-1}$. We conclude that the C_3-breaking bond-order fluctuation leads to an isotropic angular dependence of the Landau damping as shown in Eq. (4.5).

Comparison with the Ising nematic order

The above results are quite contrasted to the Ising nematic case where the nematic director is forced to be $\theta = \{0, \pi/2\}$ for $d_{x^2-y^2}$-wave. In that case, the term $D\left(\frac{|\epsilon_m|}{\Gamma_d(\boldsymbol{q})}\right)$ in Eq. (4.4) is expressed as the following anisotropic form[135, 268] as

$$D\left(\frac{|\epsilon_m|}{\Gamma_d(\boldsymbol{q})}\right) = \rho_0\left[\frac{|\epsilon_m|}{v_{\rm F}|\boldsymbol{q}|}\cos^2 2\theta_{\boldsymbol{q}} - 2\frac{|\epsilon_m|^2}{(v_{\rm F}|\boldsymbol{q}|)^2}\cos 4\theta_{\boldsymbol{q}}\right], \tag{4.26}$$

which leads to the angle dependent dynamics of nematic fluctuation. It is possible to understand from the coupling term in Eq. (4.7) what is responsible for these differences between the three-state Potts nematicity and the Ising nematicity, as follows. The dynamics of nematic fluctuation is damped due to particle-hole pair excitations close the Fermi surface, which is a source of the Landau damping. It requires electrons to scatter along the Fermi surface. One of the unique properties of bond-orders is the presence of the nodal structure in the form factor[135, 268]. This implies that a particle-hole pair creation is prohibited at certain directions, leading to a large anisotropy in physical quantities. For example, in the case of the Ising nematicity, the nematic director is forced to be $\theta = \{0, \pi/2\}$ for $d_{x^2-y^2}$-waves, so that the coupling term vanishes at $\theta_{\boldsymbol{k}} = \pm\pi/4$ in Eq. (4.7). On the contrary, the three-state Potts nematic case of our interest does not have such a specific direction of vanishing coupling because nematic directors are not orthogonal to each other, as we have discussed in this subsection.

4.2.2 Probing the nematicity through acoustic phonons

In addition to the angle dependence of the Landau damping $\hat{D}\left(\frac{|\epsilon_m|}{\Gamma_d(\boldsymbol{q})}\right)$ in Eq. (4.4), there is a unique character in the nematic order; the nematic order parameter couples linearly to acoustic phonon modes[134–136, 143, 171, 272, 273]. This is essentially different from the cases of other ferroic orders, e.g., ferromagnetism or superconductivity whose order parameters only couple to the totally symmetric mode of phonon in quadratic order. Because of this specific form of coupling, the unique properties are reflected in the transverse acoustic phonon. As a result, through the linear nemato-elastic coupling, phonon modes affect the thermodynamic and transport properties near the nematic quantum critical point.

Despite a lot of research, an identification of the electron-nematic phase transition and clarifying whether it is induced spontaneously or from trivial strains is not an easy task. The ultrasound attenuation of acoustic phonons is one of the good techniques of identifying the electron-nematic phase transition and its critical behavior. It is also pointed out that the selection rules of ultrasound attenuation coefficients can determine the Ising nematic phase transition[134]. In this section, we focus on the impact of nemato-elastic coupling on the acoustic phonons.

Acoustic phonon

First we consider the dynamical properties of two acoustic phonon modes, a transverse (T) and a longitudinal (L) one with sound velocity $v_{T(L)}$. The displacement field $\boldsymbol{u}$ is decomposed into two modes $\boldsymbol{u}_{\mu=T,L} = \tilde{u}_\mu \hat{\boldsymbol{e}}_\mu$ with $\hat{\boldsymbol{e}}_T = (-\sin\theta_{\boldsymbol{q}}, \cos\theta_{\boldsymbol{q}})$, $\hat{\boldsymbol{e}}_L = (\cos\theta_{\boldsymbol{q}}, \sin\theta_{\boldsymbol{q}})$ and $\theta_{\boldsymbol{q}} = \tan^{-1}(q_y/q_x)$. The elastic action for two acoustic phonon modes reads[267],

The elastic action for the acoustic phonon

$$S_{\rm ph}[\boldsymbol{u}] = \frac{\rho}{2}\sum_{\mu=T,L}\sum_{q}\tilde{u}_{\mu}(q)K_{\mu}(q)\tilde{u}^{*}_{\mu}(q), \tag{4.27}$$

$$K_{\mu}(q) = K^{(0)}_{\mu}(q) - \delta K_{\mu}(q), \tag{4.28}$$

with $q = (\boldsymbol{q}, i\epsilon_m)$, the full (bare) inverse propagator $K_\mu(K^{(0)}_\mu)$, the phonon self-energy δK_μ, the boson Matsubara frequency $\epsilon_m = 2\pi T m$ and the mass density ρ.

The bare inverse propagator has the form

$$K^{(0)}_{\mu} = \epsilon_m^2 + v_\mu^2\boldsymbol{q}^2. \tag{4.29}$$

The sound attenuation coefficient[274] α_μ is defined as the inverse of the phonon mean-free path, as follows

$$\alpha_\mu(\boldsymbol{q}) = -\lim_{\omega\to 0}\frac{1}{v_\mu\omega}\mathrm{Im}K^R_\mu(\boldsymbol{q},\omega), \tag{4.30}$$

where $K^R_\mu(\boldsymbol{q},\omega)$ is the retarded function of the full inverse propagator.

Nemato-elastic coupling

In general, the lowest order of the symmetry-allowed nemato-elastic coupling[143, 171] in the free energy is

$$F_{\rm nem-ph}[\boldsymbol{\Phi},\boldsymbol{u}] = -\kappa\int d^2\boldsymbol{r}\Big[(\epsilon_{xx}-\epsilon_{yy})\Phi_1 + 2\epsilon_{xy}\Phi_2\Big], \tag{4.31}$$

with the coupling constant κ and the strain tensor $\epsilon_{ij} = \frac{1}{2}(\partial_i u_j + \partial_j u_i)$. Considering the nemato-elastic coupling $S_{\rm nem-ph} = \int_0^\beta d\tau F_{\rm nem-ph}$, we calculate the effective action for phonons coupled with nematic fluctuation.

Nemato-elastic coupling

$$S_{\rm nem-ph}[\Phi,\boldsymbol{u}] = -\kappa\sum_q i\frac{|\boldsymbol{q}|}{2}\Big[\tilde{u}_L(q)-\tilde{u}_T(q)\Big]\Phi^*(q). \tag{4.32}$$

Here, we derive the nemato-elastic coupling (see Eq. (4.37)). In terms of $\tilde{u}_L(q)$ and $\tilde{u}_T(q)$, the nemato-elastic action reads

$$\begin{aligned} S_{\rm nem-ph}[\boldsymbol{\Phi},\boldsymbol{u}] &= -\kappa\sum_q \begin{pmatrix}\tilde{u}_L(q) & \tilde{u}_T(q)\end{pmatrix} i|\boldsymbol{q}| \begin{pmatrix}\cos 2\theta_{\boldsymbol{q}} & \sin 2\theta_{\boldsymbol{q}} \\ -\sin 2\theta_{\boldsymbol{q}} & \cos 2\theta_{\boldsymbol{q}}\end{pmatrix}\begin{pmatrix}\Phi_1(-q)\\ \Phi_2(-q)\end{pmatrix}, \\ &= -\kappa\sum_q \begin{pmatrix}\tilde{u}_L(q) & \tilde{u}_T(q)\end{pmatrix} i|\boldsymbol{q}| \begin{pmatrix}\cos(2\theta_{\boldsymbol{q}}-2\theta) \\ -\sin(2\theta_{\boldsymbol{q}}-2\theta)\end{pmatrix}\Phi^*(q), \end{aligned} \tag{4.33}$$

where $\theta_{\boldsymbol{q}}$ shows the propagating direction of a wave vector $\boldsymbol{q}$. In the second line, we have used $\boldsymbol{\Phi} = \Phi(\cos 2\theta, \sin 2\theta)$ with the angle of nematic director θ.

In the case of the Ising nematicity, the nematic director is forced to be $\theta = \{0, \pi/2\}$ for $d_{x^2-y^2}$-wave. Even if we treat the two angles equally, the anisotropy of the nemato-elastic coupling remains, as follows,

$$\cos^2(2\theta_{\boldsymbol{q}} - 2\theta) \quad \to \quad \cos^2(2\theta_{\boldsymbol{q}}), \tag{4.34}$$

$$\sin^2(2\theta_{\boldsymbol{q}} - 2\theta) \quad \to \quad \sin^2(2\theta_{\boldsymbol{q}}). \tag{4.35}$$

This form is the same as in Ref. [135]. However, in the case of the three-state Potts nematicity, treating the three angles equally does not show any anisotropy. Thus we conclude that $\mathbb{Z}_3$ symmetry leads to an isotropic angular dependence of the nemato-elastic coupling.

$$\cos^2(2\theta_{\boldsymbol{q}} - 2\theta) \quad \to \quad \frac{1}{2}, \ \sin^2(2\theta_{\boldsymbol{q}} - 2\theta) \to \frac{1}{2}. \tag{4.36}$$

Treating the three angles equally does not show anisotropy, with a similar argument as before, and thus we obtain the following form

$$S_{\mathrm{nem-ph}}[\Phi, \boldsymbol{u}] \quad = \quad -\kappa \sum_{q} i \frac{|\boldsymbol{q}|}{2} \left[\tilde{u}_L(q) - \tilde{u}_T(q) \right] \Phi^*(q). \tag{4.37}$$

Therefore we conclude that the nemato-elastic coupling has an isotropic angular dependence.

Result: Phonon's properties affected by the nematio-elastic coupling

After integrating out the nematic order parameter field in the total action $S_{\mathrm{tot}} = S_{\mathrm{Gauss}}[\Phi] + S_{\mathrm{ph}}[\boldsymbol{u}] + S_{\mathrm{nem-ph}}[\Phi, \boldsymbol{u}]$, an additional contribution to the phonon Green's function in Eq. (4.28) is

$$\delta K_\mu(q) = \frac{\kappa^2 \boldsymbol{q}^2}{2\rho} \chi_d(q). \tag{4.38}$$

Indeed, up to the leading order correction, we can confirm that the self-energy has no anisotropy.

As a consequence, we obtain the full inverse propagator for phonons in Eq. (4.28), which gives rise to the renormalization of sound velocities as,

$$\begin{aligned} v_\mu^* &= v_\mu \sqrt{1 - \frac{\mathrm{Re}\delta K_\mu^R(\boldsymbol{q}, \omega \to 0)}{v_\mu^2 q^2}}, \\ &= v_\mu \sqrt{1 - \frac{\kappa^2}{2 v_\mu^2 \rho} \mathrm{Re}\chi_d^R(\boldsymbol{q}, \omega \to 0)}. \end{aligned} \tag{4.39}$$

Note that a sound velocity renormalization implies a lattice softening. They are tied together in the following equation $v_\mu = \sqrt{c_\mu/\rho}$, where the corresponding elastic constants

are c_μ. In the same way, sound attenuation coefficients are

$$\begin{aligned} \alpha_\mu(\boldsymbol{q}) &= -\lim_{\omega\to 0}\frac{1}{v_\mu^*\omega}\mathrm{Im}\delta K_\mu^R(\boldsymbol{q},\omega), \\ &= \lim_{\omega\to 0}\frac{\kappa^2\boldsymbol{q}^2}{2\rho v_\mu^*\omega}\mathrm{Im}\chi_d^R(\boldsymbol{q},\omega\to 0). \qquad (4.40) \\ &\sim \frac{\kappa^2}{2\rho v_\mu^*}\frac{1}{r^2}\frac{|\boldsymbol{q}|}{\gamma_d}, \qquad (4.41) \end{aligned}$$

with $\gamma_d = \frac{2v_F}{\rho_0}$. Thus $\alpha_\nu(\boldsymbol{q}) \propto r^{-2}$. The symmetry-allowed coupling term leads to the isotropic divergence of transverse (longitudinal) sound attenuation $\alpha_{T(L)} \propto (T_c - T)^{-2}$ and an isotropic lattice softening.

In addition to the above equation, there is another relevant term[134, 275] which is induced by the deformation potential,

$$F'_{\mathrm{nem-ph}}[\boldsymbol{\Phi},\boldsymbol{u}] = \kappa'\sum_{\boldsymbol{q},\boldsymbol{q}'}\Phi_a^*(\boldsymbol{q}+\boldsymbol{q}')\Phi_a(\boldsymbol{q}')[i|\boldsymbol{q}|u_L(\boldsymbol{q})], \qquad (4.42)$$

where the longitudinal sound modes couple to the quadratic term of nematic fields. It originates from a change in volume due to the effective nematic-nematic interaction. This term also leads to the divergent contribution to the longitudinal sound attenuation $\alpha_L \propto (T_c - T)^{-2}$. Note that the latter term is essentially the same as in weak ferromagnetism[275] for sound attenuation near the ferromagnetic transition in metals. [3]

Comparison with the Ising nematic case

Some comments are in order here on the comparison with the Ising nematic case. In the case of the Ising nematicity, the nematic director is forced to be $\theta = \{0, \pi/2\}$. Even if we treat the two angles equally, the anisotropy of the nemato-elastic coupling remains, as follows

$$S_{\mathrm{Ising}}[\Phi,\boldsymbol{u}] = -\kappa\sum_q i|\boldsymbol{q}|\left[\tilde{u}_L(q)\cos(2\theta_{\boldsymbol{q}}) - \tilde{u}_T(q)\sin(2\theta_{\boldsymbol{q}})\right]\Phi^*(q). \qquad (4.44)$$

As pointed out in previous studies, this leads to the angle dependent damping properties of acoustic phonons[134] or the mass term anisotropy of the Ising nematic fluctuation[135].

We conclude that the unique properties to observe the three-state Potts nematic order: (i) the nematic fluctuation affects the transverse acoustic phonon, (ii) the ultrasound attenuation coefficients show an isotropic divergence which is proportional to the momentum $|\boldsymbol{q}|$ and (iii) the sound velocity renormalization also shows an isotropic angle

[3] Paulson and Schrieffer considered that the deformation potential of the effective exchange interaction J gives an interaction between a phonon and the electron spins of the form

$$H_{\mathrm{el-spin}}[\boldsymbol{M},\boldsymbol{u}] = -J\int_V \boldsymbol{\nabla}\cdot\boldsymbol{u}(\boldsymbol{r})\,\boldsymbol{M}(\boldsymbol{r})\cdot\boldsymbol{M}(\boldsymbol{r}), \qquad (4.43)$$

where $\boldsymbol{M}(\boldsymbol{r}) = \psi^\dagger(\boldsymbol{r})\sigma\psi(\boldsymbol{r})$ is the electron spin density. They pointed out that $\alpha_L \propto \omega^2(T - T_c)^{-2\gamma}$ above T_c.

dependence. We therefore propose to detect the three-state Potts nematic order by the measurement of the isotropic divergence of transverse sound attenuation coefficient and the isotropic sound velocity renormalization. The isotropic nature of these properties is in contrast to the Ising nematic case where such quantities are anisotropic and subject to selection rules[134]. Note that the vanishing anisotropy of the acoustic phonon velocity is consistent with Cowley's classification[276].

4.3 Model calculation of the electron-nematic phase transition

Let us move on to the model calculation of the nematic phase originating from a bond order on the honeycomb lattice. In this section, we use the mean-field approximation by taking into account the higher order terms up to the sixth order coefficients in Eq. (4.1). Since the critical properties near the phase transition are evaluated in the mean-field approximation, the power of divergence may be changed in the presence of strong fluctuations, but the stability and the extent of the ordered phase are expected to remain qualitatively unchanged even with the inclusion of such effects of the mode coupling.

4.3.1 Extended Hubbard model on the honeycomb lattice

We here consider the extended Hubbard model on the emergent honeycomb lattice in Eq. (4.45). In a TBG, a slight mismatch in the lattice periods of two graphene layers gives rise to a long-period moiré interference pattern. The regions that locally apear to be AB-stacked bilayer grahene and BA-stacked bilayer graphene form the emergent honeycomb lattice in Fig.4.1(a). Furthermore, it is pointed out that the Wannier state[154, 155, 157] is centered at the AB or BA spot in the moiré pattern, while the maximum amplitude is at three AA spots. Because of the three-peak form of Wannier state, the Coulomb interaction between the neighboring sites is as important as the on-site interaction[155]. The extended Hubbard model on the emergent honeycomb lattice reads

Extended Hubbard model

$$
\begin{aligned}
H &= \frac{1}{N}\sum_{\boldsymbol{k}\xi\sigma}\begin{pmatrix} c^{AB\dagger}_{\boldsymbol{k}\xi\sigma} & c^{BA\dagger}_{\boldsymbol{k}\xi\sigma}\end{pmatrix}\hat{\mathcal{H}}^{\xi}_{\boldsymbol{k}\sigma}\begin{pmatrix} c^{AB}_{\boldsymbol{k}\xi\sigma} \\ c^{BA}_{\boldsymbol{k}\xi\sigma}\end{pmatrix} + H_{\mathrm{int}} + H_{\mathrm{imp}}, \\
H_{\mathrm{int}} &= \frac{1}{2}\sum_{ab}\sum_{\sigma\sigma'} V_{ab} c^{\dagger}_{a\sigma} c_{a\sigma} c^{\dagger}_{b\sigma'} c_{b\sigma'},
\end{aligned}
\tag{4.45}
$$

with creation and annihilation operators $c^{\alpha\dagger}_{\boldsymbol{k}\xi\sigma}, c^{\alpha}_{\boldsymbol{k}\xi\sigma}$, the spin index σ, the sublattice index $\alpha \in \{\mathrm{AB}, \mathrm{BA}\}$, the valley index $\xi \in \{+, -\}$, the unit cell index i, and its shorthand notation $a = (i, \alpha, \xi)$.

The long-range interaction comes from the three-peak structure of Wannier orbitals in MA-TBG[154, 155, 157]. Here $\mathcal{H}^{\xi}_{\boldsymbol{k}\sigma}$ is a 2×2 Hamiltonian for each valley ξ and σ. Since our mean-field analysis aims at showing the critical properties of the nematic fluctuation and order of the metallic phase, we use a reduced tight-binding model with only the nearest-neighbor hopping term on the honeycomb lattice and deal with all spin

and valley degrees of freedom on an equal footing[4]. The tight-binding model on the honeycomb lattice are written as

$$\hat{\mathcal{H}}_k = \begin{pmatrix} 0 & t(1+e^{-i\boldsymbol{k}\cdot\boldsymbol{a}_1}+e^{-i\boldsymbol{k}\cdot\boldsymbol{a}_2}) \\ t(1+e^{i\boldsymbol{k}\cdot\boldsymbol{a}_1}+e^{i\boldsymbol{k}\cdot\boldsymbol{a}_2}) & 0 \end{pmatrix}, \tag{4.46}$$

with the nearest-neighbor hopping strength t and the primitive lattice vectors on the honeycomb lattice: $\boldsymbol{a}_1$, $\boldsymbol{a}_2$ in Fig.4.1(a). Although the band structure is somewhat different from the Bistritzer-MacDonald model and other tight-binding models[152–158], our simple model captures the essential properties around VH filling, including the correlated insulating phase near half-filling. Imposing valley-U(1) symmetry, we introduce two orbitals which do not hybridize with each other. Each valley for $\xi = \pm 1$ is independent in the non-interacting Hamiltonian. Although the Coulomb interaction term may have both contributions from the intra-valley and the inter-valley interaction, the obtained form factor from the DW-equation method[174] has no inter-valley component. In our mean-field calculation, we analyze all spin and valley degrees of freedom on an equal footing in the following section. As is known, in order to reproduce the correlated insulating phase near VH filling[5], which is not expected in ordinary single layer graphene, valley degrees of freedom are needed. In this paper, however, we focus on the nematic metallic phase with the C_3-breaking Fermi surface, in line with the transport measurement in Ref. [167].

The third term H_{imp} in Eq. (4.45) represents the spin-independent short-range isotropic impurity scattering,

$$H_{\mathrm{imp}} = \sum_{\xi\sigma\alpha i} u_i^{\mathrm{imp}\xi\sigma\alpha} n_i^{\xi\sigma\alpha}, \tag{4.47}$$

where the random impurity potential u^{imp} obeys the Gaussian ensemble

$$\langle u_i^{\mathrm{imp}} \rangle = 0, \ \langle u_i^{\mathrm{imp}} u_j^{\mathrm{imp}} \rangle = n_{\mathrm{imp}} |u|^2 \delta_{i,j} \tag{4.48}$$

with n_{imp} and u being the impurity concentration and the strength of the impurity potential. We resort to the Born approximation, which results in the impurity-averaged self-energy

$$\hat{\Sigma}_{\mathrm{imp}}^{\xi\sigma\alpha}(i\omega_n) = n_i |u|^2 \frac{T}{N} \sum_{\boldsymbol{k}} \hat{G}(\boldsymbol{k}, i\omega_n) = i\Gamma \mathrm{sign}(\omega_n) \mathbb{1}, \tag{4.49}$$

where $i\omega_n$ is the Matsubara frequency and Γ is the strength of the impurity scattering. In this calculation, we use Eq. (4.49) or its retarded representation. With this approximation, the impurity-averaged Green's function is solved as $\hat{G}^{-1}(k) = \hat{G}_0^{-1}(k) - \hat{\Sigma}_{\mathrm{imp}}(k)$.

Derivation of forward-scattering interaction

Now we focus on the electron-nematic phase transition near the van-Hove (VH) filling where the nematicity can be seen in the experiment, as claimed in a previous theoretical

[4]The valley degrees of freedom in some moiré materials are not the same as those used in semiconductors but a kind of orbital degree of freedom due to the folding of Brillouin zone and originating from the K and K' valleys of graphene before twisting. It has also been pointed out that these two orbitals do not hybridize, because the hybridization of original K and K' points requires a large momentum transfer which greatly exceeds the scale of the moiré Brillouin zone after the folding. In the Bistritzer-MacDonald model or some effective tight-binding models, it has been pointed out that the two orbital degrees of freedom decouple from each other, referred to as a valley-$U(1)$ symmetry.

[5]In many theoretical studies, it has been pointed out that one of the essential features to explain the correlated insulating phase is the emergence of additional degrees of freedom arising from the moiré structure, namely valley degrees of freedom, compared to the case of single-layer graphene.

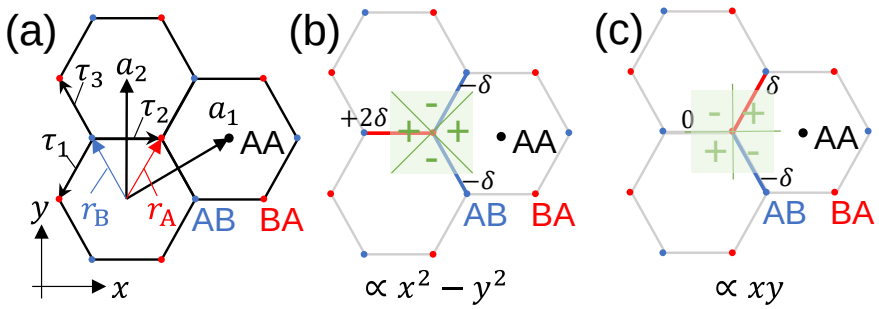

Fig. 4.1: (a) The primitive lattice vectors on the honeycomb lattice: $\boldsymbol{a}_1 = (\frac{\sqrt{3}}{2}, \frac{1}{2})$, $\boldsymbol{a}_2 = (0,1)$ with vectors of the nearest-neighbor bond $\boldsymbol{\tau}_1 = (-\frac{1}{2\sqrt{3}}, -\frac{1}{2}), \boldsymbol{\tau}_2 = (\frac{1}{\sqrt{3}}, 0), \boldsymbol{\tau}_3 = (-\frac{1}{2\sqrt{3}}, \frac{1}{2})$. The basis function of E(or E_g) representation of form factor: (b) $\mathrm{d}_{x^2-y^2}$-wave, (c) d_{xy}-wave. Reprinted figure with premission from [277] Copyright 2022 by the American Physical Society.

study[174]. These authors showed that the C_3-breaking bond ordered state is stabilized near VH filling by using the so-called DW equation method beyond our mean-field description. Based on this work[174], we restrict ourselves to the d-wave forward scattering channel of electron-electron interactions only. Here, we derive the forward-scattering interaction[6][278–282] from an extended Hubbard model on the emergent honeycomb lattice in Eq. (4.45). The microscopic forward-scattering interaction obtained is

Forward-scattering channel

$$H_{\mathrm{int}} = -g \sum_{\xi\sigma} \sum_{i=1,2} \sum_{\boldsymbol{q}} \left(n_{E_i}^{AB\xi\sigma}(\boldsymbol{q}) n_{E_i}^{BA\xi\sigma}(-\boldsymbol{q}) \right), \tag{4.50}$$

with creation and annihilation operators $c^{\alpha\dagger}_{\boldsymbol{k}\xi\sigma}, c^{\alpha}_{\boldsymbol{k}\xi\sigma}$, the spin index σ, the sublattice index $\alpha \in \{\mathrm{AB}, \mathrm{BA}\}$, the valley index $\xi \in \{+,-\}$, and the coupling constant $g = \frac{2V_{\mathrm{NN}}}{3}$ (V_{NN}: the nearest-neighbor repulsive interaction).

This is derived in the following way. The interaction term is shown in terms of the d_i-wave density operator $n_{E_i}^{AB\xi\sigma}(\boldsymbol{q}) = \frac{1}{N}\sum_{\boldsymbol{k}} E_{\boldsymbol{k}}^{i*} c^{AB\xi\dagger}_{\boldsymbol{k}+\boldsymbol{q}/2\sigma} c^{BA\xi}_{\boldsymbol{k}-\boldsymbol{q}/2\sigma}$, where $E_{\boldsymbol{k}}^{i*}$ are form factors in a two-dimensional E representation. Considering the nearest-neighbor (NN) direct channel on the multi-orbital Hubbard model, the interaction term is given by

$$H_{\mathrm{int}} = \frac{1}{2}\sum_{ab}\sum_{\sigma\sigma'} V_{ab} c^{\dagger}_{a\sigma} c_{a\sigma} c^{\dagger}_{b\sigma'} c_{b\sigma'}, \tag{4.51}$$

$$= \frac{V_{\mathrm{NN}}}{2N} \sum_{\alpha\neq\beta} \sum_{\boldsymbol{q}} \gamma^{\mathrm{NN}}_{\alpha\beta}(\boldsymbol{q}) \rho_{\alpha}(\boldsymbol{q}) \rho_{\beta}(-\boldsymbol{q}), \tag{4.52}$$

$$\gamma^{\mathrm{NN}}_{\mathrm{AB,BA}}(\boldsymbol{q}) = \left(e^{-i\boldsymbol{q}\cdot\boldsymbol{\tau}_1} + e^{-i\boldsymbol{q}\cdot\boldsymbol{\tau}_2} + e^{-i\boldsymbol{q}\cdot\boldsymbol{\tau}_3} \right), \tag{4.53}$$

[6]The forward-scattering interaction means a scattering channel between quasiparticles whose initial and final momenta are unchanged. So-called d-wave Pomeranchuk instability or bond ordered states are driven by the forward scattering channel.

where $a = (i, \alpha, \xi)$ denotes the unit cell index i, the sublattice index $\alpha \in \{\mathrm{AB}, \mathrm{BA}\}$, the valley index $\xi \in \{+, -\}$ and the density operator $\rho_\alpha(\boldsymbol{q}) = \sum_{\alpha,\xi,\sigma} \sum_{\boldsymbol{k}} c^{\alpha\xi\dagger}_{\boldsymbol{k}+\boldsymbol{q}\sigma} c^{\alpha\xi}_{\boldsymbol{k}\sigma}$.

We change the ordering of fermion operators in the NN direct channel as

$$\begin{aligned} & \sum_{\boldsymbol{p}_1\boldsymbol{p}_2\boldsymbol{p}_3} \gamma^{\mathrm{NN}}_{\mathrm{AB,BA}}(\boldsymbol{p}_2) c^{\alpha\xi\dagger}_{\boldsymbol{p}_1+\boldsymbol{p}_2\sigma} c^{\alpha\xi}_{\boldsymbol{p}_1\sigma} c^{\beta\xi'\dagger}_{\boldsymbol{p}_3-\boldsymbol{p}_2\sigma'} c^{\beta\xi'}_{\boldsymbol{p}_3\sigma'} \\ \sim & -\sum_{\boldsymbol{k}\boldsymbol{k}'\boldsymbol{q}} \gamma^{\mathrm{NN}}_{\mathrm{AB,BA}}(\boldsymbol{k}-\boldsymbol{k}') c^{\alpha\xi\dagger}_{\boldsymbol{k}+\boldsymbol{q}/2\sigma} c^{\beta\xi}_{\boldsymbol{k}-\boldsymbol{q}/2\sigma'} c^{\beta\xi\dagger}_{\boldsymbol{k}'-\boldsymbol{q}/2\sigma} c^{\alpha\xi}_{\boldsymbol{k}'+\boldsymbol{q}/2\sigma'}, \end{aligned} \tag{4.54}$$

where we have ignored the inter-valley component and consider only $\sigma = \sigma'$. Now we decouple $\gamma^{\mathrm{NN}}_{\mathrm{AB,BA}}(\boldsymbol{k}-\boldsymbol{k}')$ as $\gamma^{\mathrm{NN}}_{\mathrm{AB,BA}}(\boldsymbol{k}-\boldsymbol{k}') = \frac{1}{3} s^*_{\boldsymbol{k}} s_{\boldsymbol{k}'} + \frac{2}{3} E^{1*}_{\boldsymbol{k}} E^1_{\boldsymbol{k}'} + \frac{2}{3} E^{2*}_{\boldsymbol{k}} E^2_{\boldsymbol{k}'}$, where $s_{\boldsymbol{k}}$, $E^1_{\boldsymbol{k}}$, $E^2_{\boldsymbol{k}}$ are the form factors in Fig.4.1(b) and (c), such as

$$\begin{aligned} s_{\boldsymbol{k}} &= e^{i\boldsymbol{k}\cdot\boldsymbol{\tau}_1} + e^{i\boldsymbol{k}\cdot\boldsymbol{\tau}_2} + e^{i\boldsymbol{k}\cdot\boldsymbol{\tau}_3}, \\ E^1_{\boldsymbol{k}} &= e^{i\boldsymbol{k}\cdot\boldsymbol{\tau}_1} - \frac{1}{2} e^{i\boldsymbol{k}\cdot\boldsymbol{\tau}_2} - \frac{1}{2} e^{i\boldsymbol{k}\cdot\boldsymbol{\tau}_3}, \\ E^2_{\boldsymbol{k}} &= -\frac{\sqrt{3}}{2} e^{i\boldsymbol{k}\cdot\boldsymbol{\tau}_2} + \frac{\sqrt{3}}{2} e^{i\boldsymbol{k}\cdot\boldsymbol{\tau}_3}. \end{aligned} \tag{4.55}$$

We can rewrite Eq. (4.54) in terms of the density operator, which is in the E-representation of the point group D_3,

$$H^{AB}_{\mathrm{int}} = -\frac{V_{\mathrm{NN}}}{3N} \sum_{\xi\sigma} \sum_{\boldsymbol{k},\boldsymbol{k}',\boldsymbol{q}} \left(n^{AB\xi\sigma}_{E_1}(\boldsymbol{q}) [n^{AB\xi\sigma}_{E_1}(\boldsymbol{q})]^\dagger + n^{AB\xi\sigma}_{E_2}(\boldsymbol{q}) [n^{AB\xi\sigma}_{E_2}(\boldsymbol{q})]^\dagger \right),$$

with

$$n^{AB\xi\sigma}_{E_i}(\boldsymbol{q}) = \frac{1}{N} \sum_{\boldsymbol{k}} E^{i*}_{\boldsymbol{k}} c^{AB\xi\dagger}_{\boldsymbol{k}+\boldsymbol{q}/2\sigma} c^{BA\xi}_{\boldsymbol{k}-\boldsymbol{q}/2\sigma}. \tag{4.56a}$$

Finally, we have $H_{\mathrm{int}} = H^{AB}_{\mathrm{int}} + H^{BA}_{\mathrm{int}}$ as shown in Eq. (4.50).

	E	C_{3z}	C_{2y}	linear	quadratic
A_1	1	1	-1		x^2+y^2
A_2	1	1	-1		
E	2	-1	0	(x,y)	(x^2-y^2, xy)

Table 4.1: The character table of the D_3 point group.

In the D_3 point group case[155], form factors result from TABLE.4.1. The real part of $n^{AB\xi\sigma}_{E_i}(\boldsymbol{q})$ corresponds to the d-wave components of the density operator, referred to as nematic fields, whereas the imaginary part of $n^{AB\xi\sigma}_{E_i}(\boldsymbol{q})$ corresponds to the p-wave components, referred to as loop-current fields[174]. We note that, if we consider the D_6 point group case[158] which is another symmetry of MA-TBG, nematic fields appear irrespective of loop-current fields.

4.3.2 Effective action describing the three-state Potts nematic phase transition

To construct the mean-field theory, we introduce the two-component nematic order parameter field $\boldsymbol{\Phi}(q)$, with $\boldsymbol{\Phi} = (\Phi_1, \Phi_2)$ and we derive the following effective action in

Eq. (4.57) from the extended Hubbard model in Eqs.(4.45) and (4.50).The effective action is given by the two-component order parameter $\mathbf{\Phi} = (\Phi_1, \Phi_2)$,

Effective action for the three-state Potts nematicity

$$S_{\rm eff}[\mathbf{\Phi}] = \sum_{i\xi\sigma q} \frac{1}{g}\Phi_i(-q)\Phi_i(q) - {\rm Trln}\Big[\hat{M}^{\xi\sigma}_{k+\frac{q}{2},k-\frac{q}{2}}\Big], \tag{4.57}$$

$$\hat{M}^{\xi\sigma}_{k+\frac{q}{2},k-\frac{q}{2}} = ((-i\omega_n-\mu)\mathbb{1} + \hat{\mathcal{H}}^{\xi}_{\boldsymbol{k}\sigma})\delta_{k+\frac{q}{2},k-\frac{q}{2}} - \sum_i \frac{\Phi_i(-q)}{\sqrt{\beta N}} \begin{pmatrix} 0 & E^{i*}_{\boldsymbol{k}} \\ E^{i}_{\boldsymbol{k}} & 0 \end{pmatrix}, \tag{4.58}$$

with the chemical potential μ, the spin index σ, the valley index $\xi \in \{+,-\}$, $q = (\boldsymbol{q}, i\omega_n)$, $k = (\boldsymbol{k}, i\omega_m)$ and the form factor $E^i_{\boldsymbol{k}}$ in Eqs.(4.55), where we have neglected any loop-current order and only considered the $(d_{x^2-y^2}, d_{xy})$-wave components for simplicity.

First, we rewrite the grand-canonical partition function Z in the functional-integral form[267],

$$Z = \int \mathcal{D}(\bar{\boldsymbol{c}}, \boldsymbol{c}) e^{-S[\bar{\boldsymbol{c}},\boldsymbol{c}]}, \tag{4.59}$$

$$\mathcal{D}(\bar{\boldsymbol{c}}, \boldsymbol{c}) = \prod_{q\alpha\xi\sigma} d\bar{c}_{q\alpha\xi\sigma} dc_{q\alpha\xi\sigma}, \tag{4.60}$$

with the Grassmannian variables $\bar{\boldsymbol{c}}, \boldsymbol{c}$, where the action S is defined as

$$S = S_0[\bar{\boldsymbol{c}}, \boldsymbol{c}] + S_{\rm int}[\bar{\boldsymbol{c}}, \boldsymbol{c}], \tag{4.61}$$

$$= \sum_{i\xi\sigma qk}\sum_{\alpha\beta} \bar{c}^{\alpha}_{k+\frac{q}{2}\xi\sigma}\Big[((-i\omega_n-\mu)\delta_{\alpha\beta} + \hat{\mathcal{H}}^{\xi}_{\boldsymbol{k}\sigma,\alpha\beta})\delta_{q,0}\Big] c^{\beta}_{k-\frac{q}{2}\xi\sigma} - g\sum_{i\xi\sigma q} n^{AB\xi\sigma}_{E_i}(q) n^{BA\xi\sigma}_{E_i}(-q), \tag{4.62}$$

with the chemical potential μ, the shorthand notation $q = (\boldsymbol{q}, i\omega_n)$, $k = (\boldsymbol{k}, i\omega_m)$ and the d_i-wave density operator

$$n^{AB\xi\sigma}_{E_i}(q) = \frac{1}{N}\sum_k E^{i*}_{\boldsymbol{k}} \bar{c}^{AB\xi}_{k+q/2\sigma} c^{BA\xi}_{k-q/2\sigma}, \tag{4.63}$$

$$n^{BA\xi\sigma}_{E_i}(q) = \frac{1}{N}\sum_k E^{i}_{\boldsymbol{k}} \bar{c}^{BA\xi}_{k-q/2\sigma} c^{BA\xi}_{k+q/2\sigma}. \tag{4.64}$$

Next, we perform the Hubbard-Stratonovich transformation by using the two-component complex field $(\mathbf{\Psi}, \bar{\mathbf{\Psi}})$, with $\mathbf{\Psi} = (\Psi_1, \Psi_2)$, $\Psi_i \in \boldsymbol{C}$, and $\bar{\mathbf{\Psi}} = \mathbf{\Psi}^*$, as follows

$$S_{\rm int} = -\sum_{i\xi\sigma q}\frac{1}{\sqrt{\beta N}}\Big(\bar{\Psi}_i(-q) n^{AB\xi\sigma}_{E_i}(q) + \Psi_i(-q) n^{BA\xi\sigma}_{E_i}(q)\Big) + \frac{1}{g}\sum_{i\xi\sigma q}\Psi_i(-q)\bar{\Psi}_i(q),$$

$$= \sum_{i\xi\sigma qk}\sum_{\alpha\beta}\bar{c}^{\alpha}_{k+\frac{q}{2}\xi\sigma}\Big[V^i_{\alpha\beta}(k,q)\Big] c^{\beta}_{k-\frac{q}{2}\xi\sigma} + \frac{1}{g}\sum_{i\xi\sigma q}\Psi_i(-q)\bar{\Psi}_i(q), \tag{4.65}$$

where $V^i_{\alpha\beta}(k,q)$ is an (α,β) component of the matrix $\hat{V}^i(k,q)$. In terms of form factors $E^i_{\boldsymbol{k}}$ in Eq. (4.55), it is expressed,

$$\hat{V}^i(k,q) = -\frac{1}{\sqrt{\beta N}}\begin{pmatrix} 0 & E^{i*}_{\boldsymbol{k}}\bar{\Psi}_i(-q) \\ E^i_{\boldsymbol{k}}\Psi_i(-q) & 0 \end{pmatrix}, \tag{4.66}$$

with $q=(\boldsymbol{q},i\omega_n)$, $k=(\boldsymbol{k},i\omega_m)$, where σ_x,σ_y are Pauli matrices and $\bar{\boldsymbol{c}},\boldsymbol{c}$ are Grassmannian variables corresponding to creation and annihilation operators.

We now divide Ψ into nematic fields $\Phi_i(q)$ and loop-current fields $\Phi'_i(q)$, where $\Phi_i(q) = \mathrm{Re}\Psi_i(q) \in \mathbb{R}$ and $\Phi'_i(q) = \mathrm{Im}\Psi_i(q) \in \mathbb{R}$. In the following calculation, for simplicity, we only consider an electron-nematic order and in this case the matrix $\hat{V}^i(k,q)$ is written as

$$\hat{V}^i(k,q) = -\frac{\Phi_i(-q)}{\sqrt{\beta N}}\begin{pmatrix} 0 & E^{i*}_{\boldsymbol{k}} \\ E^i_{\boldsymbol{k}} & 0 \end{pmatrix}. \tag{4.67}$$

The total action in this system is given by the two-component real field $\boldsymbol{\Phi}=(\Phi_1,\Phi_2)$,

$$S_{\mathrm{tot}}[\bar{\boldsymbol{c}},\boldsymbol{c},\boldsymbol{\Phi}] = S_0[\bar{\boldsymbol{c}},\boldsymbol{c}] + S_{\mathrm{int}}[\bar{\boldsymbol{c}},\boldsymbol{c},\boldsymbol{\Phi}], \tag{4.68}$$

with

$$S_0[\bar{\boldsymbol{c}},\boldsymbol{c}] = \sum_{i\xi\sigma qk}\sum_{\alpha\beta}\bar{c}^{\alpha}_{k+\frac{q}{2}\xi\sigma}\left[\left((-i\omega_n-\mu)\delta_{\alpha\beta}+\hat{\mathcal{H}}^{\xi}_{\boldsymbol{k}\sigma,\alpha\beta}\right)\delta_{q,0}\right]c^{\beta}_{k-\frac{q}{2}\xi\sigma}. \tag{4.69}$$

After integrating out the electron degrees of freedom $\boldsymbol{c},\bar{\boldsymbol{c}}$, we have an effective action for the nematic field $\boldsymbol{\Phi}$

$$S_{\mathrm{eff}}[\boldsymbol{\Phi}] = \frac{1}{g}\sum_{i\xi\sigma q}\Phi_i(-q)\Phi_i(q) - \mathrm{Trln}\left[\hat{M}^{\xi\sigma}_{k+\frac{q}{2},k-\frac{q}{2}}\right], \tag{4.70}$$

$$\hat{M}^{\xi\sigma}_{k+\frac{q}{2},k-\frac{q}{2}} = -\hat{G}_0^{-1}\delta_{k+q/2,k-q/2} - \sum_{i=1,2}\hat{V}^i(k,q), \tag{4.71}$$

where we have introduced the non-interacting Green's function $\hat{G}_0^{-1}(k) = i\omega_n\mathbb{1} - \hat{\mathcal{H}}^{\xi}_{\boldsymbol{k}\sigma}$. This leads to Eq. (4.57).

4.3.3 Ginzburg-Landau expansion for the three-state Potts nematicity

In terms of the order parameter field $\boldsymbol{\Phi}$, the partition function is expressed in a functional integral form,

$$Z = Z_0\int\mathcal{D}\boldsymbol{\Phi}e^{-S_{\mathrm{eff}}[\boldsymbol{\Phi}]}, \tag{4.72}$$

$$\mathcal{D}\boldsymbol{\Phi} = \prod_{q\alpha\xi\sigma}\frac{d\Phi_{1q\alpha\xi\sigma}d\Phi_{2q\alpha\xi\sigma}}{\pi}, \tag{4.73}$$

with $Z_0 = \int\mathcal{D}(\bar{\boldsymbol{c}},\boldsymbol{c})e^{-S_0[\bar{\boldsymbol{c}},\boldsymbol{c}]} = e^{-\beta\Omega_0}$, the thermodynamic potential Ω_0. The Landau free energy is given by

$$\exp\left(-F_{\mathrm{nem}}/T\right) = \int\mathcal{D}\boldsymbol{\Phi}e^{-S_{\mathrm{eff}}[\boldsymbol{\Phi}]}. \tag{4.74}$$

In terms of the order parameter field $\mathbf{\Phi}$, the Landau free energy is obtained from the GL expansion up to the sixth order terms, as follows

Ginzburg-Landau expansion

$$\begin{aligned} F_{\rm nem}[\mathbf{\Phi}_0] &= \frac{1}{2}r\Phi_+\Phi_- + \frac{1}{6}u_3(\Phi_+^3+\Phi_-^3) + \frac{1}{4}u_4(\Phi_+\Phi_-)^2 \\ &+ \frac{1}{10}u_5(\Phi_+^4\Phi_- + \Phi_+\Phi_-^4) + \frac{1}{6}u_6\Phi_+^3\Phi_-^3, \end{aligned} \tag{4.75}$$

with $\Phi_\pm = \Phi_1(0) \pm i\Phi_2(0)$, the uniform ($\boldsymbol{q} = \mathbf{0}$) and static ($i\omega_n = 0$) component $\mathbf{\Phi}_0 = \mathbf{\Phi}(q=0)$, and coefficients u_n and $r = 1/g - u_2$ defined as

$$u_{n+1} = \frac{T}{N}\sum_{k,i\omega_n} \mathrm{tr}\Big[\hat{G}_k\hat{v}^i(k,0)\Big]^{n+1}, \tag{4.76}$$

$$= \frac{1}{N}\sum_k (d_k^i)^{n+1}\frac{1}{n!}\Big[\frac{\partial^n}{\partial^n\epsilon}f(\epsilon_k^+) + (-1)^{n+1}\frac{\partial^n}{\partial^n\epsilon}f(\epsilon_k^-)\Big], \tag{4.77}$$

with the Fermi distribution function $f(\epsilon)$, where we have used the non-interacting formula in Eqs. (4.80) and (4.83) with $T\sum_{i\omega_n}[g^i(k)]^{n+1} = \frac{1}{n!}\frac{\partial^n}{\partial^n\epsilon}f(\epsilon^i)$ at the second line.

Here, we derive the GL expansion in Eq. (4.75). For simplicity, we approximate the 2×2 Dirac Hamiltonian with chiral symmetry on the honeycomb lattice,

$$\hat{\mathcal{H}}_k = \begin{pmatrix} \mu & \epsilon_k^* \\ \epsilon_k & \mu \end{pmatrix}, \tag{4.78}$$

$$\hat{U}_k = \frac{1}{\sqrt{2}}\begin{pmatrix} 1 & 1 \\ e^{i\theta_k} & -e^{i\theta_k} \end{pmatrix}, \tag{4.79}$$

where a phase factor is introduced as $\theta_k = \frac{\epsilon_k}{|\epsilon_k|}$ with $\epsilon_k = t(1+e^{-i\boldsymbol{k}\cdot\boldsymbol{a}_1} + e^{-i\boldsymbol{k}\cdot\boldsymbol{a}_2})$, the hopping parameter t and the chemical potential μ. The band representation of the non-interacting Green's function and the interaction vertex in Eq. (4.71) is given by

$$\hat{G}_0(k) = \hat{U}_k\begin{pmatrix} g_k^+ & 0 \\ 0 & g_k^- \end{pmatrix}\hat{U}_k^\dagger, \tag{4.80}$$

$$\begin{aligned} \hat{V}^i(k,q) &= -\frac{1}{\sqrt{\beta N}}\hat{U}_k\Big\{\begin{pmatrix} 1 & 0 \\ 0 & -1 \end{pmatrix}\Big[d_k^i\Phi_i(-q) - p_k^i\Phi_i'(-q)\Big] \\ &+ \begin{pmatrix} 0 & -i \\ i & 0 \end{pmatrix}\Big[-p_k^i\Phi_i(-q) + d_k^i\Phi_i'(-q)\Big]\Big\}\hat{U}_k^\dagger, \end{aligned} \tag{4.81}$$

where $[g_k^\pm]^{-1} = i\omega_n \mp |\epsilon_k| - \mu$ is the electron Green's function, ω_n is the fermion Matsubara frequency and we have introduced the d- and p- wave components of the form factor E_k^i in Eqs.(4.55),

$$d_k^i = \mathrm{Re}\Big[E_k^i e^{-i\theta_k}\Big],\ p_k^i = \mathrm{Im}\Big[E_k^i e^{-i\theta_k}\Big]. \tag{4.82}$$

If the system has space inversion symmetry, the p-wave component of the nematic field vanishes. Now we focus on the d-wave component, for which the matrix $\hat{V}^i(k,q)$ is

obtained in a diagonal form

$$\begin{aligned}\hat{V}^i(k,q) &= -\frac{d^i_{\boldsymbol{k}}\Phi_i(-q)}{\sqrt{\beta N}}\hat{U}_{\boldsymbol{k}}\begin{pmatrix}1 & 0\\ 0 & -1\end{pmatrix}\hat{U}^\dagger_{\boldsymbol{k}},\\ &= \hat{v}^i(k,q)\Phi_i(-q),\end{aligned} \tag{4.83}$$

where we have introduced the shorthand notation of the interaction vertex $\hat{v}^i(k,q)$.

As described in Sec. 4.3.2, we have used the effective action in Eq. (4.71). In terms of the order parameter field $\boldsymbol{\Phi} = (\Phi_1, \Phi_2)$, the partition function is expressed in a functional integral form,

$$Z = Z_0 \int \mathcal{D}\boldsymbol{\Phi} e^{-S_{\rm GL}[\boldsymbol{\Phi}]}, \tag{4.84}$$

$$S_{\rm GL}[\boldsymbol{\Phi}] = \sum_{n=1,\cdots,6} S^{(n)}_{\rm GL}[\boldsymbol{\Phi}]. \tag{4.85}$$

We expand the above GL action up to the sixth order terms in the nematic order parameter, by using the following relation as

$$\mathrm{Trln}\hat{M} = \mathrm{Trln}\left(-\hat{G}_0^{-1}\right) - \sum_{n=1}^{\infty}\frac{1}{n}\mathrm{Tr}\left(\hat{G}_0\hat{V}\right)^n, \tag{4.86}$$

where $\hat{M}$ is shown in Eq.(4.71). The first order term of $\boldsymbol{\Phi}$ is

$$\mathrm{Tr}\left(\hat{G}_0\hat{V}\right) = \frac{1}{\sqrt{\beta N}}\sum_{ik\alpha\beta}\left[\hat{G}_k\right]_{\alpha\beta}\left[\hat{v}^i(k,q)\right]_{\beta\alpha}\Phi_i(-q), \tag{4.87}$$

where this integration becomes zero because $\hat{G}_k$ has the C_3 symmetry. The second order term, which is shown in Figs. (4.2)(a), is

$$\frac{1}{2}\mathrm{Tr}\left(\hat{G}_0\hat{V}\right)^2 = \frac{1}{2}\frac{T}{N}\sum_{qij}\chi^{ij}_q\Phi_i(-q)\Phi_j(q), \tag{4.88}$$

$$\chi^{ij}_q = \frac{T}{N}\sum_{\boldsymbol{k},i\omega_n}\mathrm{tr}\left[\hat{G}_{k+q/2}\hat{v}^i(k,q)\hat{G}_{k-q/2}\hat{v}^j(k,-q)\right]. \tag{4.89}$$

Thus the Gaussian term is

$$S^{(2)}_{\rm Gauss}[\boldsymbol{\Phi}] = \sum_{qij}\left[\chi_d^{-1}(q)\right]_{ij}\Phi_i(-q)\Phi_j(q), \tag{4.90}$$

$$\left[\chi_d^{-1}(q)\right]_{ij} = \frac{1}{g}\delta_{ij} - \chi^{ij}_q, \sim (r + \xi_0^2\boldsymbol{q}^2)\delta_{ij} + \hat{D}^{ij}_q, \tag{4.91}$$

where $g = \frac{2V_{\rm NN}}{3}$ is a coupling constant, the dynamical part of nematic fluctuation are defined as

$$\hat{D}_{\boldsymbol{q},i\omega_n} = \hat{\chi}_{\boldsymbol{q},i\omega_n} - \hat{\chi}_{\boldsymbol{q},0}, \tag{4.92}$$

where $r = 1/g - \chi^{11}_{q=0} \propto T_{c0} - T$ measures the distance from the mean-field transition temperature T_{c0} and the mean-field correlation length is ξ_0.

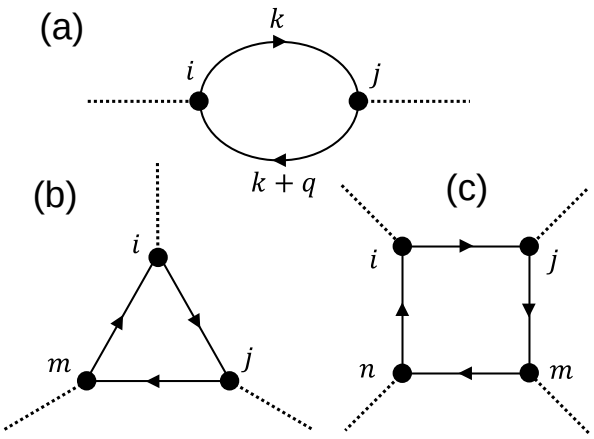

Fig. 4.2: Diagramatic representation of GL coefficients for the second order term (a), the third order term (b), and the fourth order term (c). The solid line means the electron Green's function and the broken line means the nematic interaction. The black circle means the vertex v and its labels i, j, m, n.

In a similar way, we evaluate the coefficients up to the sixth order and it is graphically shown in Figs. (4.2). GL coefficients u_{n+1} comes from uniform contributions of the $(n+1)$-th order term in the non-interacting Dirac dispersion,

$$u_{n+1} = \frac{T}{N}\sum_{k,i\omega_n} \mathrm{tr}\Big[\hat{G}_k \hat{v}^i(k,0)\Big]^{n+1}, \tag{4.93}$$

$$= \frac{1}{N}\sum_{k}(d^i_k)^{n+1}\frac{1}{n!}\Big[\frac{\partial^n}{\partial^n \epsilon} f(\epsilon^+_k) + (-1)^{n+1}\frac{\partial^n}{\partial^n \epsilon} f(\epsilon^-_k)\Big]. \tag{4.94}$$

where we have used the non-interacting formula in Eqs. (4.80) and (4.83) with

$$T\sum_{i\omega_n}[g^i(k)]^{n+1} = \frac{1}{n!}\frac{\partial^n}{\partial^n \epsilon} f(\epsilon^i), \tag{4.95}$$

at the second line. If we treat the impurity effect in a Born approximation, the electron Green's function is evaluated as $\hat{G}^{-1}(k) = \hat{G}_0^{-1}(k) - \hat{\Sigma}_{\mathrm{imp}}(k)$ and the self-energy is obtained in Eq. (4.49).

As a consequence, we arrive at the following GL action up to the sixth order,

$$S_{\mathrm{GL}}[\Phi_\pm(\boldsymbol{q}=0, i\omega_n=0)] = (\beta N)\Big[\frac{1}{2}r\Phi_+\Phi_- + \frac{1}{6}u_3(\Phi_+^3+\Phi_-^3) + \frac{1}{4}u_4\Phi_+^2\Phi_-^2 + \frac{1}{10}u_5(\Phi_+^4\Phi_- + \Phi_+\Phi_-^4) + \frac{1}{6}u_6\Phi_+^3\Phi_-^3\Big], \tag{4.96}$$

where $x = (\boldsymbol{r}, \tau)$,$\Phi_\pm = \Phi_1 \pm i\Phi_2$ and $r = 1/g - u_2$. The Landau free energy is obtained from $\exp(-F_{\mathrm{nem}}/T) = \int \mathcal{D}\boldsymbol{\Phi} e^{-S_{\mathrm{eff}}[\boldsymbol{\Phi}]} = e^{-S_{\mathrm{eff}}[\Phi_\pm(0)]}$ as shown in Eq. (4.75).

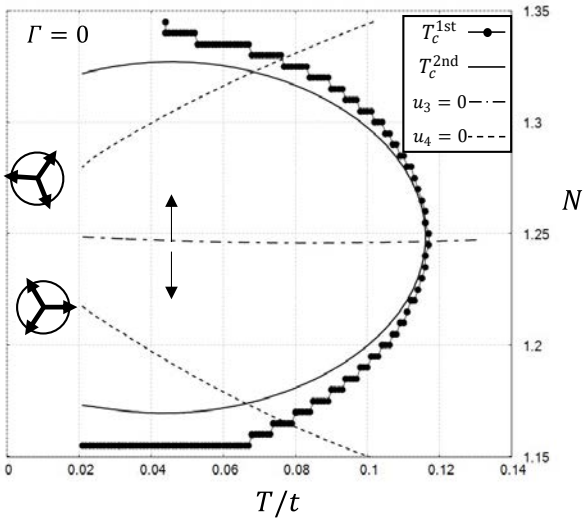

Fig. 4.3: Phase diagram of a nematic bond-ordered state. We use $V_{\mathrm{NN}}/t = 4.5$. $T_c^{1\mathrm{st}}$ ($T_c^{2\mathrm{nd}}$) is the first (second) order phase transition point, and $u_3 = 0$ ($u_4 = 0$) is zeros of u_3 (u_4). The three arrowheads surrounded by the circle represent the set of the orientation of the nematic director. The set of the orientation changes on the zeros of u_3. We calculate this by using a square mesh of 500×500 in the Brillouin zone. The phase transition line $T_c^{1\mathrm{st}}$ is defined by $F_{\mathrm{nem}}[\Phi_1, \Phi_2] = 0$ and $\partial F_{\mathrm{nem}}[\Phi_1, \Phi_2]/\partial\Phi_i = 0$ with $i = 1, 2$. Reprinted figure with premission from [277] Copyright 2022 by the American Physical Society.

4.3.4 Numerical results (i): Mean-field phase diagram

Parameters in the Landau free energy

Now we determine Landau free energy coefficients up to the sixth order $(r, u_2, \cdots, u_6)$ numerically. [7] The electron-nematic phase transition shown here is described by a spontaneous distortion of the Fermi surface, caused by C_3-breaking hopping anisotropy. In addition, due to the symmetry of spin and valley, we perform a mean-field analysis dealing with all spin and valley degrees of freedom on an equal footing. In the following section, without loss of generality, we focus on one spin and one valley degrees of freedom. We summarize the mean-field phase diagram (T, N), with the temperature T and the filling N, determined by the Landau free energy in Fig. 4.3. The transition is of purely second order at the VH filling ($N_{\mathrm{VH}} \sim 1.25$) because of $u_3 = 0$ and $u_4 > 0$. We note that $N = 2$ corresponds to the full filling and $N = 1$ corresponds to the charge-neutral point. The important feature is that the transition is of weak first-order in a wide range of filling. "Weak first-order" means that the character of the phase transition is first order but the transition temperature is close to the second order transition temperature which is defined by $u_2 = 0$. In general, first-order transitions are not accompanied by a divergence of the susceptibility, but a remnant of critical fluctuations can nevertheless be observed due to the vicinity of the second order instability, as we will show below.

In this analysis, we focus around VH filling as shown in Figs.4.4(a) (this is correspond

[7] In this calculation, we use the band representation of the non-interacting Green's function. The (α, β)-component is expressed as $\left[\mathcal{G}_k\right]_{\alpha\beta} = \sum_\gamma \left[U_k\right]_{\alpha\gamma} \left[U_k^\dagger\right]_{\gamma\beta} g^{fl}_{k,i!_m}$, where the non-interacting Hamiltonian $\mathcal{H}_k$ and the unitary matrix U_k as follows: $\mathcal{H}_k U_k = U_k D_k$, a diagonal matrix $D_k = \mathrm{diag}\{\epsilon_k^\gamma\}$, γ-th component of eigenvalue ϵ_k^γ and $1/g^\gamma_{k,i\omega_m} = i\omega_m - \epsilon_k^\gamma$.

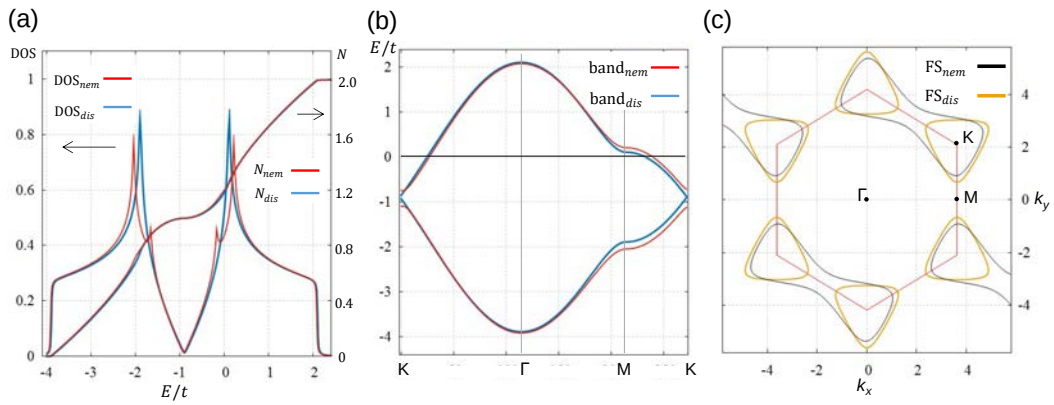

Fig. 4.4: The Hartree-Fock results in the disordered phase and the nematic phase; (a)The density of states, and the particle number N. (b)The band structure along the high-symmetric line of the Brillouin zone. (c)The Fermi surface. The data are plotted for the disordered phase ($\boldsymbol{\Psi} = (0,0)$, $T/t = 0.15$) and the nematic phase ($\boldsymbol{\Psi} = (0.12,0)$, $T/t = 0.05$). We use $V_{\mathrm{NN}}/t = 4.5$, $N = 1.2$. We note that $N = 2$ corresponds to the full filling and $N = 1$ corresponds to the charge-neutral point. Reprinted figure with premission from [277] Copyright 2022 by the American Physical Society.

to $N = 1.2$). We note the band structure in Figs.4.4(b). Introducing on the interaction, a finite value of the order parameter yields a deformation of the Fermi surface which breaks the C_{3z} symmetry as shown in Figs.4.4(c). This is obtained from Hartree-Fock approximation and the derivation is summarized in Appendix 4.6.1. We show the temperature dependence of the order parameters in Fig. 4.5. Although, in the vicinity of VH filling, the transition is of almost second order with a continuous change of the order parameter in Fig. 4.5(a), for other fillings, the transition is of weak first-order with a small discontinuous change of the order parameter in Fig. 4.5(b). In this weak first-order region, we expect a nearly diverging behavior of the nematic susceptibility.

Impurity effects for the mean-field phase diagram

Next, we show how weak impurity scattering modifies the mean-field phase diagram. In graphene-based materials, it is known that there are impurity effects due to the substrate and disorder effects due to sample inhomogeneity. Here, for simplicity, we treat the impurity effect at the level of the Born approximation introduced in Eq. (4.49). In Fig. 4.6, the mean-field phase diagrams for disordered cases ($\Gamma = 0.05$ and $\Gamma = 0.09$) are shown. First, we observe that the transition temperature of the three-state Potts nematic state is suppressed with increasing the impurity scattering. Second, the first order transition line at low temperatures gradually approaches the second-order one, rendering the transition a weak first-order. Thus we conclude that the transition becomes weakly first-order in the presence of the weak impurity scattering.

As described above, we have used the mean-field approximation for the free energy and the critical properties. In general, it is known that phase transitions and critical properties can be modified by introducing mode-coupling effects between fluctuations, such as third- and fourth-order terms of GL action. In addition, due to the peculiarities of the three-state Potts model, the classical phase transition at finite temperature is known to be a second-order transition in two spatial dimensions[283, 284], and it is expected that the first-order transition discussed here will be further close to the second-order transition if

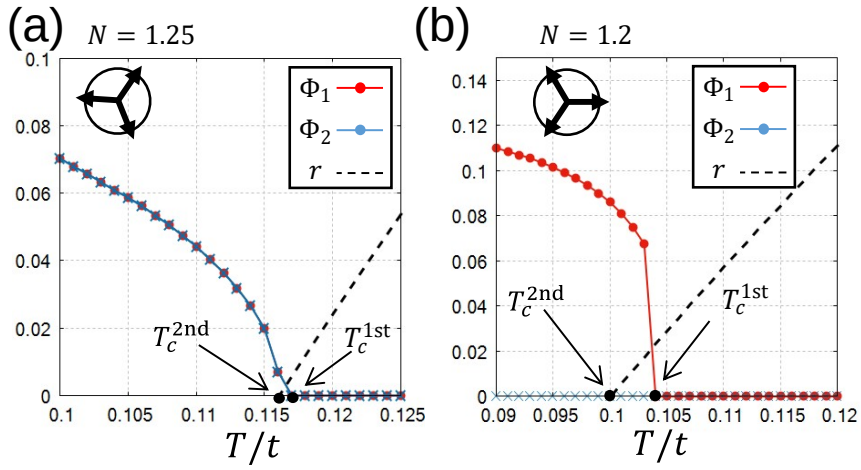

Fig. 4.5: Nematic order parameters (Φ_1, Φ_2) and $r \propto T_{c0} - T$ measures the distance from the mean-field transition temperature T_c^{2nd}. The three arrowheads surrounded by the circle represent the set of the orientation of the nematic director. T_c^{1st} (T_c^{2nd}) is the first (second) order phase transition point. (a) $N = 1.25$ which is very close to the VHs. (b) $N = 1.2$ which clearly shows the first order phase transition. Reprinted figure with premission from [277] Copyright 2022 by the American Physical Society.

we take into account the mode-coupling effect[129, 131–133]. Of course, in the case of quantum phase transitions[285–287], the order of the phase transition is not well understood, and it is an open question what happens for the order of the phase transition when the nematic phase transition is accompanied by loop-current order or when the impurity vertex corrections are applied. In our analysis, the critical properties near the phase transition point are due to the mean-field approximation, but the stability and the extent of the ordered phase are expected to remain qualitatively unchanged even if the effects of such fluctuations are included.

Before closing this subsection, we comment on the connection between the calculation and experimental observations. In Ref. [167], the authors obtained the phase diagram by changing the filling with a gate voltage, where the electron-nematic state is realized only in a narrow filling range. This observation is consistent with the fact that the electron-nematic state is stable only near the VHs in our mean-field calculations.

4.3.5 Numerical results (ii): Sound attenuation coefficients

Next, we show the sound attenuation coefficients and the sound wave velocity for the transverse acoustic phonons, which are modified by the Fermi surface fluctuation. The inverse propagator of acoustic phonon has the following form, as we have discussed in Sec. 4.2.2,

$$K_\mu(q) = K_\mu^{(0)}(q) - \delta K_\mu(q), \tag{4.97}$$

$$K_\mu^{(0)} = \epsilon_m^2 + v_\mu^2 \boldsymbol{q}^2, \tag{4.98}$$

with $q = (\boldsymbol{q}, i\epsilon_m)$, the full (bare) inverse propagator $K_\mu(K_\mu^{(0)})$, the phonon self-energy δK_μ, the boson Matsubara frequency $\epsilon_m = 2\pi T m$ and the mass density ρ.

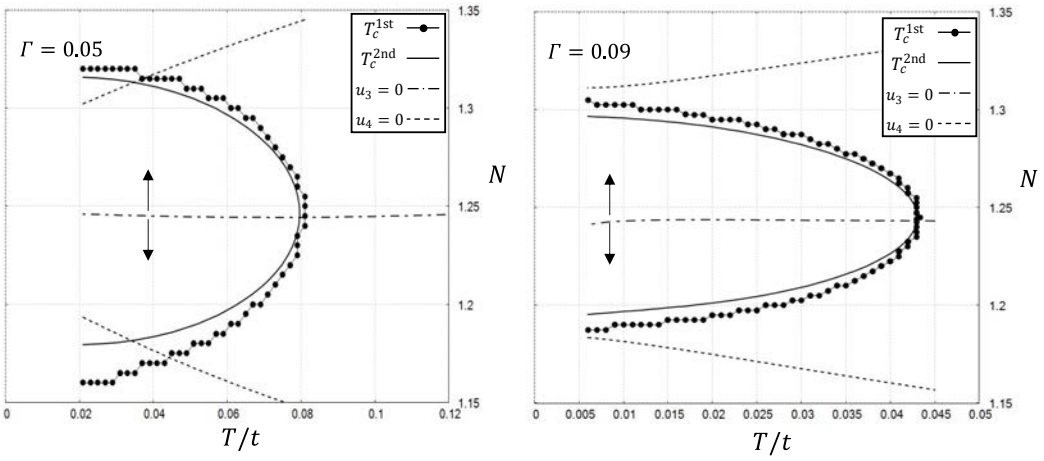

Fig. 4.6: Phase diagrams of a bond-ordered phase with the impurity scattering ($\Gamma = 0.05$ and $\Gamma = 0.09$). T_c^{1st} (T_c^{2nd}) is the first (second) order phase transition point, and $u_3 = 0$ ($u_4 = 0$) is zeros of u_3 (u_4). The calculation is done by using a square mesh of 100×100 in the Brillouin zone and a mesh of 1000 in the energy. The phase transition line T_c^{1st} is defined by $F_{\rm nem}[\Phi_1, \Phi_2] = 0$ and $\partial F_{\rm nem}[\Phi_1, \Phi_2]/\partial\Phi_i = 0$ with $i = 1, 2$. Reprinted figure with premission from [277] Copyright 2022 by the American Physical Society.

The dominant contribution to the phonon self-energy in Eq. (4.28) is given by the nematic fluctuation,

$$\delta K_{\mu,\rm nem}(q) = \frac{\kappa^2 \boldsymbol{q}^2}{2\rho}\chi_d(q) = -\frac{\kappa^2\boldsymbol{q}^2}{2\rho}\left[r + \xi_0^2\boldsymbol{q}^2 + \frac{|\epsilon_m|}{\Gamma_d(\boldsymbol{q})}\right]^{-1}. \tag{4.99}$$

An additional contribution to the phonon Green's function is given by the bubble diagrams with electron-phonon vertices,

$$\delta K_{\mu,\rm el-ph}(q) = -\frac{1}{2\rho}\int_q \mathrm{tr}\left[\hat{G}_{k+q/2}\hat{w}^{\mu}_{k,q}\hat{G}_{k-q/2}\hat{w}^{\mu}_{k,-q}\right], \tag{4.100}$$

with

$$\begin{aligned}
\hat{w}^{\mu}_{k,q} &= -\frac{g_{\rm ph}}{\sqrt{\beta N}}\begin{pmatrix} 0 & \Delta\boldsymbol{E}^*_{\boldsymbol{k},\boldsymbol{q}}\cdot\hat{\boldsymbol{e}}_\mu(-q) \\ \Delta\boldsymbol{E}_{\boldsymbol{k},\boldsymbol{q}}\cdot\hat{\boldsymbol{e}}_\mu(-q) & 0\end{pmatrix}, \\
\Delta\boldsymbol{E}_{\boldsymbol{k},\boldsymbol{q}} &= \begin{pmatrix} -\frac{1}{2} \\ -\frac{\sqrt{3}}{2}\end{pmatrix} e^{i\boldsymbol{k}\cdot\boldsymbol{a}_1}(i\boldsymbol{q}\cdot\boldsymbol{a}_1) + \begin{pmatrix} -\frac{1}{2} \\ \frac{\sqrt{3}}{2}\end{pmatrix} e^{i\boldsymbol{k}\cdot\boldsymbol{a}_2}(i\boldsymbol{q}\cdot\boldsymbol{a}_2),
\end{aligned} \tag{4.101}$$

with $\hat{\boldsymbol{e}}_T = (-\sin\theta_{\boldsymbol{q}}, \cos\theta_{\boldsymbol{q}})$ $\hat{\boldsymbol{e}}_L = (\cos\theta_{\boldsymbol{q}}, \sin\theta_{\boldsymbol{q}})$, $\theta_{\boldsymbol{q}} = \tan^{-1}(q_y/q_x)$. The derivation of the above equations is in Appendix 4.6.2. The phonon self-energy ($\delta K_{\mu,\rm el-ph}(q)$ due to the electron-phonon couplings and $\delta K_{\mu,\rm nem}(q)$ due to the nemato-elastic couplings in Eq. (4.28)) are obtained numerically. The sound velocity and the sound attenuation coefficient, which is defined as the inverse of the phonon mean-free path, are summarized as follows

$$v^*_\mu = v_\mu\sqrt{1 - \frac{\mathrm{Re}\delta K^R_\mu(\boldsymbol{q}, \omega\to 0)}{v_\mu^2 q^2}},\ \alpha_\mu(\boldsymbol{q}) = -\lim_{\omega\to 0}\frac{1}{v_\mu\omega}\mathrm{Im}K^R_\mu(\boldsymbol{q},\omega). \tag{4.102}$$

Using these self-energies δK, we calculate the normalized sound velocities $v_{\mathrm{nem}}/v_{\mathrm{el-ph}}$ and the normalized sound attenuation coefficients $\alpha_{\mathrm{nem}}/\alpha_{\mathrm{el-ph}}$, which quantify the contribution of the nematic fluctuation (v_{nem}, α_{nem}) to the electron-phonon coupling ($v_{\mathrm{el-ph}}$, $\alpha_{\mathrm{el-ph}}$). The temperature dependencies of the transverse sound velocity and the transverse sound attenuation coefficient for several impurity scatterings are shown in Fig. 4.7. The parameter region is in the weak first-order phase transition for $N = 1.2$. We note that the ratio of the sound velocity $v_{\mathrm{nem}}/v_{\mathrm{el-ph}}$ takes about 0.8 at $T_c^{1\mathrm{st}}$ for the choice of parameters.

It is confirmed that the ultrasound attenuation coefficient is enhanced by a factor of about 100 around the first-order transition temperature T_c^{1st} even if the impurity effect is present in Fig. 4.7 ($\Gamma = 0.05$). Furthermore, in the region where the impurity scattering is much stronger in Fig. 4.7 ($\Gamma = 0.09$), the ultrasound attenuation coefficient is still enhanced by a factor of 10 for the same parameters as above. These results suggest that the weak first-order phase transition occurs and that the effect of nematic fluctuations can be observed in the phonon damping even in the presence of impurities.

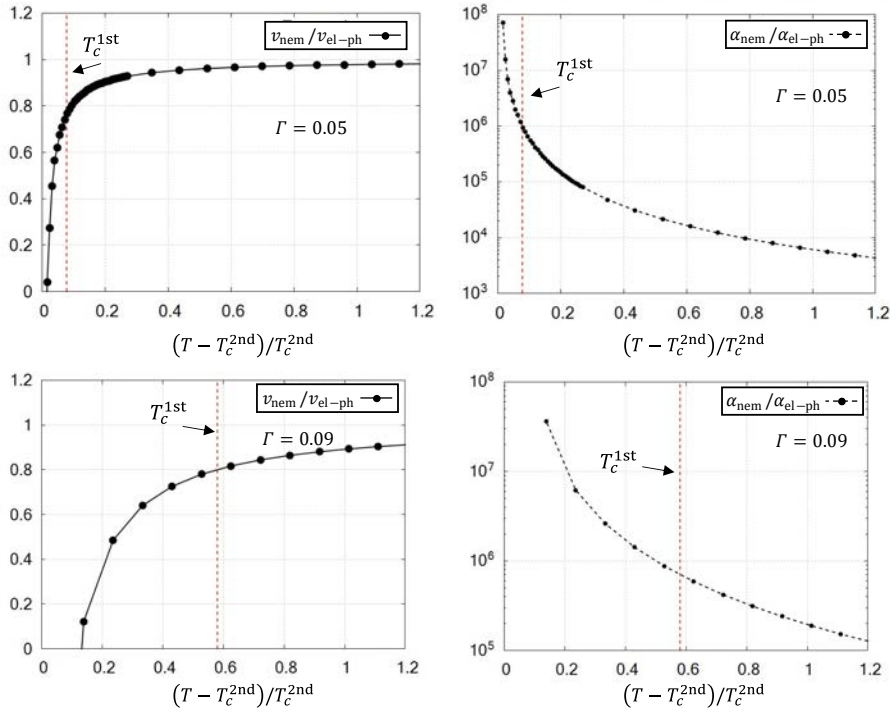

Fig. 4.7: Temperature dependence of the sound velocities $v_{\mathrm{nem}}/v_{\mathrm{ep-ph}}$ and the sound attenuation coefficients $\alpha_{\mathrm{nem}}/\alpha_{\mathrm{ep-ph}}$ for the transverse acoustic wave for $N = 1.2$. $T_c^{1\mathrm{st}}$ ($T_c^{2\mathrm{nd}}$) is the first (second) order phase transition point. The points make only sense above the transition temperature for $T > T_c^{1\mathrm{st}}$. Reprinted figure with premission from [277] Copyright 2022 by the American Physical Society.

4.4 Discussion

Here some additional comments are in order on the characteristic properties discussed in the previous sections.

Superlattice effects

In this chapter, we have focused on the long-wavelength limit of acoustic phonons with linear dispersions. Here we comment on the phonon modes in MA-TBG, which are complicated due to the superlattice structure. One of the unique properties of such moiré phonon modes, which reflects a non-rigid crystal[175, 176], is the appearance of rotation tensors in addition to the ordinary strain tensors in the elastic degrees of freedom. While for a rigid crystal the velocity of longitudinal phonons is much larger than that of transverse phonons, for twisted bilayer graphene having a non-rigid crystal property, the velocity of transverse phonons may exceed that of longitudinal phonons due to the coupling between the strain tensor and the rotation tensor[171, 175, 176]. Although there are such quantitative differences, as far as the acoustic phonons in the long-wavelength limit are concerned, there is no qualitative change in their linear-dispersion properties. Thus we believe, even in the moiré materials, that our theory can be applied to the low-energy properties of acoustic phonons with linear dispersions. It is also important to consider the effect of the rotation tensor to the nematicity as discussed in Ref. [171]. Since the electron-nematic order parameter does not couple to the rotation tensor in the leading order correction, we have not considered it in this paper. Nevertheless, the detailed study including the higher order corrections to phonons and nematicity is important, which is left for future work.

Impurity effects

In MA-TBG, it is known that there are impurity effects due to the substrate and disorder effects due to sample inhomogeneity and inhomogeneity of moiré structures. In this chapter, we have treated the disorder effect at the level of the Born approximation. In addition to the discussions in Sec. II. C and Sec. III. C, it is also important to consider several scattering mechanisms. In this connection, we comment here on the impurity effects beyond the Born approximation in Eq. (4.49). We expect that the impurity vertex correction changes the dynamical critical exponent, leading to the change of the wavenumber dependence of the ultrasound attenuation coefficients from $|\boldsymbol{q}|$ to $|\boldsymbol{q}|^2$.

The damping rate $\Gamma_d(q)$ in Eq. (4.5) depends on the dynamical critical exponent z as,

$$\Gamma_d(\boldsymbol{q}) \quad = \quad \gamma_d |\boldsymbol{q}|^{z-2} \tag{4.103}$$

where $z = 3$ for a usual ferroic order in clean systems. One of the unique properties of the electron-nematic state is that the sound attenuation coefficient in Eq. (4.41) reflects the damping rate of nematic fluctuations, as follows,

$$\alpha_\mu(\boldsymbol{q}) \quad \sim \quad \frac{\kappa^2}{2\rho v_\mu^*} \frac{1}{r^2} \frac{\boldsymbol{q}^2}{\Gamma_d(\boldsymbol{q})} = \frac{\kappa^2}{2\rho v_\mu^*} \frac{1}{r^2} \frac{|\boldsymbol{q}|^{4-z}}{\gamma_d}. \tag{4.104}$$

We discuss how the impurity effect would modify the above nematic fluctuations via a possible change in the exponent z. It is known that for charge density fluctuations, a diffusion pole appears from vertex corrections for the impurity scattering[129, 288–290] , and the dynamical critical exponent becomes $z = 4$[8]. This is related to the conservation law of electric charge, and such a diffusive mode appears when there is charge $U(1)$-gauge symmetry. On the other hand, in the present case of electric quadrupoles (the

[8] A leading order contribution from a diffusion pole has the form $D_q \propto \frac{|\epsilon_n|}{|q|^2}$ in ordinary charge density fluctuations.

electric quadrupole density is not a conserved quantity[268, 291]), it is expected that the normal diffusion mode does not appear due to impurity effects[292], and we expect the relaxation mode[293][9] with $z = 2$, etc. In this case, the dynamical critical exponent may be changed to a value other than $z = 3$, unlike the usual charge density fluctuation and this change will be probed through the wavenumber dependence of the ultrasound attenuation coefficient. To identify the correct dynamical exponent is an open problem and a further analysis will be required.

Candidate materials for experiments

Here are some comments on candidate materials. A three-state Potts nematic order has been reported for doped-Bi_2Se_3[186–188]. Even in these materials, as the 2D nematic ordered state which breaks the in-plane C_{3z}-symmetry is stacked in the z-direction, the formulation developed here can be applied to phonon modes propagating in the plane with a slight modification. In these materials, it has been suggested that a vestigial nematic order[143] is caused by nematic superconducting fluctuations, rather than the bond-order discussed here. Nevertheless, a similar treatment can be applied, and thus we expect the isotropic divergence of sound attenuation and the isotropic lattice softening for transverse modes within the GL theory discussed here. The scenario presented here is useful to probe the nematic fluctuation, predicting a weak first-order transition like behavior.

In the case of MA-TBG, an electron-nematic state has been reported at several fillings by scanning tunneling microscopy[164–166], transport measurement[167] and the quantum oscillation[167, 168]. Our mean-field analysis for the C_3-breaking bond order is based on Ref. [174]. It is shown that the C_3-breaking intra-valley bond ordered state is stabilized near the VH filling and the other magnetically ordered states are suppressed by using the so-called DW equation method including the Aslamazov-Larkin vertex correction[174]. Besides the weak-coupling approaches[162, 174], there are some theoretical proposals such as an orbital order and a vestigial nematic order in the strong coupling theory[294]. We think that our phenomenological theory can also be applied to the above scenarios with a slight modification. The detailed study on this point is left for future work.

Unfortunately, MA-TBG does not allow us to conduct usual sound attenuation experiments due to its purely 2D character, but this does not change the fact that the mean-free path $l = \alpha^{-1}$ of phonons becomes isotropically shorter. In this 2D case, experiments using optical methods such as Brillouin scattering[295] and double resonant Raman scattering[296] provide alternative probes to detect the nematic fluctuation. For these experiments, the formulation developed here can be applied with a slight modification to identify such a three-state Potts nematic state and figure out whether it is induced spontaneously or from trivial strain.

4.5 Summary

In this chapter, we have analyzed the impact of the nemato-elastic coupling on the low energy properties of phonons by a phenomenological argument and a model calculation. Phenomenological analysis has clarified that the Landau damping term becomes isotropic due to fluctuations of the C_3-breaking bond-order in the Gaussian fluctuation region, and

[9] The relaxation mode appears in a dirty ferromagnetic quantum critical point with the spin-orbit coupling.

the nemato-elastic coupling is also isotropic. As a result, we have proposed to detect the intrinsic three-state Potts nematic phase transition by measuring the ultrasound attenuation of the transverse acoustic phonon. Namely the ultrasound attenuation coefficient shows an isotropic divergence which is proportional to the momentum $|\boldsymbol{q}|$ and the sound velocity renormalization also show an isotropic angle dependence. Both features are quite contrasted to the strong anisotropy in the case of the C_4-breaking nematic case.

We have determined the phase diagram by an extended Hubbard model in a mean-field approximation to investigate the critical properties. According to the mean-field approximation, the transition temperature takes its maximum near VHs, and the large density of states favors the nematic phase transition. The order of phase transition is of weak first-order in a wide range of band filling and, with increasing the impurity scattering, the first order transition line at low temperatures gets closer to the second-order line, making the transition weakly first-order in a wider parameter region. Furthermore, it has been confirmed that the enhancement of the ultrasound attenuation coefficient can be observed in the case of a weak first-order phase transition. Even if the effect of mode coupling between the nematic fluctuations is considered, the qualitative features of the isotropic sound attenuation coefficients and the phase diagram are expected to be unchanged, but the order of the transition could be changed to the second as expected for a classical phase transition of three-state Potts nematicity in 2D.

4.6 Appendix for this chapter: Derivations of some formulas

4.6.1 Hartree-Fock approximation of a bond-order

Here, we derive the mean-field theory of the three-state Potts nematic phase transition following Ref. [282] and show the Fermi surface and DOS in Sec. 4.3.4. The effective model containing the quadrupole-quadrupole interaction is shown in Eq. (4.50) and in Appendix 4.3.1. After introducing the mean-field decoupling $n^{\alpha\beta}_{k\sigma} = n^{\alpha\beta}_{k\sigma} - \langle n^{\alpha\beta}_{k\sigma}\rangle + \langle n^{\alpha\beta}_{k\sigma}\rangle$ and ignoring the second order correction $(n^{\alpha\beta}_{k\sigma} - \langle n^{\alpha\beta}_{k\sigma}\rangle)$, we arrive at

$$\begin{aligned} H^{\mathrm{MF}}_{\mathrm{int}} &= \frac{1}{N}\sum_{k,k'}\Big[f_{k,k'}\langle n^{BA}_{k'}\rangle n^{AB}_{k} + f^{*}_{k,k'}\langle n^{AB}_{k'}\rangle n^{BA}_{k}\Big] - \frac{1}{N}\sum_{k,k'} f_{k,k'}\langle n^{BA}_{k'}\rangle\langle n^{AB}_{k}\rangle, \\ &= \sum_{k}\begin{pmatrix} c^{A\dagger}_{k} & c^{B\dagger}_{k}\end{pmatrix}\begin{pmatrix} 0 & \Delta^{AB}_{k} \\ \Delta^{BA}_{k} & 0\end{pmatrix}\begin{pmatrix} c^{A}_{k} \\ c^{B}_{k}\end{pmatrix} - \sum_{k}\Delta^{AB}_{k}\langle n^{AB}_{k}\rangle, \end{aligned} \tag{4.105}$$

with $f_{k,k'} = g(E^{1*}_{k}E^{1}_{k'} + E^{2*}_{k}E^{2}_{k'})$, a coupling constant $g = \frac{2}{3}V_{\mathrm{NN}}$, the mean-field $\Delta^{AB}_{k} = \frac{1}{N}\sum_{k'} f_{k,k'}\langle n^{BA}_{k'}\rangle$ and form factors E^{i}_{k} in Eq. (4.55). The two-component complex order parameter $(\boldsymbol{\Psi}, \bar{\boldsymbol{\Psi}})$ with $\boldsymbol{\Psi} = (\Psi_1, \Psi_2)$ contributes to the above mean-field as,

$$\begin{aligned} \Delta^{AB}_{k} &= -\frac{g}{N}\sum_{k'}\Big[E^{1*}_{k}E^{1}_{k'}\langle n^{BA}_{k'}\rangle + E^{2*}_{k}E^{2}_{k'}\langle n^{BA}_{k'}\rangle\Big], \\ &= \Big[E^{1*}_{k}\Psi_1 + E^{2*}_{k}\Psi_2\Big], \end{aligned} \tag{4.106}$$

where the order parameters are defined as $\Psi_{1(2)} = -\frac{g}{N}\sum_k E_k^{1(2)}\langle n_k^{BA}\rangle$. Moreover, the energy shift resulting from the mean-field theory is

$$\begin{aligned} -\sum_k \Delta_k^{AB}\langle n_k^{AB}\rangle &= -\sum_k \Big[E_k^{1*}\Psi_1 + E_k^{2*}\Psi_2\Big]\langle n_k^{AB}\rangle, \\ &= \frac{N}{g}\Big[\Psi_1^*\Psi_1 + \Psi_2^*\Psi_2\Big]. \end{aligned} \tag{4.107}$$

For example, for a tight-binding model on the honeycomb lattice

$$\hat{\mathcal{H}}_k^0 = \begin{pmatrix} 0 & t(1+e^{-i\boldsymbol{k}\cdot\boldsymbol{a}_1}+e^{-i\boldsymbol{k}\cdot\boldsymbol{a}_2}) \\ t(1+e^{i\boldsymbol{k}\cdot\boldsymbol{a}_1}+e^{i\boldsymbol{k}\cdot\boldsymbol{a}_2}) & 0 \end{pmatrix}, \tag{4.108}$$

the mean-field term induces the hopping anisotropy as

$$\hat{\mathcal{H}}_k^{\mathrm{MF}} = \begin{pmatrix} 0 & E_k^{1*}\Psi_1 + E_k^{2*}\Psi_2 \\ E_k^1\Psi_1^* + E_k^2\Psi_2^* & 0 \end{pmatrix}. \tag{4.109}$$

Finally, we obtain the mean-field Hamiltonian, $\hat{\mathcal{H}}_k^{\mathrm{MF}}$.

4.6.2 Electron-phonon coupling from the bond-length change

To calculate the sound attenuation coefficients and the sound wave renormalization, we derive an electron-acoustic phonon coupling for arbitrary filling of the honeycomb lattice. The electron-phonon coupling arises from the lattice modulation by phonons, which leads to a change in the nearest neighbor hopping t, the so-called bond-length change[297–299].

Here, we derive the electron-phonon coupling in Eq. (4.100) from a change in the bond length[297–299]. We assume that the electron-phonon coupling arises from the lattice modulation by phonons, which leads to a change in the nearest neighbor hopping t.

$$H_{\mathrm{el-ph}} = \sum_{\boldsymbol{\delta}} \boldsymbol{g}(\boldsymbol{\delta}) \sum_{\boldsymbol{r}_i,\xi\sigma} \Big[\boldsymbol{u}_\alpha(\boldsymbol{r}_i) - \boldsymbol{u}_\beta(\boldsymbol{r}_i+\boldsymbol{\delta})\Big] \sum_\alpha c_{\xi\sigma}^{\alpha\dagger} c_{\xi\sigma}^{\bar{\alpha}}, \tag{4.110}$$

where $\boldsymbol{u}_\alpha(\boldsymbol{r}_i)$ is the lattice displacement vector at $\boldsymbol{r}_i$, $\boldsymbol{\delta}$ is the nearest neighbor lattice vector, $\boldsymbol{g}(\boldsymbol{\delta}) = \nabla t(\boldsymbol{\delta}) = g_{\mathrm{nn}}\boldsymbol{\delta}_{\mathrm{nn}}$ with the hopping amplitude $t(\boldsymbol{\delta})$ between sites $\boldsymbol{r}_i$ and $\boldsymbol{r}_i+\boldsymbol{\delta}$. The Fourier representation of the electron-phonon coupling is

$$\begin{aligned} H_{\mathrm{el-ph}} &= \sum_{\boldsymbol{\tau}_i} \boldsymbol{\tau}_i \frac{g_{\mathrm{ph}}}{\sqrt{N}} \sum_{\boldsymbol{pq}} \Big[\boldsymbol{u}_{A\boldsymbol{q}} - \boldsymbol{u}_{B\boldsymbol{q}} e^{i\boldsymbol{q}\cdot\boldsymbol{\tau}_i}\Big] \\ &\times \Big[c_{A\boldsymbol{k}+\boldsymbol{q}/2}^\dagger c_{B\boldsymbol{k}-\boldsymbol{q}/2} e^{i\boldsymbol{k}\cdot\boldsymbol{\tau}_i} + c_{B\boldsymbol{k}+\boldsymbol{q}/2}^\dagger c_{A\boldsymbol{k}-\boldsymbol{q}/2} e^{i(\boldsymbol{k}+\boldsymbol{q}/2)\cdot\boldsymbol{\tau}_i}\Big], \\ &= \frac{g_{\mathrm{ph}}}{\sqrt{N}} \sum_{\boldsymbol{pq}} \Big[\boldsymbol{u}_{A\boldsymbol{q}} \cdot \begin{pmatrix} E_{\boldsymbol{k}-\boldsymbol{q}/2}^1 \\ E_{\boldsymbol{k}-\boldsymbol{q}/2}^2 \end{pmatrix} - \boldsymbol{u}_{B\boldsymbol{q}} \cdot \begin{pmatrix} E_{\boldsymbol{k}+\boldsymbol{q}/2}^1 \\ E_{\boldsymbol{k}+\boldsymbol{q}/2}^2 \end{pmatrix}\Big] c_{A\boldsymbol{k}+\boldsymbol{q}/2}^\dagger c_{B\boldsymbol{k}-\boldsymbol{q}/2} \\ &+ \frac{g_{\mathrm{ph}}}{\sqrt{N}} \sum_{\boldsymbol{pq}} \Big[\boldsymbol{u}_{A\boldsymbol{q}} \cdot \begin{pmatrix} E_{\boldsymbol{k}+\boldsymbol{q}/2}^{1*} \\ E_{\boldsymbol{k}+\boldsymbol{q}/2}^{2*} \end{pmatrix} - \boldsymbol{u}_{B\boldsymbol{q}} \cdot \begin{pmatrix} E_{\boldsymbol{k}-\boldsymbol{q}/2}^{1*} \\ E_{\boldsymbol{k}-\boldsymbol{q}/2}^{2*} \end{pmatrix}\Big] c_{B\boldsymbol{k}+\boldsymbol{q}/2}^\dagger c_{A\boldsymbol{k}-\boldsymbol{q}/2}, \\ &= \frac{g_{\mathrm{ph}}}{\sqrt{N}} \sum_{\boldsymbol{pq}} \Big[\boldsymbol{u}_{\boldsymbol{q}}^{\mathrm{OP}} \cdot \boldsymbol{E}_{\boldsymbol{k}} + \boldsymbol{u}_{\boldsymbol{q}}^{\mathrm{AC}} \cdot \Delta\boldsymbol{E}_{\boldsymbol{k},\boldsymbol{q}}\Big] c_{A\boldsymbol{k}+\boldsymbol{q}/2}^\dagger c_{B\boldsymbol{k}-\boldsymbol{q}/2} \\ &+ \frac{g_{\mathrm{ph}}}{\sqrt{N}} \sum_{\boldsymbol{pq}} \Big[\boldsymbol{u}_{\boldsymbol{q}}^{\mathrm{OP}} \cdot \boldsymbol{E}_{\boldsymbol{k}}^* + \boldsymbol{u}_{\boldsymbol{q}}^{\mathrm{AC}} \cdot \Delta\boldsymbol{E}_{\boldsymbol{k},\boldsymbol{q}}^*\Big] c_{B\boldsymbol{k}+\boldsymbol{q}/2}^\dagger c_{A\boldsymbol{k}-\boldsymbol{q}/2}, \end{aligned} \tag{4.111}$$

where we have introduced displacement fields of an optical phonon $\boldsymbol{u}_{\boldsymbol{q}}^{\mathrm{OP}} = \frac{1}{\sqrt{2}}(\boldsymbol{u}_{A\boldsymbol{q}} - \boldsymbol{u}_{B\boldsymbol{q}})$ and an acoustic phonon $\boldsymbol{u}_{\boldsymbol{q}}^{\mathrm{AC}} = \frac{1}{\sqrt{2}}(\boldsymbol{u}_{A\boldsymbol{q}} + \boldsymbol{u}_{B\boldsymbol{q}})$ in the long-wave length limit. The vectors $\boldsymbol{E}_{\boldsymbol{k}}$ and $\Delta\boldsymbol{E}_{\boldsymbol{k},\boldsymbol{q}}$ are obtained from the Taylor expansion for small $\boldsymbol{q}$ as follows, $\boldsymbol{E}_{\boldsymbol{k}+\boldsymbol{q}/2} - \boldsymbol{E}_{\boldsymbol{k}-\boldsymbol{q}/2} = \boldsymbol{E}_{\boldsymbol{k}} + \Delta\boldsymbol{E}_{\boldsymbol{k},\boldsymbol{q}} \cdots$ and $\boldsymbol{E}_{\boldsymbol{k}} = (E_{\boldsymbol{k}}^1, E_{\boldsymbol{k}}^2)$,

$$\Delta\boldsymbol{E}_{\boldsymbol{k},\boldsymbol{q}} = \begin{pmatrix} -\frac{1}{2} \\ -\frac{\sqrt{3}}{2} \end{pmatrix} e^{i\boldsymbol{k}\cdot\boldsymbol{a}_1}(i\boldsymbol{q}\cdot\boldsymbol{a}_1) + \begin{pmatrix} -\frac{1}{2} \\ \frac{\sqrt{3}}{2} \end{pmatrix} e^{i\boldsymbol{k}\cdot\boldsymbol{a}_2}(i\boldsymbol{q}\cdot\boldsymbol{a}_2). \tag{4.112}$$

Finally, the electron-phonon coupling term for acoustic phonons resulting from the bond-length change is

$$\begin{aligned} & S_{\mathrm{el-ph}}[\bar{\boldsymbol{c}}, \boldsymbol{c}, \tilde{u}_L, \tilde{u}_T] \\ = & \sum_{i\tilde{\zeta}\sigma} \int_q \int_k \sum_{\alpha\beta} \bar{c}^{\alpha}_{k+\frac{q}{2}\tilde{\zeta}\sigma} \left[\hat{w}^{\mu}(k,q)\right]_{\alpha\beta} c^{\beta}_{k-\frac{q}{2}\tilde{\zeta}\sigma} \tilde{u}_{\mu}(-q), \end{aligned} \tag{4.113}$$

with the displacement field of acoustic phonons $\boldsymbol{u}_{\mu=T,L} = \tilde{u}_{\mu}\hat{\boldsymbol{e}}_{\mu}$ where $\hat{\boldsymbol{e}}_T = (-\sin\theta_{\boldsymbol{q}}, \cos\theta_{\boldsymbol{q}})$ and $\hat{\boldsymbol{e}}_L = (\cos\theta_{\boldsymbol{q}}, \sin\theta_{\boldsymbol{q}})$ with $\theta_{\boldsymbol{q}} = \tan^{-1}(q_y/q_x)$ and

$$\hat{w}^{\mu}_{k,q} = -\frac{g_{\mathrm{ph}}}{\sqrt{\beta N}} \begin{pmatrix} 0 & \Delta\boldsymbol{E}^*_{\boldsymbol{k},\boldsymbol{q}} \cdot \hat{\boldsymbol{e}}_{\mu}(-q) \\ \Delta\boldsymbol{E}_{\boldsymbol{k},\boldsymbol{q}} \cdot \hat{\boldsymbol{e}}_{\mu}(-q) & 0 \end{pmatrix}. \tag{4.114}$$

After integrating out the electron degrees of freedom, we have a self-energy correction to the phonon action in Eq. (4.28),

$$\delta K_{\mu,\mathrm{el-ph}}(q) = -\frac{1}{2\rho} \int_q \mathrm{tr}\left[\hat{G}_{k+q/2}\hat{w}^{\mu}_{k,q}\hat{G}_{k-q/2}\hat{w}^{\mu}_{k,-q}\right]. \tag{4.115}$$

This is shown in Eq. (4.100).

Chapter 5

Conclusion

In this thesis, we have studied physical properties of the correlation-induced topological states and their various phase transitions.

In Chapter 2, we have explored 2D topological crystalline insulating/half-metallic states in magnetically ordered heavy-fermion systems. On the basis of the Hartree-Fock calculation, we have shown the stability of the AFM topological phase at half filling, which is characterized by a mirror Chern number. Moreover, we have revealed that an AFM topological semimetallic phase is expected in an effective model of a SmB_6 film. We have also shown the stability of the spin-selective topological insulating state characterized by a Chern number in the half-metallic FM phase around quarter filling. In contrast to the previous proposal of the spin-selective topological insulator, which assumed spin $U(1)$ symmetry to obtain such topological properties, we have proposed that these phases can be realized even in the absence of spin $U(1)$ symmetry by taking into account crystalline symmetry. Generally, spin $U(1)$ symmetry is not preserved in the presence of spin-orbit coupling; thus, the present scenario without respecting spin $U(1)$ symmetry will provide a feasible platform to realize magnetic topological insulators for 2D systems.

In Chapter 3, we have elucidated the emergence of correlation-induced symmetry-protected exceptional torus (SPET) for a diamond lattice model with spatially modulated Hubbard interaction. The essential difference from the case for nodal-line semimetals with PT symmetry is that the present chiral symmetry-protected exceptional torus and its low energy excitations (i.e., Fermi volumes) are fixed to the Fermi level. Furthermore, we have revealed that these low energy excitations result in counterintuitive behaviors, exemplifying for the first time the effects of SPETs on magnetic responses. Specifically, by employing the dynamical mean-field theory and random phase approximation, we have found that the magnetic susceptibility for B-sublattice becomes larger than that for A-sublattice, although the interaction strength is opposite ($U_A > U_B$). For this counterintuitive response to the homogeneous magnetic field, the chiral symmetry is essential, leading to the enhancement of the local density of states at the Fermi level only for B-sublattice.

In Chapter 4, we have analyzed the impact of the coupling between the nematic order parameter and the elastic degrees of freedom on the low energy properties of phonons. Phenomenological analysis based on the Ginzburg-Landau-Wilson action has clarified an isotropic divergence of the transverse sound attenuation coefficient and the transverse sound velocity renormalization. Both features are quite contrasted to the strong anisotropy in the case of the C_4-breaking nematic case. We have also determined the mean-field phase diagram by a microscopic extended Hubbard model with impurity. The transition temperature takes its maximum near VHs, and the large density of states favors the ne-

matic phase transition. The order of phase transition is of weak first-order in a wide range of band filling and, with increasing the impurity scattering, the first order transition line at low temperatures gets closer to the second-order line, making the transition weakly first-order in a wider parameter region. Furthermore, it has been confirmed that the enhancement of the ultrasound attenuation coefficient can be observed in the case of a weak first-order phase transition. We have proposed to detect the intrinsic three-state Potts nematic phase transition by measuring the ultrasound attenuation of the transverse acoustic phonon. Namely the ultrasound attenuation coefficient shows an isotropic divergence which is proportional to the momentum $|\boldsymbol{q}|$ and the sound velocity renormalization also show an isotropic angle dependence.

In this thesis, we have contributed to a deeper understanding of correlation-induced topological states in Chapter 3 and its magnetic phase transition in Chapter 2 or electron-nematic phase transition in Chapter 4. Finally, we discuss our future prospects. In relation to Chapter 2, it is important to investigate not only the ground state stability of the magnetic topological phase, but also its effects on transport properties and responses, and to find alternatives to magnetic-impurity doped topological insulators. In realtion to Capter 3, in the case of chiral symmetry, a large Fermi volume has been realized, which may have some influence on the physical properties, but it is a future issue to clarify the influence on physical quantities in the case of no symmetry and the relationship with the mystery of quantum oscillation in bulk Kondo insulators. In relation to Chapter 4, it is a future issue to clarify the relationship between non-Fermi liquid states, superconducting instability, which includes topological and/or nematic superconductivity, induced by three-state Potts nematic fluctuations. The interplay between the Coulomb interaction and the topological band structure leads to finding new physical phenomena and it will become even more important to understand the origin of intertwined orders and a varietie of quantum phases of matter.

Bibliography

[1] C. L. Kane and E. J. Mele, Phys. Rev. Lett. **95**, 226801 (2005).

[2] C. L. Kane and E. J. Mele, Phys. Rev. Lett. **95**, 146802 (2005).

[3] M. Z. Hasan and C. L. Kane, Rev. Mod. Phys. **82**, 3045 (2010).

[4] X.-L. Qi and S.-C. Zhang, Rev. Mod. Phys. **83**, 1057 (2011).

[5] S. Rachel, Reports on Progress in Physics **81**, 116501 (2018).

[6] M. Dzero, K. Sun, V. Galitski, and P. Coleman, Phys. Rev. Lett. **104**, 106408 (2010).

[7] M. Dzero, K. Sun, P. Coleman, and V. Galitski, Phys. Rev. B **85**, 045130 (2012).

[8] M. Dzero, J. Xia, V. Galitski, and P. Coleman, Annu. Rev. Condens. Matter Phys. **7**, 249 (2016).

[9] D. Pesin and L. Balents, Nat. Phys. **6**, 376 (2010).

[10] T. Yoshida, R. Peters, S. Fujimoto, and N. Kawakami, Phys. Rev. Lett. **112**, 196404 (2014).

[11] T. Yoshida and N. Kawakami, Phys. Rev. B **94**, 085149 (2016).

[12] H.-Q. Wu, Y.-Y. He, Y.-Z. You, T. Yoshida, N. Kawakami, C. Xu, Z. Y. Meng, and Z.-Y. Lu, Phys. Rev. B **94**, 165121 (2016).

[13] K. Kudo, T. Yoshida, and Y. Hatsugai, Phys. Rev. Lett. **123**, 196402 (2019).

[14] L. Fidkowski and A. Kitaev, Phys. Rev. B **81**, 134509 (2010).

[15] L. Fidkowski and A. Kitaev, Phys. Rev. B **83**, 075103 (2011).

[16] A. M. Turner, F. Pollmann, and E. Berg, Phys. Rev. B **83**, 075102 (2011).

[17] S. Ryu and S.-C. Zhang, Phys. Rev. B **85**, 245132 (2012).

[18] H. Yao and S. Ryu, Phys. Rev. B **88**, 064507 (2013).

[19] X.-L. Qi, New J. Phys. **15**, 065002 (2013).

[20] Y.-M. Lu and A. Vishwanath, Phys. Rev. B **86**, 125119 (2012).

[21] M. Levin and A. Stern, Phys. Rev. B **86**, 115131 (2012).

[22] L. Fidkowski, X. Chen, and A. Vishwanath, Phys. Rev. X **3**, 041016 (2013).

[23] Z.-C. Gu and X.-G. Wen, Phys. Rev. B **90**, 115141 (2014).

[24] C.-T. Hsieh, T. Morimoto, and S. Ryu, Phys. Rev. B **90**, 245111 (2014).

[25] C. Wang, A. C. Potter, and T. Senthil, Science **343**, 629 (2014).

[26] T. Morimoto, A. Furusaki, and C. Mudry, Phys. Rev. B **92**, 125104 (2015).

[27] H. Isobe and L. Fu, Phys. Rev. B **92**, 081304 (2015).

[28] T. Yoshida and A. Furusaki, Phys. Rev. B **92**, 085114 (2015).

[29] Y.-Z. You and C. Xu, Phys. Rev. B **90**, 245120 (2014).

[30] T. Yoshida, A. Daido, Y. Yanase, and N. Kawakami, Phys. Rev. Lett. **118**, 147001 (2017).

[31] T. Yoshida, I. Danshita, R. Peters, and N. Kawakami, Phys. Rev. Lett. **121**, 025301 (2018).

[32] C.-Z. Chang, J. Zhang, X. Feng, J. Shen, Z. Zhang, M. Guo, K. Li, Y. Ou, P. Wei, L.-L. Wang, et al., Science **340**, 167 (2013).

[33] Y. Tokura, K. Yasuda, and A. Tsukazaki, Nature Reviews Physics **1**, 126 (2019).

[34] N. Hatano and D. R. Nelson, Phys. Rev. Lett. **77**, 570 (1996).

[35] C. M. Bender and S. Boettcher, Phys. Rev. Lett. **80**, 5243 (1998).

[36] T. Fukui and N. Kawakami, Phys. Rev. B **58**, 16051 (1998).

[37] V. Kozii and L. Fu, arXiv preprint arXiv:1708.05841 (2017).

[38] M. Papaj, H. Isobe, and L. Fu, Phys. Rev. B **99**, 201107 (2019).

[39] H. Shen and L. Fu, Phys. Rev. Lett. **121**, 026403 (2018).

[40] T. Yoshida, R. Peters, and N. Kawakami, Phys. Rev. B **98**, 035141 (2018).

[41] P. A. McClarty and J. G. Rau, Phys. Rev. B **100**, 100405 (2019).

[42] E. J. Bergholtz and J. C. Budich, Phys. Rev. Research **1**, 012003 (2019).

[43] A. P. Schnyder, S. Ryu, A. Furusaki, and A. W. W. Ludwig, Phys. Rev. B **78**, 195125 (2008).

[44] A. P. Schnyder, S. Ryu, A. Furusaki, and A. W. W. Ludwig, AIP Conference Proceedings **1134**, 10 (2009).

[45] A. Kitaev, AIP Conference Proceedings **1134**, 22 (2009).

[46] L. Fu, Phys. Rev. Lett. **106**, 106802 (2011).

[47] T. H. Hsieh, H. Lin, J. Liu, W. Duan, A. Bansil, and L. Fu, Nat. Commun. **3**, 982 (2012).

[48] Y. Tanaka, Z. Ren, T. Sato, K. Nakayama, S. Souma, T. Takahashi, K. Segawa, and Y. Ando, Nat. Phys. **8**, 800 (2012).

[49] P. Dziawa, B. J. Kowalski, K. Dybko, R. Buczko, A. Szczerbakow, M. Szot, E. Łusakowska, T. Balasubramanian, B. M. Wojek, M. H. Bastian, M. H. Berntsen, O. Tjernberg, and T. Story, Nat. Mater. **11**, 1023 (2012).

[50] S. Murakami, New Journal of Physics **9**, 356 (2007).

[51] X. Wan, A. M. Turner, A. Vishwanath, and S. Y. Savrasov, Phys. Rev. B **83**, 205101 (2011).

[52] A. A. Burkov and L. Balents, Phys. Rev. Lett. **107**, 127205 (2011).

[53] H. Weng, C. Fang, Z. Fang, B. A. Bernevig, and X. Dai, Phys. Rev. X **5**, 011029 (2015).

[54] S.-Y. Xu, I. Belopolski, N. Alidoust, M. Neupane, G. Bian, C. Zhang, R. Sankar, G. Chang, Z. Yuan, C.-C. Lee, S.-M. Huang, H. Zheng, J. Ma, D. S. Sanchez, B. Wang, A. Bansil, F. Chou, P. P. Shibayev, H. Lin, S. Jia, and M. Z. Hasan, Science **349**, 613 (2015).

[55] B. Q. Lv, H. M. Weng, B. B. Fu, X. P. Wang, H. Miao, J. Ma, P. Richard, X. C. Huang, L. X. Zhao, G. F. Chen, Z. Fang, X. Dai, T. Qian, and H. Ding, Phys. Rev. X **5**, 031013 (2015).

[56] N. P. Armitage, E. J. Mele, and A. Vishwanath, Rev. Mod. Phys. **90**, 015001 (2018).

[57] A. Y. Kitaev, Physics-Uspekhi **44**, 131 (2001).

[58] V. Mourik, K. Zuo, S. M. Frolov, S. R. Plissard, E. P. A. M. Bakkers, and L. P. Kouwenhoven, Science **336**, 1003 (2012).

[59] L. P. Rokhinson, X. Liu, and J. K. Furdyna, Nature Physics **8**, 795 (2012).

[60] A. Das, Y. Ronen, Y. Most, Y. Oreg, M. Heiblum, and H. Shtrikman, Nat. Phys. **8**, 887 (2012).

[61] T. Yoshida, M. Sigrist, and Y. Yanase, Phys. Rev. Lett. **115**, 027001 (2015).

[62] A. Daido and Y. Yanase, Phys. Rev. B **94**, 054519 (2016).

[63] M. Imada, A. Fujimori, and Y. Tokura, Rev. Mod. Phys. **70**, 1039 (1998).

[64] M. Sigrist and K. Ueda, Rev. Mod. Phys. **63**, 239 (1991).

[65] L. Balents, Nature **464**, 199 (2010).

[66] W. Witczak-Krempa, G. Chen, Y. B. Kim, and L. Balents, Annu. Rev. Condens. Matter Phys. **5**, 57 (2014).

[67] M. Hohenadler, T. C. Lang, and F. F. Assaad, Phys. Rev. Lett. **106**, 100403 (2011).

[68] Y. Yamaji and M. Imada, Phys. Rev. B **83**, 205122 (2011).

[69] S.-L. Yu, X. C. Xie, and J.-X. Li, Phys. Rev. Lett. **107**, 010401 (2011).

[70] T. Yoshida, S. Fujimoto, and N. Kawakami, Phys. Rev. B **85**, 125113 (2012).

[71] Y. Tada, R. Peters, M. Oshikawa, A. Koga, N. Kawakami, and S. Fujimoto, Phys. Rev. B **85**, 165138 (2012).

[72] W. Wu, S. Rachel, W.-M. Liu, and K. Le Hur, Phys. Rev. B **85**, 205102 (2012).

[73] T. Yoshida, R. Peters, S. Fujimoto, and N. Kawakami, Phys. Rev. B **87**, 085134 (2013).

[74] V. Gurarie, Phys. Rev. B **83**, 085426 (2011).

[75] Z. Wang, X.-L. Qi, and S.-C. Zhang, Phys. Rev. Lett. **105**, 256803 (2010).

[76] A. M. Essin and V. Gurarie, Phys. Rev. B **84**, 125132 (2011).

[77] Z. Wang and S.-C. Zhang, Phys. Rev. X **2**, 031008 (2012).

[78] Z. Wang and B. Yan, Journal of Physics: Condensed Matter **25**, 155601 (2013).

[79] S. R. Manmana, A. M. Essin, R. M. Noack, and V. Gurarie, Phys. Rev. B **86**, 205119 (2012).

[80] R. S. K. Mong, A. M. Essin, and J. E. Moore, Phys. Rev. B **81**, 245209 (2010).

[81] D. Zheng, G.-M. Zhang, and C. Wu, Phys. Rev. B **84**, 205121 (2011).

[82] C. Griset and C. Xu, Phys. Rev. B **85**, 045123 (2012).

[83] A. M. Essin and V. Gurarie, Phys. Rev. B **85**, 195116 (2012).

[84] S. Okamoto, W. Zhu, Y. Nomura, R. Arita, D. Xiao, and N. Nagaosa, Phys. Rev. B **89**, 195121 (2014).

[85] H. Guo, S. Feng, and S.-Q. Shen, Phys. Rev. B **83**, 045114 (2011).

[86] J. He, Y.-H. Zong, S.-P. Kou, Y. Liang, and S. Feng, Phys. Rev. B **84**, 035127 (2011).

[87] J. He, B. Wang, and S.-P. Kou, Phys. Rev. B **86**, 235146 (2012).

[88] T. Yoshida, R. Peters, S. Fujimoto, and N. Kawakami, Phys. Rev. B **87**, 165109 (2013).

[89] S. Rachel and K. Le Hur, Phys. Rev. B **82**, 075106 (2010).

[90] C. N. Varney, K. Sun, M. Rigol, and V. Galitski, Phys. Rev. B **82**, 115125 (2010).

[91] G. R. Stewart, Rev. Mod. Phys. **56**, 755 (1984).

[92] P. Lee, T. Rice, J. Serene, L. Sham, and J. Wilkins, Comments on Condensed Matter Physics **12**, 99 (1986).

[93] H. Tsunetsugu, M. Sigrist, and K. Ueda, Rev. Mod. Phys. **69**, 809 (1997).

[94] P. Coleman, Introduction to many-body physics (Cambridge University Press, 2015).

[95] A. Menth, E. Buehler, and T. H. Geballe, Phys. Rev. Lett. **22**, 295 (1969).

[96] M. Neupane, N. Alidoust, S.-Y. Xu, T. Kondo, Y. Ishida, D.-J. Kim, C. Liu, I. Belopolski, Y. J. Jo, T.-R. Chang, H.-T. Jeng, T. Durakiewicz, L. Balicas, H. Lin, A. Bansil, S. Shin, Z. Fisk, and M. Z. Hasan, Nat. Commun. **4**, 2991 (2013).

[97] N. Xu, P. K. Biswas, J. H. Dil, R. S. Dhaka, G. Landolt, S. Muff, C. E. Matt, X. Shi, N. Plumb, M. Radović, E. Pomjakushina, K. Conder, A. Amato, S. V. Borisenko, R. Yu, H.-M. Weng, Z. Fang, X. Dai, J. Mesot, H. Ding, and M. Shi, Nat. Commun. **5**, 4566 (2014).

[98] H. Weng, J. Zhao, Z. Wang, Z. Fang, and X. Dai, Phys. Rev. Lett. **112**, 016403 (2014).

[99] J. C. Cooley, M. C. Aronson, Z. Fisk, and P. C. Canfield, Phys. Rev. Lett. **74**, 1629 (1995).

[100] G. Li, Z. Xiang, F. Yu, T. Asaba, B. Lawson, P. Cai, C. Tinsman, A. Berkley, S. Wolgast, Y. S. Eo, et al., Science **346**, 1208 (2014).

[101] B. Tan, Y.-T. Hsu, B. Zeng, M. C. Hatnean, N. Harrison, Z. Zhu, M. Hartstein, M. Kiourlappou, A. Srivastava, M. Johannes, et al., Science **349**, 287 (2015).

[102] Z. Xiang, B. Lawson, T. Asaba, C. Tinsman, L. Chen, C. Shang, X. H. Chen, and L. Li, Phys. Rev. X **7**, 031054 (2017).

[103] M. Hartstein, W. Toews, Y.-T. Hsu, B. Zeng, X. Chen, M. C. Hatnean, Q. Zhang, S. Nakamura, A. Padgett, G. Rodway-Gant, et al., Nat. Phys. **14**, 166 (2018).

[104] S. M. Thomas, X. Ding, F. Ronning, V. Zapf, J. D. Thompson, Z. Fisk, J. Xia, and P. F. S. Rosa, Phys. Rev. Lett. **122**, 166401 (2019).

[105] T. T. Terashima, Y. H. Matsuda, Y. Kohama, A. Ikeda, A. Kondo, K. Kindo, and F. Iga, Phys. Rev. Lett. **120**, 257206 (2018).

[106] Y. Sato, Z. Xiang, Y. Kasahara, T. Taniguchi, S. Kasahara, L. Chen, T. Asaba, C. Tinsman, H. Murayama, O. Tanaka, et al., Nat. Phys. **15**, 954 (2019).

[107] S. Dzsaber, L. Prochaska, A. Sidorenko, G. Eguchi, R. Svagera, M. Waas, A. Prokofiev, Q. Si, and S. Paschen, Phys. Rev. Lett. **118**, 246601 (2017).

[108] H.-H. Lai, S. E. Grefe, S. Paschen, and Q. Si, Proc. Natl. Acad. Sci. U.S.A. **115**, 93 (2018).

[109] C. Guo, F. Wu, Z. Wu, M. Smidman, C. Cao, A. Bostwick, C. Jozwiak, E. Rotenberg, Y. Liu, F. Steglich, et al., Nat. Commun. **9**, 1 (2018).

[110] S. Dzsaber, X. Yan, M. Taupin, G. Eguchi, A. Prokofiev, T. Shiroka, P. Blaha, O. Rubel, S. E. Grefe, H.-H. Lai, et al., Proc. Natl. Acad. Sci. U.S.A. **118** (2021), 10.1073/pnas.2013386118.

[111] A. Kofuji, Y. Michishita, and R. Peters, Phys. Rev. B **104**, 085151 (2021).

[112] E. D. Mun, S. L. Bud'ko, C. Martin, H. Kim, M. A. Tanatar, J.-H. Park, T. Murphy, G. M. Schmiedeshoff, N. Dilley, R. Prozorov, and P. C. Canfield, Phys. Rev. B **87**, 075120 (2013).

[113] K. S. D. Beach and F. F. Assaad, Phys. Rev. B **77**, 205123 (2008).

[114] R. Peters, N. Kawakami, and T. Pruschke, Phys. Rev. Lett. **108**, 086402 (2012).

[115] O. Howczak and J. Spalek, Journal of Physics: Condensed Matter **24**, 205602 (2012).

[116] R. Peters and N. Kawakami, Phys. Rev. B **86**, 165107 (2012).

[117] D. Golež and R. Žitko, Phys. Rev. B **88**, 054431 (2013).

[118] K. Shiozaki, M. Sato, and K. Gomi, Phys. Rev. B **93**, 195413 (2016).

[119] M. M. Otrokov, I. I. Klimovskikh, H. Bentmann, D. Estyunin, A. Zeugner, Z. S. Aliev, S. Gaß, A. Wolter, A. Koroleva, A. M. Shikin, et al., Nature **576**, 416 (2019).

[120] R.-J. Slager, A. Mesaros, V. Juričić, and J. Zaanen, Nat. Phys. **9**, 98 (2013).

[121] J. Kruthoff, J. de Boer, J. van Wezel, C. L. Kane, and R.-J. Slager, Phys. Rev. X **7**, 041069 (2017).

[122] R. Shankar, Rev. Mod. Phys. **66**, 129 (1994).

[123] I. Y. Pomeranchuk, Sov.Phys.JETP **8**, 361 (1958).

[124] S. A. Kivelson, E. Fradkin, and V. J. Emery, Nature **393**, 550 (1998).

[125] E. Fradkin, S. A. Kivelson, M. J. Lawler, J. P. Eisenstein, and A. P. Mackenzie, Annu. Rev. Condens. Matter Phys. **1**, 153 (2010).

[126] E. Fradkin, S. A. Kivelson, and J. M. Tranquada, Rev. Mod. Phys. **87**, 457 (2015).

[127] R. M. Fernandes, P. P. Orth, and J. Schmalian, Annu. Rev. Condens. Matter Phys. **10**, 133 (2019).

[128] V. Oganesyan, S. A. Kivelson, and E. Fradkin, Phys. Rev. B **64**, 195109 (2001).

[129] H. v. Löhneysen, A. Rosch, M. Vojta, and P. Wölfle, Rev. Mod. Phys. **79**, 1015 (2007).

[130] M. Garst and A. V. Chubukov, Phys. Rev. B **81**, 235105 (2010).

[131] J. A. Hertz, Phys. Rev. B **14**, 1165 (1976).

[132] A. J. Millis, Phys. Rev. B **48**, 7183 (1993).

[133] T. Moriya, Spin fluctuations in itinerant electron magnetism, Vol. 56 (Springer Science & Business Media, 2012).

[134] H. Adachi and M. Sigrist, Phys. Rev. B **80**, 155123 (2009).

[135] I. Paul and M. Garst, Phys. Rev. Lett. **118**, 227601 (2017).

[136] V. S. de Carvalho and R. M. Fernandes, Phys. Rev. B **100**, 115103 (2019).

[137] T. Moriya and K. Ueda, Advances in Physics **49**, 555 (2000).

[138] Y. Yanase, T. Jujo, T. Nomura, H. Ikeda, T. Hotta, and K. Yamada, Phys. Rep. **387**, 1 (2003).

[139] H. Kontani and S. Onari, Phys. Rev. Lett. **104**, 157001 (2010).

[140] S. Sumita and Y. Yanase, Phys. Rev. Research **2**, 033225 (2020).

[141] P. Chandra, P. Coleman, and A. I. Larkin, Phys. Rev. Lett. **64**, 88 (1990).

[142] R. Fernandes, A. Chubukov, and J. Schmalian, Nature physics **10**, 97 (2014).

[143] M. Hecker and J. Schmalian, npj Quantum Mater. **3**, 26 (2018).

[144] R. M. Fernandes and L. Fu, Phys. Rev. Lett. **127**, 047001 (2021).

[145] Y. Cao, V. Fatemi, A. Demir, S. Fang, S. L. Tomarken, J. Y. Luo, J. D. Sanchez-Yamagishi, K. Watanabe, T. Taniguchi, E. Kaxiras, et al., Nature **556**, 80 (2018).

[146] Y. Cao, V. Fatemi, S. Fang, K. Watanabe, T. Taniguchi, E. Kaxiras, and P. Jarillo-Herrero, Nature **556**, 43 (2018).

[147] M. Yankowitz, S. Chen, H. Polshyn, Y. Zhang, K. Watanabe, T. Taniguchi, D. Graf, A. F. Young, and C. R. Dean, Science **363**, 1059 (2019).

[148] X. Lu, P. Stepanov, W. Yang, M. Xie, M. A. Aamir, I. Das, C. Urgell, K. Watanabe, T. Taniguchi, G. Zhang, et al., Nature **574**, 653 (2019).

[149] A. L. Sharpe, E. J. Fox, A. W. Barnard, J. Finney, K. Watanabe, T. Taniguchi, M. Kastner, and D. Goldhaber-Gordon, Science **365**, 605 (2019).

[150] M. Serlin, C. Tschirhart, H. Polshyn, Y. Zhang, J. Zhu, K. Watanabe, T. Taniguchi, L. Balents, and A. Young, Science **367**, 900 (2020).

[151] Y. Xie, B. Lian, B. Jäck, X. Liu, C.-L. Chiu, K. Watanabe, T. Taniguchi, B. A. Bernevig, and A. Yazdani, Nature **572**, 101 (2019).

[152] R. Bistritzer and A. H. MacDonald, Proc. Natl. Acad. Sci. U.S.A **108**, 12233 (2011).

[153] N. F. Q. Yuan and L. Fu, Phys. Rev. B **98**, 045103 (2018).

[154] J. Kang and O. Vafek, Phys. Rev. X **8**, 031088 (2018).

[155] M. Koshino, N. F. Q. Yuan, T. Koretsune, M. Ochi, K. Kuroki, and L. Fu, Phys. Rev. X **8**, 031087 (2018).

[156] H. C. Po, L. Zou, A. Vishwanath, and T. Senthil, Phys. Rev. X **8**, 031089 (2018).

[157] L. Zou, H. C. Po, A. Vishwanath, and T. Senthil, Phys. Rev. B **98**, 085435 (2018).

[158] H. C. Po, L. Zou, T. Senthil, and A. Vishwanath, Phys. Rev. B **99**, 195455 (2019).

[159] C. Xu and L. Balents, Phys. Rev. Lett. **121**, 087001 (2018).

[160] H. Isobe, N. F. Q. Yuan, and L. Fu, Phys. Rev. X **8**, 041041 (2018).

[161] V. Kozii, H. Isobe, J. W. F. Venderbos, and L. Fu, Phys. Rev. B **99**, 144507 (2019).

[162] D. V. Chichinadze, L. Classen, and A. V. Chubukov, Phys. Rev. B **102**, 125120 (2020).

[163] Y. Wang, J. Kang, and R. M. Fernandes, Phys. Rev. B **103**, 024506 (2021).

[164] Y. Choi, J. Kemmer, Y. Peng, A. Thomson, H. Arora, R. Polski, Y. Zhang, H. Ren, J. Alicea, G. Refael, et al., Nat. Phys. **15**, 1174 (2019).

[165] A. Kerelsky, L. J. McGilly, D. M. Kennes, L. Xian, M. Yankowitz, S. Chen, K. Watanabe, T. Taniguchi, J. Hone, C. Dean, et al., Nature **572**, 95 (2019).

[166] Y. Jiang, X. Lai, K. Watanabe, T. Taniguchi, K. Haule, J. Mao, and E. Y. Andrei, Nature **573**, 91 (2019).

[167] Y. Cao, D. Rodan-Legrain, J. M. Park, N. F. Yuan, K. Watanabe, T. Taniguchi, R. M. Fernandes, L. Fu, and P. Jarillo-Herrero, Science **372**, 264 (2021).

[168] S. Liu, E. Khalaf, J. Y. Lee, and A. Vishwanath, Phys. Rev. Research **3**, 013033 (2021).

[169] Y.-H. Zhang, H. C. Po, and T. Senthil, Phys. Rev. B **100**, 125104 (2019).

[170] A. O. Sboychakov, A. V. Rozhkov, A. L. Rakhmanov, and F. Nori, Phys. Rev. B **102**, 155142 (2020).

[171] R. M. Fernandes and J. W. F. Venderbos, Sci. Adv. **6**, eaba8834 (2020).

[172] D. E. Parker, T. Soejima, J. Hauschild, M. P. Zaletel, and N. Bultinck, Phys. Rev. Lett. **127**, 027601 (2021).

[173] E. Brillaux, D. Carpentier, A. A. Fedorenko, and L. Savary, arXiv preprint arXiv:2008.05041 (2020).

[174] S. Onari and H. Kontani, arXiv preprint arXiv:2011.01158 (2020).

[175] M. Koshino and Y.-W. Son, Phys. Rev. B **100**, 075416 (2019).

[176] H. Ochoa, Phys. Rev. B **100**, 155426 (2019).

[177] K. Matano, M. Kriener, K. Segawa, Y. Ando, and G.-q. Zheng, Nat. Phys. **12**, 852 (2016).

[178] S. Yonezawa, K. Tajiri, S. Nakata, Y. Nagai, Z. Wang, K. Segawa, Y. Ando, and Y. Maeno, Nat. Phys. **13**, 123 (2017).

[179] Y. Pan, A. M. Nikitin, G. K. Araizi, Y. K. Huang, Y. Matsushita, T. Naka, and A. de Visser, Sci. Rep. **6**, 28632 (2016).

[180] G. Du, Y. Li, J. Schneeloch, R. D. Zhong, H. Gu, GenDa andYang, H. Lin, and H.-H. Wen, Sci. China-Phys. Mech. Astron. **60**, 037411 (2017).

[181] J. Shen, W.-Y. He, N. F. Q. Yuan, Z. Huang, C.-w. Cho, S. H. Lee, Y. San Hor, K. T. Law, and R. Lortz, npj Quantum Mater. **2**, 59 (2017).

[182] T. Asaba, B. J. Lawson, C. Tinsman, L. Chen, P. Corbae, G. Li, Y. Qiu, Y. S. Hor, L. Fu, and L. Li, Phys. Rev. X **7**, 011009 (2017).

[183] M. Smylie, K. Willa, H. Claus, A. Koshelev, K. Song, W.-K. Kwok, Z. Islam, G. Gu, J. Schneeloch, R. Zhong, et al., Sci. Rep. **8**, 7666 (2018).

[184] R. Tao, Y.-J. Yan, X. Liu, Z.-W. Wang, Y. Ando, Q.-H. Wang, T. Zhang, and D.-L. Feng, Phys. Rev. X **8**, 041024 (2018).

[185] S. Yonezawa, Condens. Matter **4**, 2 (2019).

[186] A. Y. Kuntsevich, M. A. Bryzgalov, V. A. Prudkoglyad, V. P. Martovitskii, Y. G. Selivanov, and E. G. Chizhevskii, New J. Phys. **20**, 103022 (2018).

[187] Y. Sun, S. Kittaka, T. Sakakibara, K. Machida, J. Wang, J. Wen, X. Xing, Z. Shi, and T. Tamegai, Phys. Rev. Lett. **123**, 027002 (2019).

[188] C.-w. Cho, J. Shen, J. Lyu, O. Atanov, Q. Chen, S. H. Lee, Y. San Hor, D. J. Gawryluk, E. Pomjakushina, M. Bartkowiak, et al., Nat. Commun. **11**, 3056 (2020).

[189] A. Guo, G. J. Salamo, D. Duchesne, R. Morandotti, M. Volatier-Ravat, V. Aimez, G. A. Siviloglou, and D. N. Christodoulides, Phys. Rev. Lett. **103**, 093902 (2009).

[190] C. E. Rüter, K. G. Makris, R. El-Ganainy, D. N. Christodoulides, M. Segev, and D. Kip, Nat. Phys. **6**, 192 (2010).

[191] A. Regensburger, C. Bersch, M.-A. Miri, G. Onishchukov, D. N. Christodoulides, and U. Peschel, Nature **488**, 167 (2012).

[192] K. Esaki, M. Sato, K. Hasebe, and M. Kohmoto, Phys. Rev. B **84**, 205128 (2011).

[193] M. Sato, K. Hasebe, K. Esaki, and M. Kohmoto, Progress of Theoretical Physics **127**, 937 (2012).

[194] B. Zhen, C. W. Hsu, Y. Igarashi, L. Lu, I. Kaminer, A. Pick, S.-L. Chua, J. D. Joannopoulos, and M. Soljačić, Nature **525**, 354 (2015).

[195] T. E. Lee, Phys. Rev. Lett. **116**, 133903 (2016).

[196] Y. Ashida, S. Furukawa, and M. Ueda, Phys. Rev. A **94**, 053615 (2016).

[197] P. San-Jose, J. Cayao, E. Prada, and R. Aguado, Sci. Rep. **6**, 21427 (2016).

[198] Y. Ashida, S. Furukawa, and M. Ueda, Nat. Commun. **8**, 15791 (2017).

[199] Z. Gong, S. Higashikawa, and M. Ueda, Phys. Rev. Lett. **118**, 200401 (2017).

[200] A. U. Hassan, B. Zhen, M. Soljačić, M. Khajavikhan, and D. N. Christodoulides, Phys. Rev. Lett. **118**, 093002 (2017).

[201] H. Shen, B. Zhen, and L. Fu, Phys. Rev. Lett. **120**, 146402 (2018).

[202] K. Kawabata, Y. Ashida, H. Katsura, and M. Ueda, Phys. Rev. B **98**, 085116 (2018).

[203] Z. Gong, Y. Ashida, K. Kawabata, K. Takasan, S. Higashikawa, and M. Ueda, Phys. Rev. X **8**, 031079 (2018).

[204] S. Yao and Z. Wang, Phys. Rev. Lett. **121**, 086803 (2018).

[205] S. Yao, F. Song, and Z. Wang, Phys. Rev. Lett. **121**, 136802 (2018).

[206] F. K. Kunst, E. Edvardsson, J. C. Budich, and E. J. Bergholtz, Phys. Rev. Lett. **121**, 026808 (2018).

[207] E. Edvardsson, F. K. Kunst, and E. J. Bergholtz, Phys. Rev. B **99**, 081302 (2019).

[208] K. Kawabata, S. Higashikawa, Z. Gong, Y. Ashida, and M. Ueda, Nat. Commun. **10**, 297 (2019).

[209] K. Kawabata, K. Shiozaki, M. Ueda, and M. Sato, Phys. Rev. X **9**, 041015 (2019).

[210] K. Kawabata, T. Bessho, and M. Sato, Phys. Rev. Lett. **123**, 066405 (2019).

[211] D. Leykam, K. Y. Bliokh, C. Huang, Y. D. Chong, and F. Nori, Phys. Rev. Lett. **118**, 040401 (2017).

[212] J. González and R. A. Molina, Phys. Rev. B **96**, 045437 (2017).

[213] R. A. Molina and J. González, Phys. Rev. Lett. **120**, 146601 (2018).

[214] H. Zhou, C. Peng, Y. Yoon, C. W. Hsu, K. A. Nelson, L. Fu, J. D. Joannopoulos, M. Soljačić, and B. Zhen, Science **359**, 1009 (2018).

[215] A. Cerjan, S. Huang, M. Wang, K. P. Chen, Y. Chong, and M. C. Rechtsman, Nat. Photonics **13**, 623 (2019).

[216] A. A. Zyuzin and A. Y. Zyuzin, Phys. Rev. B **97**, 041203 (2018).

[217] Y. Xu, S.-T. Wang, and L.-M. Duan, Phys. Rev. Lett. **118**, 045701 (2017).

[218] A. Cerjan, M. Xiao, L. Yuan, and S. Fan, Phys. Rev. B **97**, 075128 (2018).

[219] J. Carlström, M. Stålhammar, J. C. Budich, and E. J. Bergholtz, Phys. Rev. B **99**, 161115 (2019).

[220] J. Carlström and E. J. Bergholtz, Phys. Rev. A **98**, 042114 (2018).

[221] H. Wang, J. Ruan, and H. Zhang, Phys. Rev. B **99**, 075130 (2019).

[222] Z. Yang and J. Hu, Phys. Rev. B **99**, 081102 (2019).

[223] K. Moors, A. A. Zyuzin, A. Y. Zyuzin, R. P. Tiwari, and T. L. Schmidt, Phys. Rev. B **99**, 041116 (2019).

[224] R. Okugawa and T. Yokoyama, Phys. Rev. B **99**, 041202 (2019).

[225] J. C. Budich, J. Carlström, F. K. Kunst, and E. J. Bergholtz, Phys. Rev. B **99**, 041406 (2019).

[226] T. Yoshida, R. Peters, N. Kawakami, and Y. Hatsugai, Phys. Rev. B **99**, 121101 (2019).

[227] T. Yoshida and Y. Hatsugai, arXiv preprint arXiv:1904.10764 (2019).

[228] Y. Nagai, Y. Qi, H. Isobe, V. Kozii, and L. Fu, Phys. Rev. Lett. **125**, 227204 (2020).

[229] Y. Michishita, T. Yoshida, and R. Peters, Phys. Rev. B **101**, 085122 (2020).

[230] Y. Michishita and R. Peters, Phys. Rev. Lett. **124**, 196401 (2020).

[231] T. Matsushita, Y. Nagai, and S. Fujimoto, J. Phys. Soc. Jpn **90**, 074703 (2021).

[232] T. Yoshida, R. Peters, N. Kawakami, and Y. Hatsugai, Prog. Theor. Exp. Phys. **12A109** (2020), 10.1093/ptep/ptaa059.

[233] Y. Michishita and R. Peters, Phys. Rev. B **103**, 195133 (2021).

[234] R. Rausch, R. Peters, and T. Yoshida, New J. Phys. **23**, 013011 (2021).

[235] T. Yoshida and Y. Hatsugai, Phys. Rev. B **104**, 075106 (2021).

[236] R. Peters, K. Kimura, Y. Michishita, T. Yoshida, and N. Kawakami, arXiv preprint arXiv:2109.09298 (2021).

[237] M. Legner, A. Rüegg, and M. Sigrist, Phys. Rev. B **89**, 085110 (2014).

[238] M. Legner, A. Rüegg, and M. Sigrist, Phys. Rev. Lett. **115**, 156405 (2015).

[239] T. Takimoto, J. Phys. Soc. Jpn **80**, 123710 (2011).

[240] M.-T. Tran, T. Takimoto, and K.-S. Kim, Phys. Rev. B **85**, 125128 (2012).

[241] F. Lu, J. Zhao, H. Weng, Z. Fang, and X. Dai, Phys. Rev. Lett. **110**, 096401 (2013).

[242] V. Alexandrov, M. Dzero, and P. Coleman, Phys. Rev. Lett. **111**, 226403 (2013).

[243] T. Fukui, Y. Hatsugai, and H. Suzuki, J. Phys. Soc. Jpn **74**, 1674 (2005).

[244] R.-X. Zhang, C. Xu, and C.-X. Liu, Phys. Rev. B **94**, 235128 (2016).

[245] K. Kimura, T. Yoshida, and N. Kawakami, J. Phys. Soc. Japan **87**, 084705 (2018).

[246] G. E. Volovik, The universe in a helium droplet, Vol. 117 (Oxford University Press on Demand, 2003).

[247] A. M. Essin and V. Gurarie, Phys. Rev. B **84**, 125132 (2011).

[248] Z. Wang and B. Yan, Journal of Physics: Condensed Matter **25**, 155601 (2013).

[249] R. Peters, T. Yoshida, and N. Kawakami, Phys. Rev. B **98**, 075104 (2018).

[250] A. Barla, J. Derr, J. P. Sanchez, B. Salce, G. Lapertot, B. P. Doyle, R. Rüffer, R. Lengsdorf, M. M. Abd-Elmeguid, and J. Flouquet, Phys. Rev. Lett. **94**, 166401 (2005).

[251] J. Derr, G. Knebel, D. Braithwaite, B. Salce, J. Flouquet, K. Flachbart, S. Gabáni, and N. Shitsevalova, Phys. Rev. B **77**, 193107 (2008).

[252] K. Nishiyama, T. Mito, G. Pristáš, Y. Hara, T. Koyama, K. Ueda, T. Kohara, Y. Akahama, S. Gabáni, M. Reiffers, K. Flachbart, H. Fukazawa, Y. Kohori, N. Takeshita, and N. Shitsevalova, J. Phys. Soc. Jpn **82**, 123707 (2013).

[253] N. P. Butch, J. Paglione, P. Chow, Y. Xiao, C. A. Marianetti, C. H. Booth, and J. R. Jeffries, Phys. Rev. Lett. **116**, 156401 (2016).

[254] Y. Zhou, Q. Wu, P. F. Rosa, R. Yu, J. Guo, W. Yi, S. Zhang, Z. Wang, H. Wang, S. Cai, K. Yang, A. Li, Z. Jiang, S. Zhang, X. Wei, Y. Huang, P. Sun, Y. feng Yang, Z. Fisk, Q. Si, Z. Zhao, and L. Sun, Sci. Bull. **62**, 1439 (2017).

[255] K.-W. Chang and P.-J. Chen, Phys. Rev. B **97**, 195145 (2018).

[256] K. Kimura, T. Yoshida, and N. Kawakami, JPS Conf. Proc. **30**, 011012 (2020).

[257] W. Metzner and D. Vollhardt, Phys. Rev. Lett. **62**, 324 (1989).

[258] E. Müller-Hartmann, Zeitschrift für Physik B Condensed Matter **74**, 507 (1989).

[259] A. Georges and G. Kotliar, Phys. Rev. B **45**, 6479 (1992).

[260] H. Kajueter and G. Kotliar, Phys. Rev. Lett. **77**, 131 (1996).

[261] A. Georges, G. Kotliar, W. Krauth, and M. J. Rozenberg, Rev. Mod. Phys. **68**, 13 (1996).

[262] R. Yamazaki, S. Taie, S. Sugawa, and Y. Takahashi, Phys. Rev. Lett. **105**, 050405 (2010).

[263] L. W. Clark, L.-C. Ha, C.-Y. Xu, and C. Chin, Phys. Rev. Lett. **115**, 155301 (2015).

[264] K. Kimura, T. Yoshida, and N. Kawakami, Phys. Rev. B **100**, 115124 (2019).

[265] R. A. Hart, P. M. Duarte, T.-L. Yang, X. Liu, T. Paiva, E. Khatami, R. T. Scalettar, N. Trivedi, D. A. Huse, and R. G. Hulet, Nature **519**, 211 (2015).

[266] A. Mazurenko, C. S. Chiu, G. Ji, M. F. Parsons, M. Kanász-Nagy, R. Schmidt, F. Grusdt, E. Demler, D. Greif, and M. Greiner, Nature **545**, 462 (2017).

[267] A. Altland and B. D. Simons, Condensed matter field theory (Cambridge university press, 2010).

[268] Y. Gallais and I. Paul, C. R. Phys. **17**, 113 (2016).

[269] H. Yamase, P. Jakubczyk, and W. Metzner, Phys. Rev. B **83**, 125121 (2011).

[270] S.-S. Lee, Annu. Rev. Cond. Matter Phys. **9**, 227 (2018).

[271] M. Zacharias, P. Wölfle, and M. Garst, Phys. Rev. B **80**, 165116 (2009).

[272] H.-Y. Kee, Phys. Rev. B **67**, 073105 (2003).

[273] U. Karahasanovic and J. Schmalian, Phys. Rev. B **93**, 064520 (2016).

[274] A. Abrikosov, L. Gorkov, and I. Y. Dzyaloshinskii, Quantum Theoretical Methods in Statistical Physics (New York: Pergamon Press, 1965).

[275] R. Paulson and J. Schrieffer, Physics Letters A **27**, 289 (1968).

[276] R. A. Cowley, Phys. Rev. B **13**, 4877 (1976).

[277] K. Kimura, M. Sigrist, and N. Kawakami, Phys. Rev. B **105**, 035130 (2022).

[278] H. Yamase and W. Metzner, Phys. Rev. B **75**, 155117 (2007).

[279] H.-Y. Kee, E. H. Kim, and C.-H. Chung, Phys. Rev. B **68**, 245109 (2003).

[280] I. Khavkine, C.-H. Chung, V. Oganesyan, and H.-Y. Kee, Phys. Rev. B **70**, 155110 (2004).

[281] H. Yamase, V. Oganesyan, and W. Metzner, Phys. Rev. B **72**, 035114 (2005).

[282] B. Valenzuela and M. A. H. Vozmediano, New J. Phys. **10**, 113009 (2008).

[283] R. J. Baxter, Journal of Physics C: Solid State Physics **6**, L445 (1973).

[284] F. Y. Wu, Rev. Mod. Phys. **54**, 235 (1982).

[285] Z.-X. Li, Y.-F. Jiang, S.-K. Jian, and H. Yao, Nat. Commun. **8**, 314 (2017).

[286] Z. Bi, E. Lake, and T. Senthil, Phys. Rev. Research **2**, 023031 (2020).

[287] Y. Xu, X.-C. Wu, C.-M. Jian, and C. Xu, Phys. Rev. B **101**, 205426 (2020).

[288] P. A. Lee and T. V. Ramakrishnan, Rev. Mod. Phys. **57**, 287 (1985).

[289] D. Belitz and T. R. Kirkpatrick, Rev. Mod. Phys. **66**, 261 (1994).

[290] D. Belitz, T. R. Kirkpatrick, and T. Vojta, Rev. Mod. Phys. **77**, 579 (2005).

[291] M. Udina, M. Grilli, L. Benfatto, and A. V. Chubukov, Phys. Rev. Lett. **124**, 197602 (2020).

[292] A. Klein, D. L. Maslov, L. P. Pitaevskii, and A. V. Chubukov, Phys. Rev. Research **1**, 033134 (2019).

[293] A. J. Millis, A. J. Schofield, G. G. Lonzarich, and S. A. Grigera, Phys. Rev. Lett. **88**, 217204 (2002).

[294] J. W. F. Venderbos and R. M. Fernandes, Phys. Rev. B **98**, 245103 (2018).

[295] Z. Wang, H. Lim, S. Ng, B. zyilmaz, and M. Kuok, Carbon **46**, 2133 (2008).

[296] X. Cong, Q.-Q. Li, X. Zhang, M.-L. Lin, J.-B. Wu, X.-L. Liu, P. Venezuela, and P.-H. Tan, Carbon **149**, 19 (2019).

[297] H. Suzuura and T. Ando, Phys. Rev. B **65**, 235412 (2002).

[298] A. H. Castro Neto, F. Guinea, N. M. R. Peres, K. S. Novoselov, and A. K. Geim, Rev. Mod. Phys. **81**, 109 (2009).

[299] M. Vozmediano, M. Katsnelson, and F. Guinea, Physics Reports **496**, 109 (2010).

Acknowledgement

I would like to thank Prof. Norio Kawakami for his support during my graduate course and doctoral programs. I have learned a lot of basics as a researcher, from how to give a presentation to how to write a paper. I am deeply grateful to him for many helpful advices and fruitful discussions in carrying out my studies. Especially in my first year as a doctoral student, I felt stuck with my research theme and future direction, but I would like to thank him for always watching over me warmly even when I was not doing well and could not produce any results. As the research progressed through the twists and turns, I was more than happy to hear him say, "Your buds have opened up," or "You've been doing well lately. I could not finish this work without his supervision.

I also thank Prof. Tsuneya Yoshida, Prof. Manfred Sigrist (ETH, Switzerland), and Prof. Robert Peters for collaborations. I have learned a lot through our collaborative researches. I would like to thank Prof. Yoshida for carefully teaching me the basics of topological phases in strongly correlated electron systems and their interesting aspects, since I had just entered the master course. The guidance was strict in some respects, but it gave me the basic skills to become interested in and conduct research in fields such as magnetism, electron correlation, topology, and heavy-fermion systems. One of the most memorable experiences for me was when I practiced my presentation for the first time at a physics conference, and I spent many days practicing my presentation and revising my slides. Thanks to the basics I learned during this time, I have been able to successfully give many oral presentations after that. I would like to thank Prof. Sigrist for the fruitful discussions and collaborations we have had through the WISE program. I have learned the basics of phonons and nematics from him, and I would like to express my deepest gratitude for his kindness to correct my papers repeatedly. I would like to thank Prof. Peters for his fruitful discussions on magnetic topological phases and non-Hermitian researches. I am also deeply grateful to them for many helpful advices in carrying out my studies.

I would like to thank Prof. Yoichi Yanase for his fruitful comments and many helpful advices about electron-nematic states and quantum critical phenomena. I am grateful to him for spending his precious time to discuss this issue when I suddenly visited his laboratory. I also thank Prof. Ryusuke Ikeda, Prof. Masaki Tezuka, and Prof. Akito Daido in Condensed Matter Theory Group for their support as well as fruitful discussions and useful comments. I am also grateful to Dr. Shuntaro Sumita and Dr. Kazuaki Takasan for their help in discussing my research, and useful comments on the topics of twisted bilayer graphene. Particularly, when they give me advices at a research meeting held at UCSB in the fall of my first year of doctoral course, it was a turning point for me. I am deeply grateful to Dr. Sumita for hid frequent discussions and many suggestions. I would like to Dr. Hikaru Watanabe for teaching me about the essence of point groups, Mr. Riki Toshio for fruitful discussions about critical phenomena, and transport properties. I would like to thank Dr. Jun Ishizuka, Dr. Kyosuke Adachi, and Dr. Rina Takashima, who are

former members of room 429, for looking over my abstract, poster, slide, and comment on the application form. I am also grateful to Mr. Shota Kanasugi, Mr. Kaoru Mizuta, Mr. Yoshihiro Michishita for their support as my classmates. Especially the casual well-wishing of everyday life was a great source of emotional support.

I also have greatly benefited from my colleagues, Mr. Riki Toshio, Mr. Kazuki Yamamoto, Mr. Yuhei Ikeda, Mr. Kosuke Nogaki, Mr. Akira Kohuji, Mr. Tatsuya Yamashita, Mr. Ashish Joshi, Mr. Taisei Kitamura, Mr. Dai Nakashima, Mr. Koki Shinada, Mr. Ryotaro Sano, and Mr. Michiya Chyazono, in Condensed Matter Theory Group for everyday discussions on physics, journal club, helpful advices. I would like to express my gratitude again to all the people who have helped me in completing my doctoral thesis.

I would like to acknowledge the financial support from JSPS KAKENHI (Grant No. 20J13688), JSPS Research Fellowship for Young Scientists and WISE Program from MEXT.

Last but not least, I would like to thank my parents, Yoshikazu Kimura and Miyako Kimura, my brothers Tomohiro Kimura and Naohiro Kimura, and my friend Takuma Rendo for their support during my graduate school life. I could not have done it without their support. Without their support, I would not have been able to come this far. Thanks a lot.